SOURCE, SCATTERING AND ATTENUATION EFFECTS ON HIGH FREQUENCY SEISMIC WAVES

by

BERNARD ALFRED CHOUET

Electrical Engineer
Federal Institute of Technology
Lausanne, Switzerland (1968)

S.M., Aeronautics and Astronautics, M.I.T. (1972)
S.M., Earth and Planetary Sciences, M.I.T. (1973)

SUBMITTED IN PARTIAL FULFILLMENT

OF THE REQUIREMENTS FOR THE

DEGREE OF DOCTOR OF PHILOSOPHY

at the

MASSACHUSETTS INSTITUTE OF TECHNOLOGY

September, 1976

Signature of the Author ....
Department of Earth and Planetary Sciences, September 1976

Certified by ....
Thesis Supervisor

Accepted by ....
Chairman, Departmental Committee on Graduate Students

SOURCE, SCATTERING AND ATTENUATION EFFECTS ON HIGH FREQUENCY SEISMIC WAVES

by

BERNARD ALFRED CHOUET

Submitted to
the Department of Earth and Planetary Sciences
on August 12, 1976
in partial fulfillment of the requirements for the
degree of Doctor of Philosophy

ABSTRACT

High frequency coda waves from small local earthquakes are interpreted as backscattering waves from numerous heterogeneities distributed uniformly in the earth's crust. Two extreme models of the wave medium that account for the observations on the coda are proposed. In the first model we use a simple statistical approach and consider the backscattering waves as a superposition of independent singly scattered wavelets. The basic assumption underlying this single backscattering model is that the scattering is a weak process so that the loss of seismic energy as well as the multiple scattering can be neglected. In the second model the seismic energy transfer is considered as a diffusion process. These two approaches lead to similar formulas that allow an accurate separation of the effect of earthquake source from the effects of scattering and attenuation on the coda spectra.

A marked difference was found in the scaling law of earthquake source spectra in various seismic regions of California, Hawaii, and Japan, which may be attributed to the differences in inhomogeneity length and strength of the earth's crust. The apparent Q of coda waves in California and Japan is strongly frequency dependent with values increasing from 60-200 at 1.5 Hz to about 600-2000 at 24 Hz. The increase of the Q of coda with frequency is less pronounced in Hawaii, showing a roughly constant value of 250 below 6 Hz and about 450 near 20 Hz. These observations are interpreted as a combined effect of variation of the intrinsic Q with depth and frequency-dependent composition of coda waves described as follows. The turbidity coefficient of the lithosphere required at 1.5 Hz to explain the observed coda as body wave scattering is orders of magnitude greater than previously known values such as those obtained by Aki (1973) and Capon (1974) under the Montana Lasa from amplitude and phase fluctuations of teleseismic P waves. From the high attenuation and turbidity obtained at this frequency we conclude that at around 1.5 Hz the coda is made of backscattering surface waves from heterogeneities in the shallow, low-Q lithosphere. The high Q observed for the coda at frequencies higher than 10 Hz, on the other hand, eliminates the possibility that these waves are backscattering surface waves. We conclude that at these high frequencies the coda must be made of backscattering body waves from heterogeneities in the deep lithosphere.

The sensitivity of the high frequency coda waves to changes in the medium structure is demonstrated in the data collected at Stone Canyon, California. The temporal change in behavior of the 24 Hz coda observed in this region is interpreted as being related mainly to an increase of the intrinsic Q in the shallow crust.

Thesis Supervisor: Keiiti Aki
Title: Professor of Geophysics

ACKNOWLEDGEMENTS

It was my privilege to have Keiiti Aki as my advisor. His enthusiasm, constant patience and penetrating physical insight made it a rewarding experience to work under his guidance. To him I wish to express my deepest gratitude.

The field experiments were made possible only through the help of many people. Jerry Eaton, Jack Healy, and Dick Thompson of the U.S. Geological Survey helped with the operation at Stone Canyon. Bill Bakun kindly offered his data from Bickmore Canyon and Sam Stewart and Jim Ellis helped with the filtering of this data at the National Center for Earthquake Research in Menlo Park. Bob Tilling, Bob Koyanagi, Elliot Endo, George Kojima, Bill Francis, and the staff of the Hawaiian Volcano Observatory provided support for the experiment at Kilauea. Clarence Allen and Hiroo Kanamori of the California Institute of Technology, Harry Kues and Tom Werntz of the Los Angeles County Flood Control District, and James Vance of the U.S. Geological Survey assisted with the logistics and operation at San Fernando. George Keough of M.I.T. helped with the installation at the Wallace Geophysical Observatory. To all of them, I extend my warmest thanks.

I am grateful to Masaru Tsujiura of Tokyo University for making the data from Tsukuba and Oishiyama available to me, and to Eystein Husebye for the coda record obtained at Norsar.

The digitizing of the records was performed at Lincoln Laboratory. The permission to use the facilities is greatly acknowledged.

I owe special thanks to my friends Michel Bouchon, Raoul Madariaga, Howard Patton and Ken Anderson with whom I had many beneficial discussions at various stages of this work.

For her continuous encouragement and support, her refreshing presence and invaluable help with the preparation of the manuscript, the author wishes to express his sincere gratitude to his wife Danielle.

This research was supported partially by the Energy Research and Development Agency under contract E(11-1)2534 and by the Advanced Research Project Agency, monitored by the Air Force Office of Scientific Research, under contract F44620-75-C-0064.

TABLE OF CONTENT

		page
CHAPTER 1	Introduction	1
CHAPTER 2	Interpretation of coda waves	5
2.1	Origin of the coda of local earthquakes	5
2.2	Two extreme models of coda waves	13
CHAPTER 3	Analysis of data	25
3.1	Earthquake selection	25
3.2	Data preparation	40
3.3	Data processing	42
3.4	Preliminary results	47
CHAPTER 4	Regional variation of the scaling law of earthquake source spectrum	73
4.1	Introduction	73
4.2	Source factors of coda	75
4.3	Construction of the scaling law	89
4.4	Discussion	112
CHAPTER 5	Quantitative discussion on the origin of coda waves	135
5.1	Introduction	135
5.2	Regional turbidities	135
5.3	Regional seismic attenuation properties of earth's crust	146
5.4	Temporal variation in the crustal structure near Stone Canyon	152
5.5	Concluding remarks	167

TABLE OF CONTENT (Continued)

page

CHAPTER 6 Conclusions 169

APPENDIX 171

REFERENCES 174

CHAPTER 1

Introduction

High-frequency seismic waves are a fascinating tool for the study of the fine structure of the earth and the details of seismic sources. To extract the information carried by these waves, however, we must first be able to interpret their seismograms in terms of parameters of their physical models. A straightforward deterministic interpretation is difficult precisely because of the extreme sensitivity of these waves to details. Numerical approaches such as the finite difference and finite element methods may be used in special cases in which the model parameters for the earth medium are known and the computer cost is not a factor. This is, unfortunately, not the case in the usual study of local earthquakes.

The above difficulties may be avoided by resorting to a statistical treatment of the heterogeneity of the earth medium. In other words, a small number of statistical parameters may be sufficient to characterize the medium for the interpretation of a certain aspect of the seismograms. There have been several attempts in recent years along this direction in earthquake seismology (Aki, 1969, 1973; Aki and Chouet, 1975; Takano, 1971; Haddon, 1972, 1975; Cleary and Haddon, 1972; King _et al_., 1973; Capon, 1974; Kopnichev, 1975; Husebye _et al_., 1976; Rautian and Khalturin, 1976) and explosion seismology (Wesley, 1965; Nicolayev, 1968, 1975; Nicolayev and Tregub, 1970; Levin and Robinson, 1969; Dunkin, 1969; Greenfield, 1971), as well as lunar seismology (Nakamura *et al*., 1970; Dainty *et al*., 1974a; Nakamura, 1976).

The longer the waves travel, the greater the variety of heterogeneities they encounter. The later portions of a seismogram therefore may be considered as a result of some kind of averaging over many samples of heterogeneities, thus suggesting a statistical treatment in which a small number of parameters characterize the average properties of the heterogeneous medium.

A few years ago Aki (1969) suggested that the seismic coda waves of local earthquakes are backscattering waves from numerous randomly distributed heterogeneities in the earth and may be treated by a statistical method. More recent studies by Scheimer and Landers (1974) and Aki and Chouet (1975), as well as the observational data accumulated in the past few years by this author and others in this country, Norway, Japan and the USSR seem to support the validity of Aki's model.

The aim of this thesis is to study the high-frequency seismic coda in the range up to 25 Hz observed in the vicinity of small local earthquakes. We shall start, in Chapter 2, by presenting evidence to support the assumption that the coda waves are backscattering waves from randomly distributed heterogeneities. A method will then be described for the interpretation of the observed coda spectra on the basis of two extreme models of the wave medium. In the single backscattering model the scattering is considered to be a weak process, and the loss of seismic energy by scattering is neglected. In the diffusion model the seismic energy transfer is considered as a diffusion process. Both models lead to similar formulas that allow an accurate separation of the effect of earthquake source from the effects of scattering and attenuation on the coda spectra. The method will be applied in Chapter 3 to data from California, Hawaii and Japan, recorded on a spectral analyzing seismograph of Tsujiura (1966, 1967, 1969), and to an earthquake swarm in the Bear Valley, California, recorded by Bakun et al. (1976).

Using the source terms derived according to the above technique, we shall show in Chapter 4 that a markedly different scaling law of earthquake source spectra exists for different seismic areas, which may be attributed to variations in inhomogeneity length and strength of the earth's crust in these regions.

Finally, in Chapter 5, a quantitative analysis of the scattering and attenuation properties of coda waves will be made which leads to a coherent picture of the nature of these waves. We shall conclude that at around 1 Hz they are backscattering surface waves from heterogeneities in the shallow, low-Q part of the earth's crust. On the other hand, at frequencies higher than 10 Hz the coda waves are primarily backscattering body waves from heterogeneities in the deeper, high-Q lithosphere. The temporal variation observed in the high-frequency coda from small earthquakes on the San Andreas fault, central California, is consistent with this model of coda generation and also demonstrates the interest of using these waves for the study of the evolution of tectonic stresses in the earth's crust.

We hope that the work presented here will contribute to a better understanding of the nature of high-frequency seismic waves and of their usefulness in terms of their sensitivity to details of seismic sources and wave paths.

CHAPTER 2

Interpretation of Coda Waves

2.1 Origin of the coda of local earthquakes

Coda waves studied in this thesis are the tail of a seismogram (after the arrival of major wave types such as P, S, and surface waves) recorded at a short distance from an earthquake. Let us first enumerate several important facts about the coda waves.

1. The spectral contents of the early part of a local earthquake seismogram depend strongly on the travel distance and the nature of the wave path to a station. The difference in spectrum among stations, however, diminishes in the later part of the seismogram and disappears in the coda (e.g. Aki, 1956, 1969).

2. For a given local earthquake at epicentral distance shorter than about 100 km the total duration of a seismogram (the length of time from the beginning of P waves to the end of coda) is nearly independent of the epicentral distance or azimuth and can be used effectively as a measure of earthquake magnitude (Bisztricsany, 1958; Soloviev, 1965; Tsumura, 1967; Lee *et al.*, 1972).

3. The power spectra of coda waves from different local earthquakes decay as a function of time (measured from the earthquake origin time) in the same manner independent of the distance and the nature of the path between epicenter and station (Aki, 1969; Aki and Chouet, 1975; this study).

4. The above time dependence (3) is also independent of the earthquake magnitude, at least for small earthquakes with M<6 (Aki, 1969; Aki and Chouet, 1975; this study).

5. The coda excitation depends, however, on the local geology of the station site. It can be 5-8 times larger on the sediment than on granite (Aki, 1969). Interestingly, the amplitude of ambient ground noise tends to be proportional to the site factor of coda excitation, making the total duration recognized on the records for various sites nearly independent of local geology.

6. The study of coda by a small-aperture array of seismographs shows that they are not regular plane waves coming from the epicenter (Aki et al., 1958; Aki and Tsujiura, 1959; Scheimer and Landers, 1974).

Three major origins of coda that immediately come to our minds are (1) slow surface waves due to low-velocity sediment and/or water bodies such as ponds and lakes, (2) waves generated by the aftershocks at the earthquake source, and (3) backscattering by heterogeneities distributed in the large region outside the zone of the direct wave path from the source to the station.

First, the "slow wave" model cannot explain the items 1, 2, 3, and 4 in the list of observed facts described above. The clearest evidence against this model can be seen in Figure 1 of Aki (1969), in which the equality of coda spectra is demonstrated between stations located within 1-2 km from the epicenters and those at 15-18 km away. The short-period records of a local earthquake at Norsar (Figure 2.1) further demonstrate the independence of coda power decay on the nature of wave path between the earthquake source and various subarray locations, as well as on the epicentral distance which ranges from a few kilometers to more than 100 km in this case.

The "aftershock" model may be refuted on the following two accounts. The item 2 on the list of observed facts, that the total duration serves as the measure of earthquake magnitude, can be explained if the aftershocks last longer for greater earthquakes. If so, however, it seems rather fortuitous that the time function for the decay of amplitude is independent of earthquake magnitude (item 4). Secondly, as shown in Figures 3.10, 3.11 and 3.12 of this thesis, the amplitude decay curve is very regular and repeatable for different earthquakes. We expect a more erratic, variable decay curve if it represents the intensity of aftershocks.

The "backscattering" model, on the other hand, satisfactorily explains all the observed facts enumerated before. Strong evidence supporting this model can be found in Figure 2.2 reproduced from Scheimer and Landers (1974). This figure shows the energy in the frequency band 1.0-2.0 Hz of a short-period record at the F2 subarray of Lasa for a strip-mining blast 113 km away as a function of time. The peak energy in this band is due to the arrival of the S wave. The

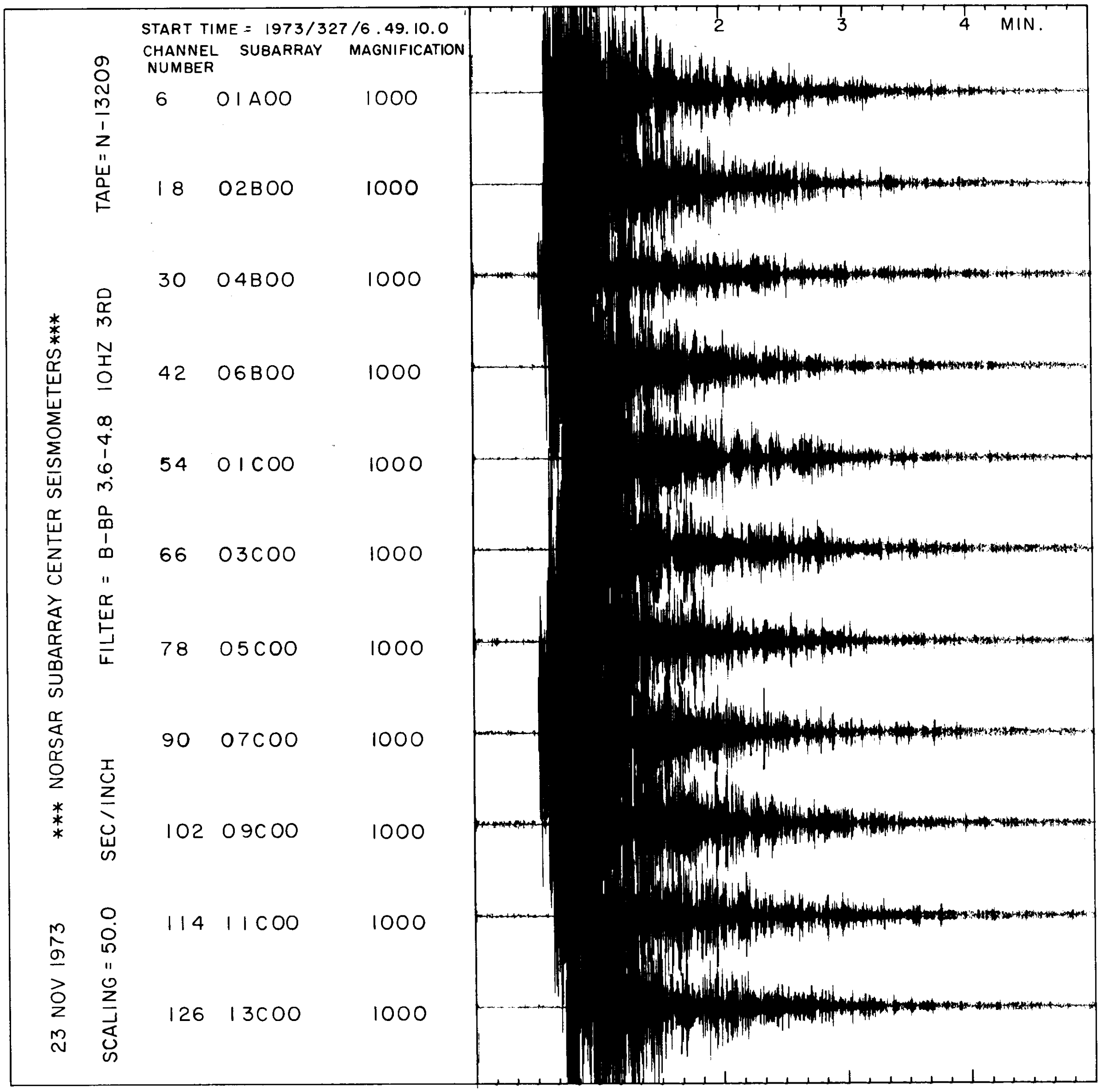

Fig. 2.1. Short-period (band-pass from 3.6 to 4.8 Hz) records of a local earthquake at NORSAR near subarray 7C. The epicentral distance is a few kilometers to the closest subarray and more than 100 km to the farthest. The decay of coda power shows no dependence on the details of the different wave paths between the earthquake source and each subarray.

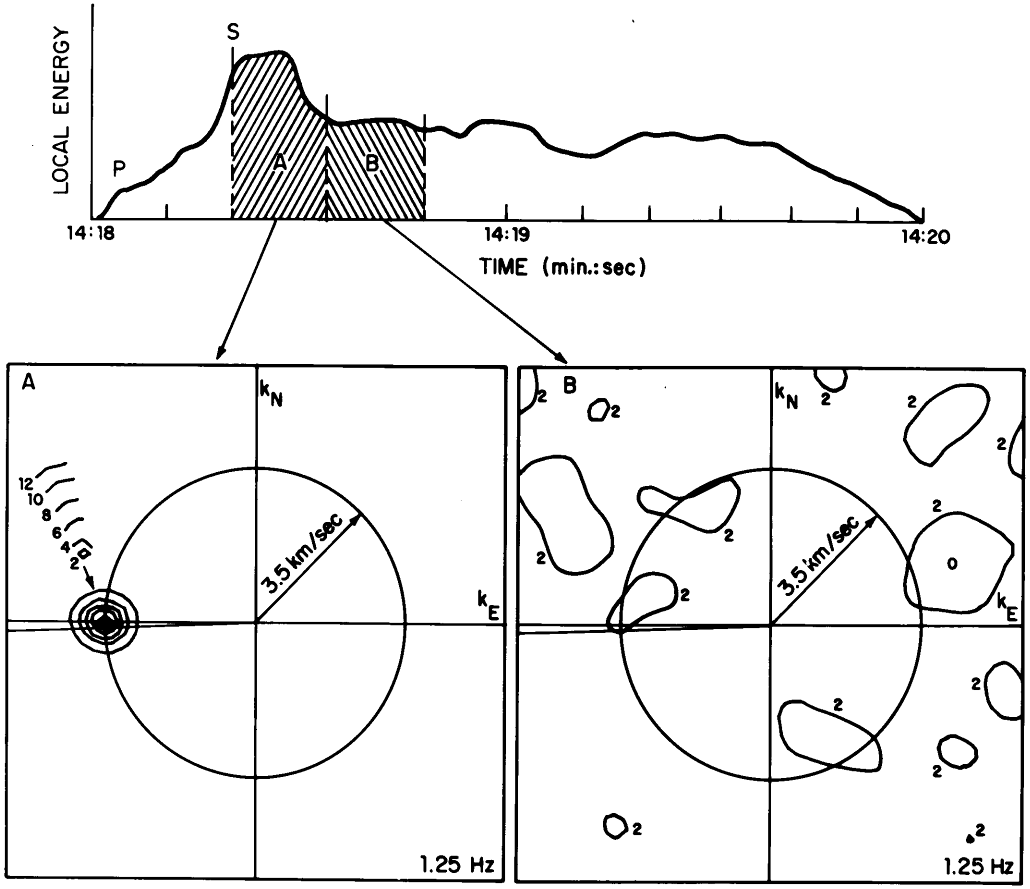

Fig. 2.2. High-resolution spectra for S arrival and S coda in the frequency band 1.0-2.0 Hz for a strip-mining blast near Lasa. This figure is reproduced from Scheimer and Landers (1974).

high-resolution wave number spectrum (Capon, 1969) for this section of the record indicates that virtually all the energy is arriving from the direction of the blast. The wave number spectrum for the later S coda indicates that energy is arriving from all directions with shear and surface wave velocities.

Let us then follow the waves as they are generated from an earthquake. The duration of the major event at an earthquake source may be measured roughly by the fault length divided by the rupture velocity. Since the fault length for earthquakes with magnitude (M) 6 is about 10 km and the rupture velocity is roughly the shear velocity, we expect that the source duration of earthquakes with $M<6$ is less than a few seconds. The duration for an M1 earthquake is probably a few hundredths of a second.

We shall call the waves which spread outward from the source "primary waves". The nature of primary waves observed at a station will depend on the earth's structure along the wave path from source to station. At high frequencies the appearance of primary waves will be quite different for different wave paths.

As the primary waves spread out, secondary waves are generated at each of the heterogeneities that they encounter. Suppose, for simplicity, that both the primary and the secondary waves are of the same kind of wave with velocity v. Suppose also, that the energy contained in the scattered waves is weak compared to the incident wave energy so that essentially singly scattered waves are observed. Then we consider a time interval $(t, t + \Delta t)$ measured from the origin time where Δt is longer than the duration of primary waves. During this time interval the secondary waves arrive from heterogeneities within the zone sandwiched by two ellipses (for surface waves; ellipsoids for body waves), both with the foci at source and station and with the length of the major axis equal to vt and $v(t + \Delta t)$.

Consider seismograms of an event recorded at two different stations. For the given time interval $(t, t + \Delta t)$ the two elliptical (or ellipsoidal) zones will increasingly overlap as t increases. Besides, a greater number of heterogeneities will contribute to the later time interval and tend to average out the difference between backscattering energies received at the two stations. Thus the difference in the appearance of seismograms disappears in the coda.

The field of the backscattered waves will appear locally stationary in space and time, implying an equal energy flow in opposite directions across a geologic boundary. Thus the particle velocity in a low-impedance medium will be greater than that in a high-impedance medium when the two are in contact. Since the ambient noise is also stationary, we expect the same amplification effect for a low-impedance medium. Since the ratio of coda amplitude to the ambient noise determines the tail end of a seismogram, the total duration will not depend on the local geology of the station site.

We shall now summarize the properties of coda waves discussed in this section in the following simple equation for the power spectrum of coda waves at time t measured from the earthquake origin time:

$$P(\omega|t) = S(\omega)C(\omega|t) \tag{2.1}$$

Here $C(\omega|t)$ is independent of the earthquake source parameters. It represents the effect of a large volume and is independent of the distance or the nature of the direct wave path from the source to the station. For a fixed ω, $C(\omega|t)$ depends only on the time t. On the other hand, $S(\omega)$ expresses the effect of earthquake source. Let $P_1(\omega|t)$ and $P_2(\omega|t)$ be the coda power for two different earthquakes. Since $C(\omega|t)$ is common to both and is independent of locations of station or epicenter, we can write

$$\frac{P_1(\omega|t)}{P_2(\omega|t)} = \frac{S_1(\omega)}{S_2(\omega)} \tag{2.2}$$

Thus the coda power will give us the ratio of source factor $S(\omega)$ for different earthquakes without knowing what $C(\omega|t)$ is. The ratio $S_1(\omega)/S_2(\omega)$ physically means the ratio of total seismic energy generated by an earthquake in the unit frequency band around ω.

Strictly speaking, the assumption that $C(\omega|t)$ is common to all sources implies that different seismic sources share a common composition of wave types, so that the same backscattering effect applies to all. Another implicit assumption is that the duration of primary waves is short in comparison with the time interval t over which the coda power $P(\omega|t)$ is estimated. It is also implicit that the spatial dimension of primary source (earthquake) is small in comparison with $v\Delta t$, where v is the velocity of wave propagation. Some of these assumptions may seem to be oversimplifications, but they give results roughly agreeing with observations.

2.2 Two extreme models of coda waves

For a more quantitative exposition of the origin of coda waves we shall consider two specific models. One is the single-scattering model, in which we consider the coda as a superposition of backscattering wavelets from discrete scattering sources. Each wavelet is due to a single scatterer in the absence of the other scatterers. In this model, the scattering is a weak process, and use is made of the Born approximation in that the loss of energy from the primary waves as well as the multiple scattering is neglected. Because of these over-simplifications the law of energy conservation is violated.

In the second model we shall go to the other extreme and consider the seismic energy transfer as a diffusion process. In this case the energy, of course, is conserved. However, the interpretation of the diffusion coefficient in terms of the heterogeneous wave medium is not straightforward.

Let us first consider the single-scattering model and, for simplicity, put the seismic station at the same place as the earthquake source. This assumption is valid for the sufficiently later part of the coda for then the distance from the earthquake source to any scatterer as well as the distance from the scatterer to the station largely exceed the hypocentral distance, so that a single radius r is a good approximation for the wave paths of both the direct and backscattered waves. Let then $\phi(\omega|r)$ be the Fourier transform of displacement due to a backscattering wavelet from a single scatterer located at a distance r; $\phi(\omega|r)$ depends on the earthquake source as well as on the scatterer. Assume that the scatterers responsible for coda waves are distributed randomly but uniformly in space, and let $N(r)$ be the number of scattering sources within radius r of the station. Then the number of scatterers in the zone bounded by $(r, r + \Delta r)$ will be $(dN/dr)\Delta r$. On the assumption that both primary waves and scattered waves are of the same kind and share the same propagation velocity, the backscattering waves from scatterers in $(r, r + \Delta r)$ will arrive at the station in the time interval $(t, t + \Delta t)$, where $t = 2r/v$ and $\Delta t = 2\Delta r/v$. For a distance range Δr long enough, so that the corresponding Δt is greater than the duration of an individual backscattering wavelet, and for a random distribution of scatterers, the sum of the energy carried by backscattered waves arriving in $(t, t + \Delta t)$ will be equal to Δt times the power spectral density $P(\omega|t)$ of the coda waves. Thus we write

$$P(\omega|t)\Delta t = \sum_{r<r_n<r+\Delta r} |\phi_n(\omega)|^2 = \frac{dN}{dr} \Delta r |\phi(\omega|r)|^2 \qquad (2.3)$$

where r_n is the distance from the station to the nth scatterer. Let us now consider the scattering of body waves. We assume a density σ of scatterers per unit volume. The number of scatterers within the spherical shell $(r, r + \Delta r)$ is $(dN/dr)\Delta r = 4\sigma\pi r^2 \Delta r$. From (2.3) we then write

$$P(\omega|t)\Delta t = |\phi(\omega|r)|^2 4\sigma\pi r^2 \Delta r \qquad (2.4)$$

The geometrical spreading being taken into account, the amplitude spectra of the scattered waves will depend on travel distance according to

$$|\phi(\omega|r)| = \phi_o(\omega) f(\omega) \frac{1}{r^2} \qquad (2.5)$$

where $\phi_o(\omega)$ represents the earthquake source, $f(\omega)$ the frequency dependent scattering, and r represents the distance between the earthquake source and scatterer, as well as the distance between station and scatterer.

Then at a reference distance $r = r_o$,

$$|\phi(\omega|r_o)| = \phi_o(\omega)f(\omega)\frac{1}{r_o^2} \tag{2.6}$$

Combining equations (2.5) and (2.6), we obtain

$$|\phi(\omega|r)| = |\phi(\omega|r_o)| \ (\frac{r_o}{r})^2 \tag{2.7}$$

In addition to the above geometrical spreading the waves should attenuate due to the anelasticity of the earth medium which turns the seismic energy into heat. By using the quality factor Q the fractional loss of energy per 1 cycle is $2\pi Q^{-1}$, and the attenuation in power during the time period t is exp $\{-\omega t/Q\}$, where ω is the angular frequency. We then write the secondary wave intensity

$$|\phi(\omega|r)| = |\phi(\omega|r_o)|(\frac{r_o}{r})^2 e^{-\omega t/2Q} \tag{2.8}$$

From (2.4) and (2.8) and since $r = vt/2$, $\Delta r = v\Delta t/2$, we obtain the expression for the power spectral density of coda waves as backscattering body waves:

$$P(\omega|t) = |\phi(\omega|r_o)|^2 8r_o^4 \ \pi\sigma v^{-1} t^{-2} e^{-\omega t/Q} \tag{2.9}$$

On the other hand, if the coda is made of backscattering surface waves, we obtain another formula,

$$P(\omega|t) = |\phi(\omega|r_o)|^2 2r_o^2 \pi\sigma t^{-1} e^{-\omega t/Q} \qquad (2.10)$$

where σ is now the density of scatterers per unit area. Both (2.9) and (2.10) can be written in a more general form as

$$P(\omega|t) = S(\omega)t^{-m}e^{-\omega t/Q} \qquad (2.11)$$

the constant m being determined by the geometrical spreading, with $m = 1$ for surface waves and $m = 2$ for body waves. The source term $S(\omega)$ in (2.11), which varies with earthquake magnitude, represents the effect of both the primary and the secondary wave sources. Since the secondary wave source, namely the scattering by heterogeneity, is common to all earthquakes (as long as the composition of primary waves is the same), the difference in this source factor should be due to the difference in the earthquake source.

Within the scheme of this single-scattering model, however, we have a serious conceptual difficulty concerning the physical meaning of Q introduced above. Because the Born approximation neglects the gradual decay of the incident field due to the scattering process and furthermore neglects multiple scattering we cannot separate anelastic loss from loss through scattering. At first it may look as if the inclusion of loss by scattering is an improvement over the simple single-scattering model. Then one realizes that the multiple scattering may pump energy back to the primary waves as well as to the backscattering waves. The basic difficulty stems from the inadequacy of the Born approximation in dealing with the energy balance. It violates the law of conservation of energy (Howe 1971, 1973a,b).

To avoid the above difficulty, we shall now consider the other extreme model in which all the seismic energy is scattered through diffusion. Such a model has been applied previously to the earth by Wesley (1965) and to the moon by Nakamura et al. (1970). Let $E(\vec{x}, t, \omega)$ be the seismic energy per unit volume within a unit frequency band around ω. Then the conservation of energy leads to a modified diffusion equation including linear dissipation

$$\frac{\partial E}{\partial t} = D\nabla^2 E - \frac{\omega}{Q}E \qquad (2.12)$$

where D is the diffusivity and the last term represents the loss by anelasticity which turns the seismic energy into heat. Clearly, here Q is the intrinsic quality factor and does not include the loss by scattering. The solution of (2.12) for a point source in time and space is given by

$$E(\vec{x},t,\omega) = \frac{W(\omega)}{(4\pi Dt)^{3/2}}\exp\left(-\frac{x^2+y^2+z^2}{4Dt}\right)\exp\left(-\frac{\omega t}{Q}\right) \qquad (2.13)$$

for the three-dimensional diffusion corresponding to body wave scattering. Here $W(\omega)$ is the total seismic energy generated by the earthquake source within the unit frequency band around ω.

For large t and small hypocentral distance $(x^2+y^2+z^2)^{1/2}$ at which the coda waves are observed, (2.13) becomes a function of only time t and is independent of distance; this is an observed result for coda power. Since we defined coda power $P(\omega|t)$ for ground displacement and the seismic energy per unit volume is twice the kinetic energy for propagating waves or stationary vibrations, we have

$$\rho\omega^2 P(\omega|t) = E(o,t,\omega) \qquad (2.14)$$

Putting (2.13) into (2.14), we get

$$P(\omega|t) = \frac{W(\omega)}{\rho\omega^2(4\pi Dt)^{3/2}} \exp\left(-\frac{\omega t}{Q}\right) \qquad (2.15)$$

Thus the diffusion theory gives an equation similar to (2.11) with a power of t(-3/2) intermediate to body wave (-2) and surface wave (-1) single-scattering models.

Coming back to (2.3) we now rewrite the equation for coda power as

$$P(\omega|t) = \frac{v}{2}\frac{dN}{dr}\,|\phi(\omega|r)|^2 \qquad (2.16)$$

In order to relate this equation with the usual scattering formula we shall formulate the scattering problem following Chernov (1960). Consider a heterogeneous region of volume V buried in an unbounded homogeneous medium. Acoustic plane waves $A_o e^{i\omega[t-(x/c)]}$ propagating in the x direction are incident on the heterogeneous region. Observations of the scattered waves are made in the far field (Fraunhofer zone) in the homogeneous medium, at which the scatterer volume V may be considered as a point source, so that the scattered waves may be approximated as $A_1 e^{i\omega[t-(R/c)]}$, where R is the distance between the center of V and the station. For wavelength λ and linear dimension L of the scatterer volume V, the distance R must be greater than $2L^2/\lambda$ to be in the Fraunhofer zone. Then the scattered power $|A_1|^2$ is proportional to the incident power $|A_o|^2$, the volume V of the heterogeneous region, and the reciprocal R^{-2} of squared distance. Putting the proportionality factor $g(\theta)/4\pi$, where θ is the angle between the direction from the center of scattering volume to the station and the direction of propagation of incident waves (x axis), we have

$$|A_1|^2 = |A_o|^2 \frac{Vg(\theta)}{4\pi R^2} \tag{2.17}$$

The average of $g(\theta)$ over all directions is equal to the fractional loss of energy by scattering and is called the "turbidity coefficient". The value $g(\theta)/4\pi$ is equal to the fractional loss of energy by scattering per unit solid angle around the direction θ.

Considering now our problem of coda waves, we shall put the Fourier transform of primary waves at the distance r to be $\phi_o(\omega|r)$. For large r the incident waves may be considered to be plane waves locally. Consider, then the incident plane waves $A_o = \phi_o(\omega|r)$ upon the heterogeneous region of volume $V = 4\pi r^2\Delta r$. If there is only one scatterer in the volume V, $A_1 = \phi(\omega|r)$. Since there are $(dN/dr)\Delta r$ scatterers in V and they add randomly, we have the relation $|A_1|^2 = (dN/dr)\Delta r|\phi(\omega|r)|^2$. Putting these relations into (2.17) we have

$$\frac{dN}{dr}|\phi(\omega|r)|^2 = g(\pi)|\phi_o(\omega|r)|^2 \qquad (2.18)$$

where we put $\theta = \pi$, assuming a literal backscattering. The value $g(\pi)$ is 4π times the fractional loss of energy by scattering in the backward direction per unit solid angle. We shall call $g(\pi)$ the "backward turbidity coefficient". Putting (2.18) into (2.16) we have a remarkably simple formula for coda power spectrum:

$$P(\omega|t) = \frac{v}{2}\, g(\pi)|\phi_o(\omega|r)|^2 \qquad (2.19)$$

The above equation relates the observed coda power with the spectrum of primary waves. If both are known, we can find the backward turbidity coefficient which will give some constraint on the nature of heterogeneity.

For an acoustic random medium characterized by the mean square fluctuation $<\mu^2>$ of the refractive index and spatial auto-correlation function $N(r) = e^{-r/a}$, Chernov (1960) gives the following formula for $g(\theta)$:

$$g(\theta) = \frac{8k^4a^3<\mu^2>}{(1+4k^2a^2\sin^2\frac{\theta}{2})^2} \qquad (2.20)$$

where k is the wave number $2\pi/\lambda$. Chernov also gives the following result for $N(r) = e^{-r^2/a^2}$.

$$g(\theta) = (\pi)^{1/2}k^4a^3<\mu^2>\exp(-k^2a^2\sin^2\frac{\theta}{2}) \qquad (2.21)$$

It is interesting to note that the above two different N(r) give similar results for forward scattering ($\theta \simeq 0$) for any ka but give drastically different results for backscattering ($\theta \simeq \pi$) for large ka. For example, Aki (1973) fitted the Chernov model to the scattering of P waves with frequency 0.5 Hz under the Montana Lasa, with parameters $ka = 5$, $<\mu^2> = 0.0016$, and $a = 10$ km, which give the backward turbidity coefficients 8×10^{-5} per kilometer for $N(r) = e^{-r/a}$ and 2.5×10^{-12} per kilometer for $N(r) = e^{-r^2/a^2}$. At frequencies higher than 0.5 Hz the backward turbidity coefficients stay nearly the same for $N(r) = e^{-r/a}$ but become smaller for $N(r) = e^{-r^2/a^2}$.

Similarly, in our diffusion model the diffusivity D may be related to the wave-scattering process. In analogy with the scattering of particles moving with a certain mean free path, Dainty et al. (1974b) obtained the relation between D and the mean free path ℓ as

$$D = \frac{v\ell}{3} \tag{2.22}$$

where v is the velocity of wave propagation and ℓ is defined as the distance travelled by the primary wave, over which its energy is reduced to e^{-1} by scattering. By definition, ℓ is the reciprocal of the turbidity coefficient. Since the scattered energy in the forward direction behaves more like waves rather than a diffusion process, the diffusion theory may apply only to the part of energy scattered in the backward direction. Then the turbidity coefficient which enters in (2.22) through ℓ should probably be the backward turbidity $g(\pi)$ rather than the average of $g(\theta)$ over all directions. Thus we get two rough estimates of backward turbidity, one by the single-scattering theory and the other by the diffusion theory.

At this point one may question the relevance of the solution (2.15) of the diffusion equation for a point source to our problem, if the diffusion theory applies to the part of the energy scattered in the backward direction. It may be more appropriate to assume a scattering source moving with the primary waves.

In Chapter 5 we shall make a rough estimate of diffusivity by using (2.15). We shall find that the diffusivity is rather high, $10^{11} \sim 10^{12}$ cm^2/sec. For the range of time 10-150 sec, at which most coda measurements were made, the above diffusivity gives a mean diffusion distance greater than or comparable to the travel distance of primary waves.

It appears, then, that as the primary waves spread out, they will leave behind a pool of scattered energy which becomes quickly homogeneous inside the pool because of high diffusivity. Then the coda amplitude decay observed in the pool will depend on the rate of energy pumped into the pool, the rate of increase in volume of the pool, and the rate of intrinsic loss of energy (conversion to heat). The rate of energy pumped into the pool depends on the amplitude history of primary waves, which not only lose energy by scattering but also gain energy back from the pool by diffusion. This is a complex process and cannot be rigorously treated by our rudimentary theory. The approach from the kinetic theory for wave propagation in random medium, such as that discussed by Howe (1973b), may be promising but is beyond the scope of this thesis. It is our feeling, however, that the validity of (2.11) may survive a more rigorous treatment.

CHAPTER 3

Analysis of Data

3.1 Earthquake selection

Six areas in western Japan, the island of Hawaii, central and southern California, and eastern Massachusetts, were selected for our study of the coda of local earthquakes. With the exception of one data set from central California provided by Bakun *et al*. (1976), the data reported here were recorded on a spectral analyzing seismograph designed and constructed by M. Tsujiura of Tokyo University. The seismograph consists of a short period ($T_o = 1$ sec) vertical transducer, an amplifier, a low-pass filter with the corner frequency of 1 Hz, and five octave band-pass channel filters with center frequencies at 1.5, 3, 6, 12 and 24 Hz and respective bandwidths of 1, 2, 4, 8 and 16 Hz. The frequency response of the seismometer-amplifier-recorder system at maximum magnification and the filter characteristics are shown in Figure 3.1. The output of the six filters is recorded continously at the rate of 1 mm/sec on an ink-writing six-channel recorder. Examples of records of coda amplitudes obtained in Japan are shown in Fig. 3.2 for two earthquakes, A($M = 3.5$) and B($M = 4.8$) near Tsukuba. Similar records were obtained in other areas as depicted for example in Figure 3.3 for three earthquakes with magnitudes M_L of 1.0, 2.1 and 2.9 in the Bear Valley region of central California.

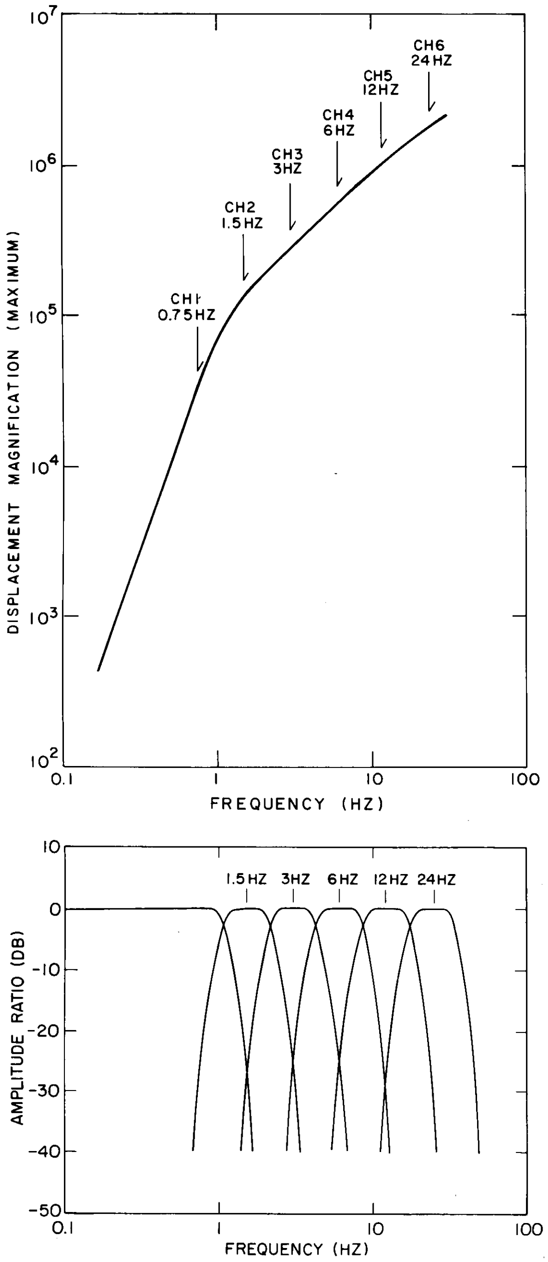

Fig. 3.1. Amplitude frequency response of the seismometer-amplifier-recorder system (top) and of the low-pass and band-pass filters (bottom) used in the spectral analysis. The vertical seismometer has a natural period of 1 sec and a damping factor of 0.8.

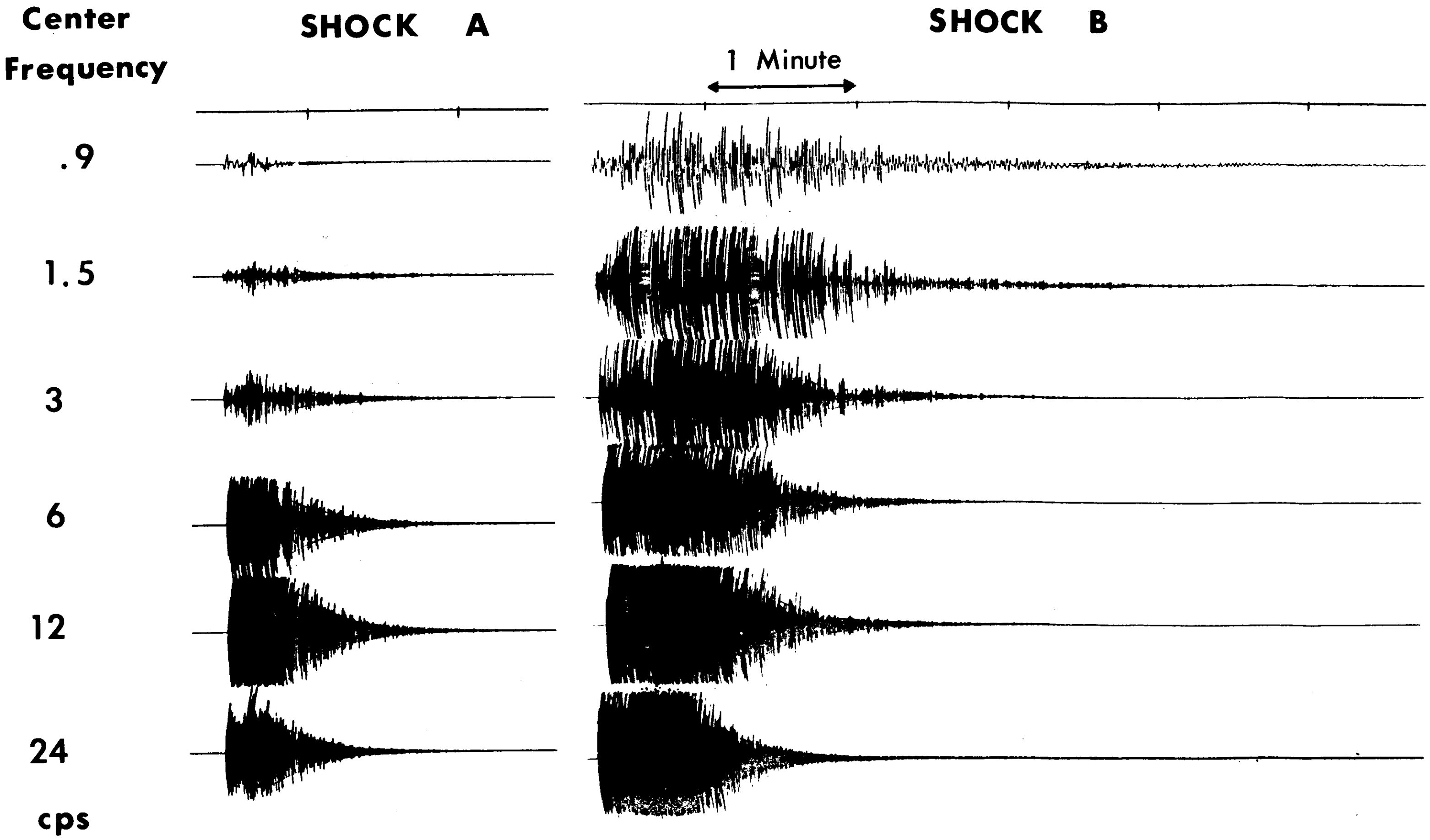

Fig. 3.2. Traces of two events, A(M = 3.5) and B(M = 4.8) recorded at Tsukuba, Japan, with the spectral analyzing seismograph. Channel center frequencies are indicated at left. Tick marks on top are minute marks.

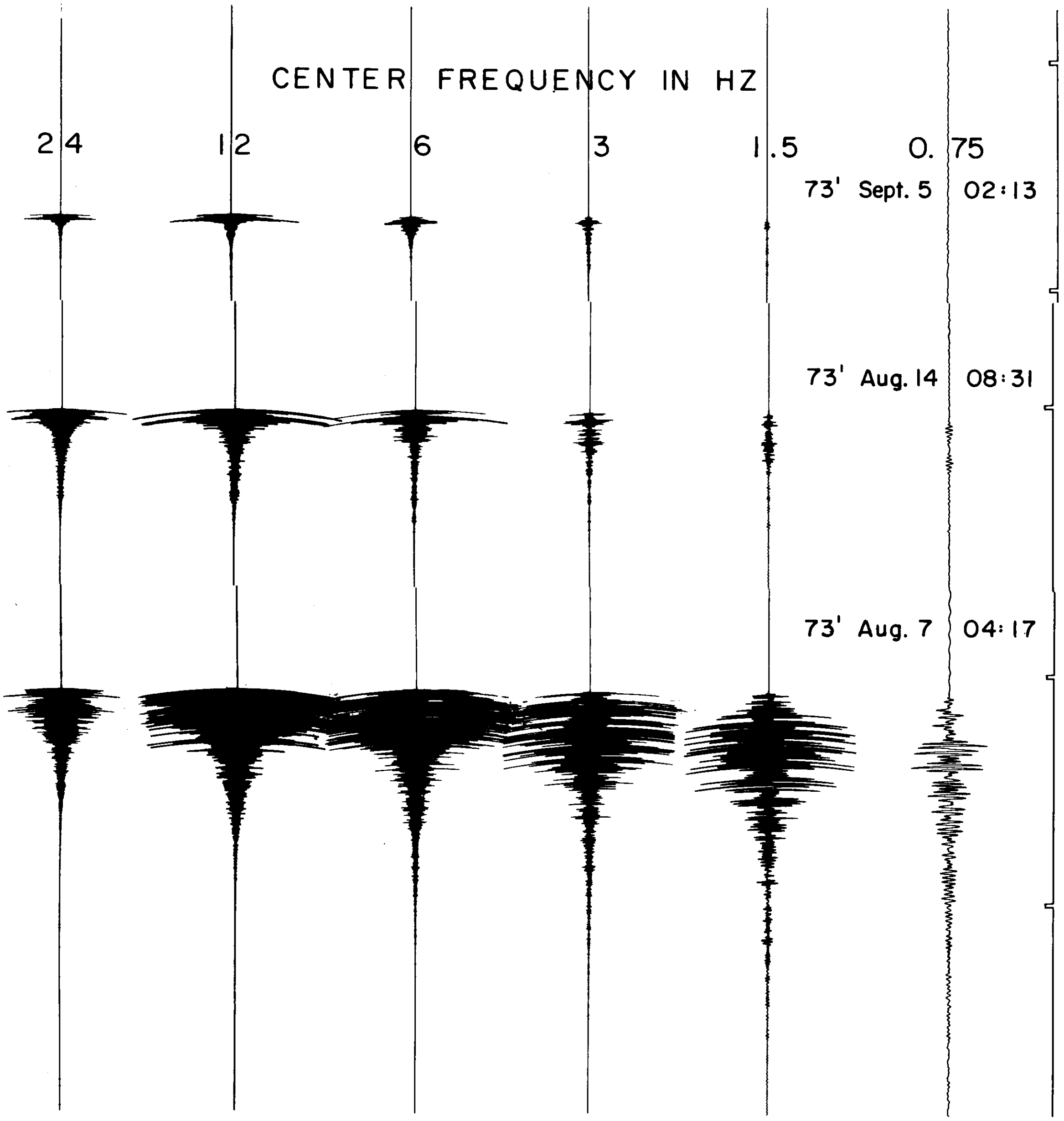

Fig. 3.3. Traces of three events with magnitudes 1 (top), 2.1 (middle), and 2.9 (bottom) recorded at Stone Canyon, California, with the spectral analyzing seismograph. Channel center frequencies are indicated at the top of the figure. Tick marks on right side of figure are minute marks.

In central California, the data we selected were recorded at a temporary seismograph station STC (36°38'12"N, 121°15'18"W) situated in Stone Canyon, 1 km west of the U.S. Geological Survey Stone Canyon observatory on the San Andreas fault trace. The location of station STC and the spatial distribution of earthquake epicenters are shown in Figure 3.4 in relation to the major faults in the area. The U.S.G.S. epicenter locations in this region are systematically biased toward the west because the lateral variation of seismic velocities between the east and west side of the San Andreas fault (Boore and Hill, 1973) was not taken into account in the determination of the earthquake foci. It is probable that the epicenters shown in Fig. 3.4 should be migrated onto the San Andreas - Bear Valley fault system. These earthquakes thus essentially represent the activity along this fault complex. The deepest event recorded at STC has a focal depth of 13.5 km and the median depth of focus for the ensemble of events is 5.6 km. The accuracy of depth determination for these earthquakes is on the average better than 1 km. All the epicenters are within 20 km of the station. Recording at STC extended over a period of eleven months, starting July 17, 1973 and ending June 24, 1974. The spectral analyzing system was initially operated with maximum amplification as indicated in Fig. 3.1. The amplifier gain was then divided by 2 at 17.00 UT on July 18, and on August 6 the magnification level was finally lowered to 4/10 of the

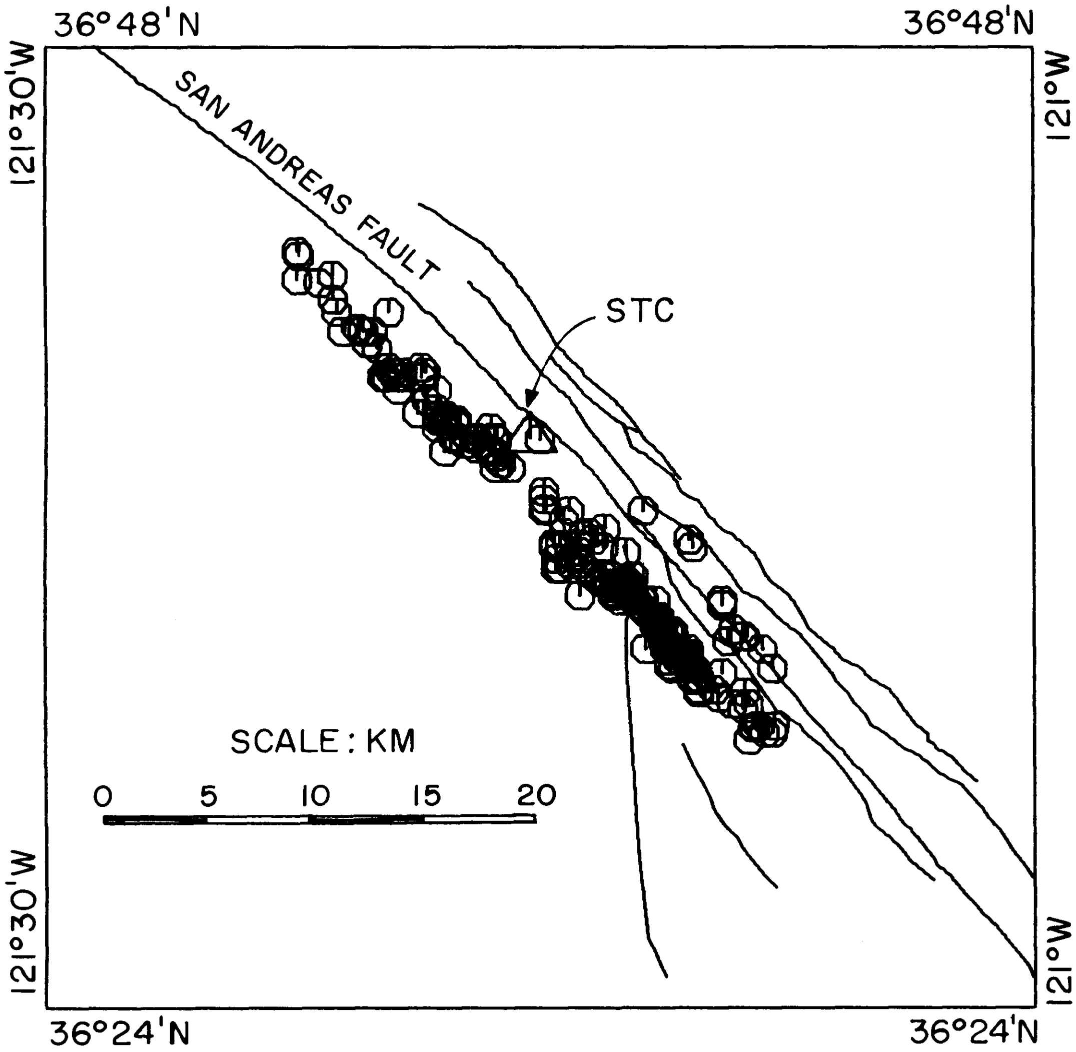

Fig. 3.4. Epicenters of the earthquakes used in the coda analysis at Stone Canyon (STC) in central California. All the earthquakes in this area are shallower than 14 km and are mostly confined within 20 km of the station. Note that since the U.S.G.S. epicentral locations did not take into account the seismic velocity anomaly across the San Andreas fault, each event in the figure appears slightly shifted to the west.

maximum gain where it remained until the end of the operation at STC. One hundred and eighty five earthquakes ranging in magnitude from 0.9 to 3.3 were selected for our study. The pertinent parameters for each event are summarized in Table 1.

In addition to the data from Stone Canyon, 26 events from the January 15, 1973, earthquake sequence on the San Andreas fault near Bear Valley, collected by W.H. Bakun, were made available to us. These earthquakes were recorded with short-period (T_o = 1 sec) Willmore seismometers at the three component temporary station BIC (36°33'38.4"N, 121°12'21"W) situated in Bickmore Canyon, 4 km west of the San Andreas fault trace and 10 km southeast of STC. The output of the seismometers was amplified and recorded on FM tape (dual gain levels for each seimic channel, 30db separation), together with binary (IRIG C) time code. The amplifiers were initially set at a gain of 200 for the high gain channels so that signals from moderate-size local earthquakes would remain on scale. Usable records were obtained for the $M_L = 4.1$, January 15, 1973 earthquake and several large ($M_L \geq 2.5$) aftershocks. On February 1, 1973, the amplifier gains were increased to 3125 to obtain records of smaller ($M_L \leq 2.5$) aftershocks. The playback signals from the analog FM tapes, bandwidth limited to 16 Hz, were digitized at the scale of 530 counts/4 volts.

The digital tapes of the vertical component of motion, which were available for our study, were reconverted to analog format with a scale of 5 volts to 2048 counts before being band-pass filtered at the U.S.G.S. National Center for Earthquake Research in Menlo Park, California. For our purpose we chose a low-pass filter with a corner frequency of 1 Hz and 4 band-pass filters with center frequencies at 1.5, 3, 6 and 13.5 Hz, and bandwidths of 1, 2, 4, and 11 Hz, the upper frequency limit being fixed by the 18 db/octave roll-off of the tape playback unit beyond 16 Hz. The roll-off rates of the filters selected were 25 db/octave. Recording was done on an ink-squirting 16-channel chart recorder at 1 mm/sec with a sensitivity of 10.83 mm/v. To calibrate the signal, the amplitude frequency response of the seismometer (mass velocity versus ground displacement) was expressed as $\omega^3/[(\omega_o^2 - \omega^2)^2 + (2\xi\omega_o\omega)^2]^{1/2}$, with $\omega = 2\pi f$, $f_o = 1$ Hz, and $\xi = 0.7$. The seismometer sensitivity was 3.36 v/cm/sec. The overall transfer function of the system relating chart record amplitudes (in mm) to actual ground motion (in micron) was thus expressed as $Kf^3/(1 + f^4)^{1/2}$ mm/μ, with K = 1.5 prior to February 1, and K = 23.1 after that date.

Of the 26 earthquakes in the aftershock sequence, 18 were retained for our analysis of the coda. The locations of their epicenters and of station BIC are shown in Fig. 3.5. The epicentral distances of these earthquakes range from 12 to 18 km and focal depths vary from 0.1 to 7.4 km. For the reason mentioned earlier, the events shown in Fig. 3.5 should probably be slightly shifted toward the east onto the San Andreas fault. The magnitudes of the 18 shocks range from $M_L = 1.8$ to $M_L = 4.1$. Relevant parameters for each event are summarized

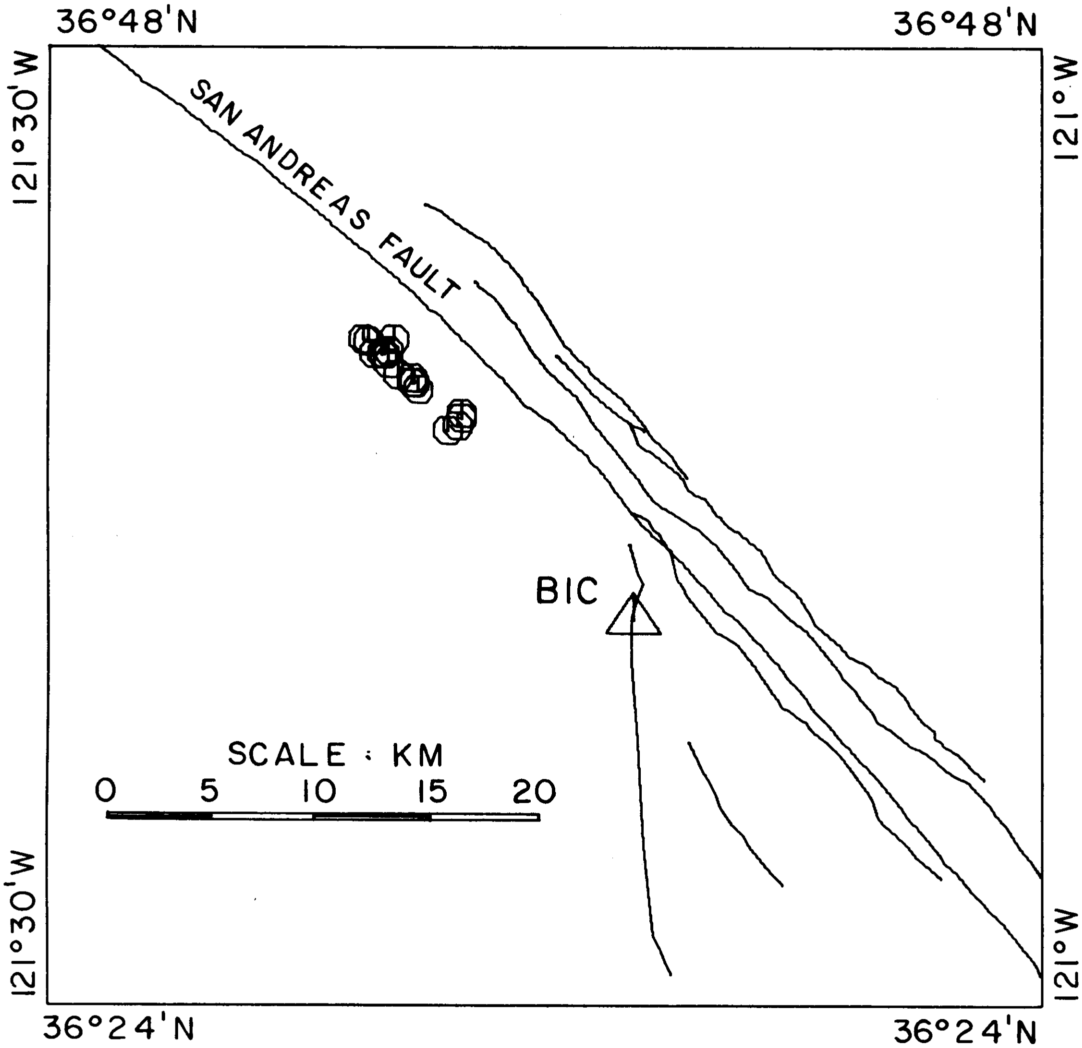

Fig. 3.5. Epicenters of the earthquakes used in the coda analysis at Bickmore Canyon (BIC) in central California. The events are shallower than 8 km and are all within 20 km of the station (see also note in Figure 3.4).

in Table 2. Because of the similarity in the source regions of the earthquakes recorded at the Bickmore Canyon Station and of those recorded at Stone Canyon, these two data sets are considered to be compatible.

In southern California, the station PAC (34°19'46.7"N, 118°23'51"W) was operated for 2 months in the Pacoima Canyon, near San Fernando. The period of recording at this location extended from July 16, to September 2, 1974. The set up of the spectral analyzing system remained the same as when installed at Stone Canyon, with the magnification level first set at 8/10 of the maximum amplification (see Figure 3.1), then switched to 4/10 of the maximum gain on July 23. The parameters of the 27 earthquakes retained for our study are listed in Table 3. The location of their epicenters, shown plotted in Fig. 3.6 in relation to station PAC and various fault traces in the region was achieved using additional data from the C.I.T. seismic network in the Los Angeles area. All the earthquakes selected are shallower than 13 km and are mostly confined within 20 km of the station. Their magnitudes range roughly from $M_L = 1.0$ to $M_L = 3.0$.

During the summer of 1975 the spectral analyzing seismograph was installed at station OTL (19°23'22.8"N, 155°16'56.4"W) on the edge of the Kilauea volcano caldera, on the island of Hawaii. To improve the signal to noise ratio at this site, a buffer amplifier with a gain of 20 and bandwidth of 1 kHz was installed on the seismometer output. Including this preamplifier the magnification level

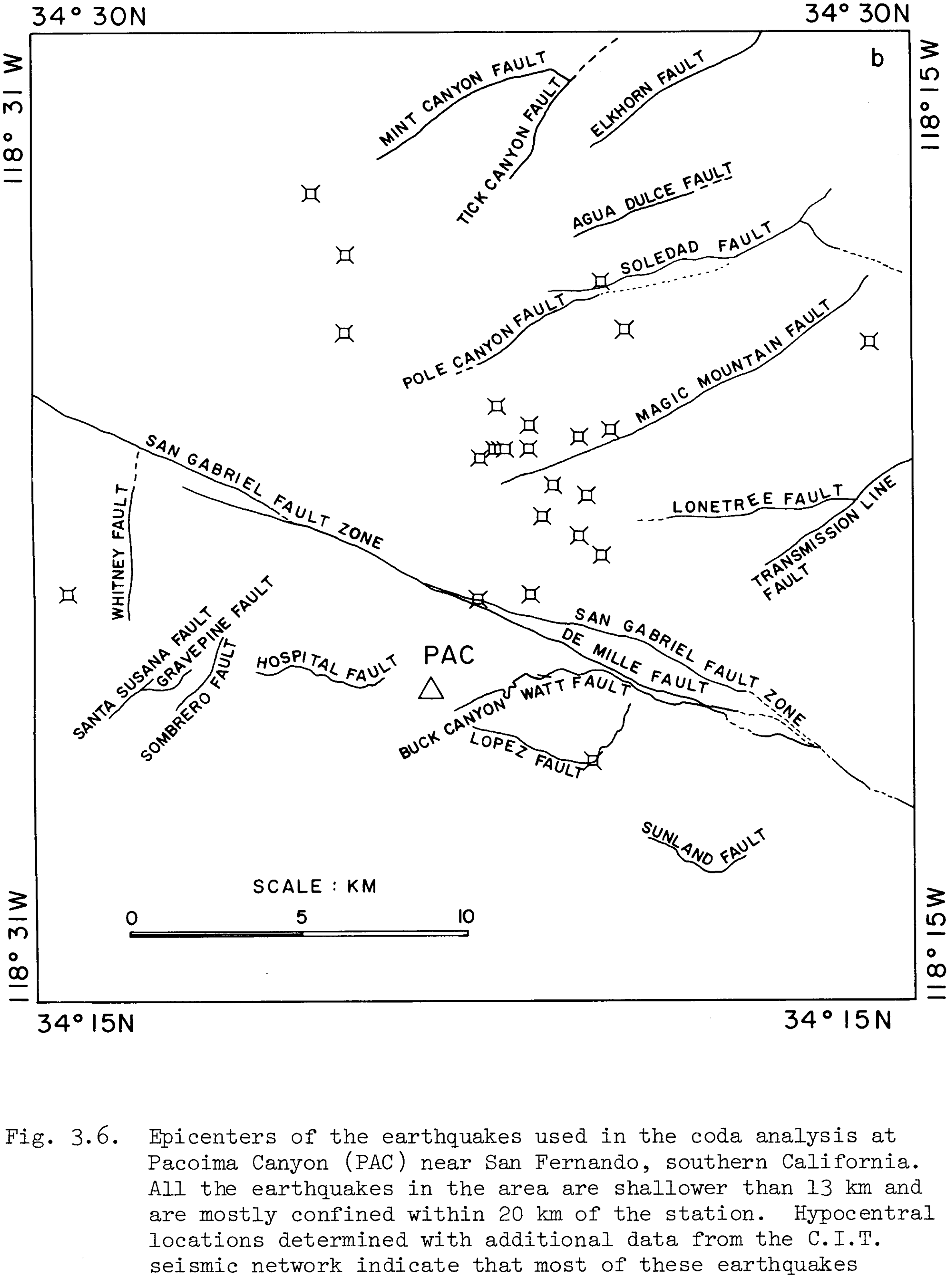

Fig. 3.6. Epicenters of the earthquakes used in the coda analysis at Pacoima Canyon (PAC) near San Fernando, southern California. All the earthquakes in the area are shallower than 13 km and are mostly confined within 20 km of the station. Hypocentral locations determined with additional data from the C.I.T. seismic network indicate that most of these earthquakes occurred off the major faults shown in the figure.

of the spectral analyzer was set at 1/8 of the maximum amplification shown in Fig. 3.1 and remained at this setting throughout the experiment. One hundred eleven earthquakes ranging in magnitude from 0.2 to 3.4 were selected from the seismograms obtained during the period of July 9 to August 12, 1975. The epicentral locations determined by the U.S. Geological Survey are shown in Fig. 3.7. The focal depths of these earthquakes are mostly shallower than 10 km, with a few events as deep as 25 to 30 km. All the epicenters are within 30 km from the station. The event parameters are listed in Table 4.

Two stations in western Japan were occupied with a spectral analyzing seismograph between 1969 and 1971. The station OIS (34°05'56"N, 130°19'00"E) at Oishiyama in the Kii peninsula was operated from July 10, 1970 until December 3, 1971 with the magnification set at 0.16 of the maximum amplification (Fig. 3.1). The station TSK (36°12'39"N, 140°06'35"E) at Tsukuba remained in operation from December 24, 1969 until August 15, 1971. The magnification level for this station was set at 0.13 of the maximum gain shown in Fig. 3.1. Forty four earthquakes, shallower than 10 km, with epicentral distances shorter than 30 km, and ranging in magnitude from 1.8 to 4.3 were selected from the data collected at Oishiyama (Fig. 3.8). A list of these events is given in Table 5. The focal depths of the earthquakes near Tsukuba (Fig. 3.9) range from 20 to 90 km

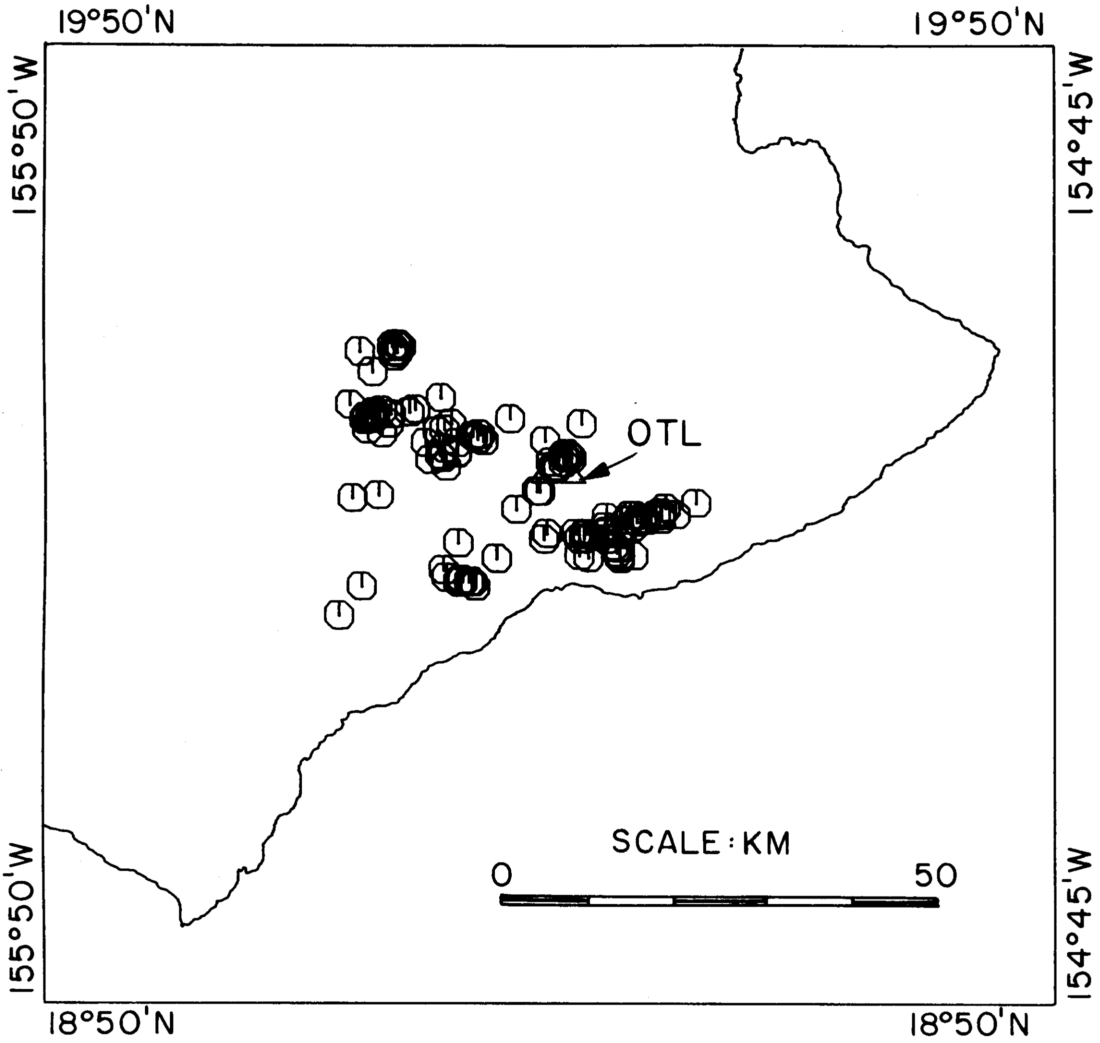

Fig. 3.7. Epicenters of the earthquakes used in the coda analysis at Kilauea (OTL) on the island of Hawaii. Focal depths are mostly shallower than 10 km with a few earthquakes as deep as 25 to 30 km. All the epicenters are within 30 km from the station.

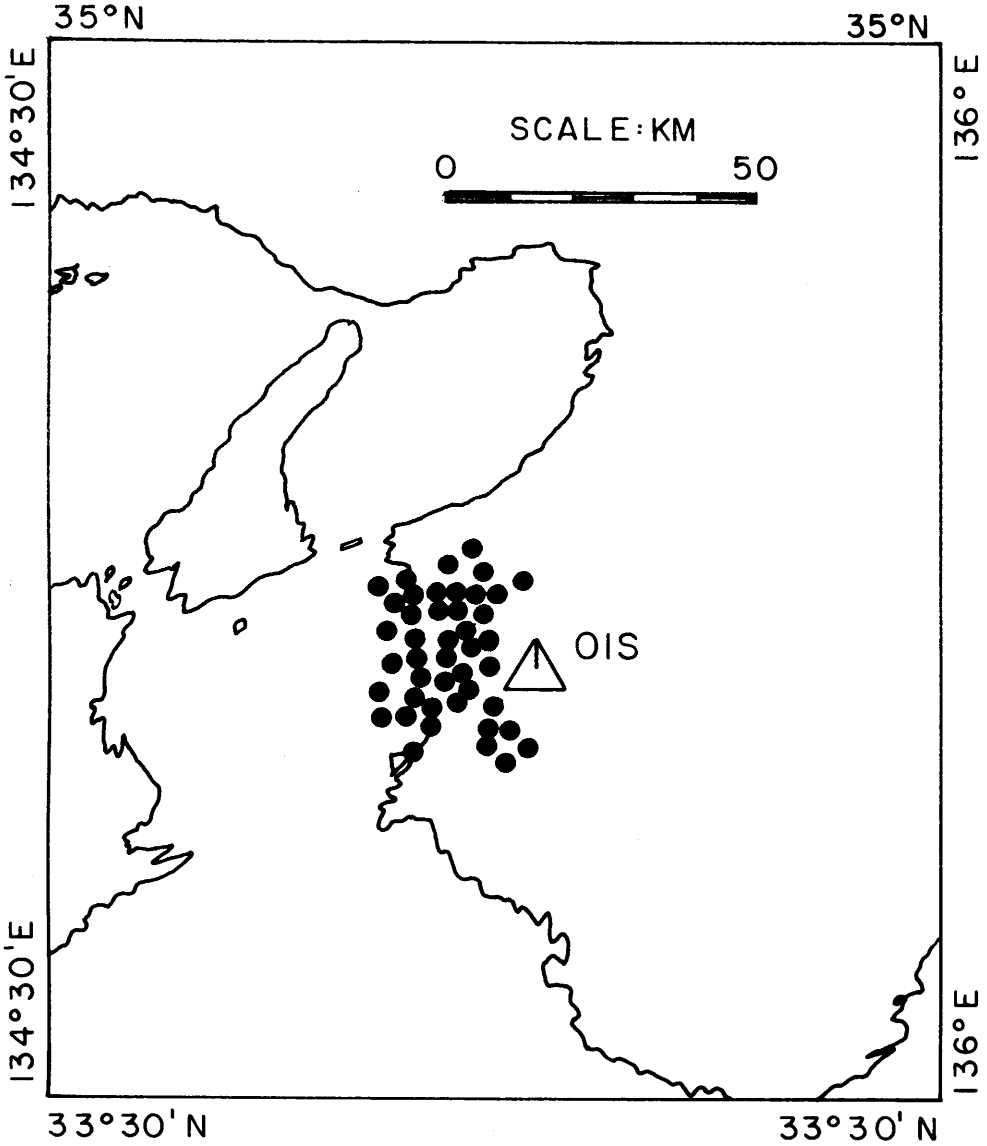

Fig. 3.8. Epicenters of earthquakes near Oishiyama (OIS), Japan, used in the coda analysis. All epicenters are within 30 km of the station and focal depths are shallower than 10 km.

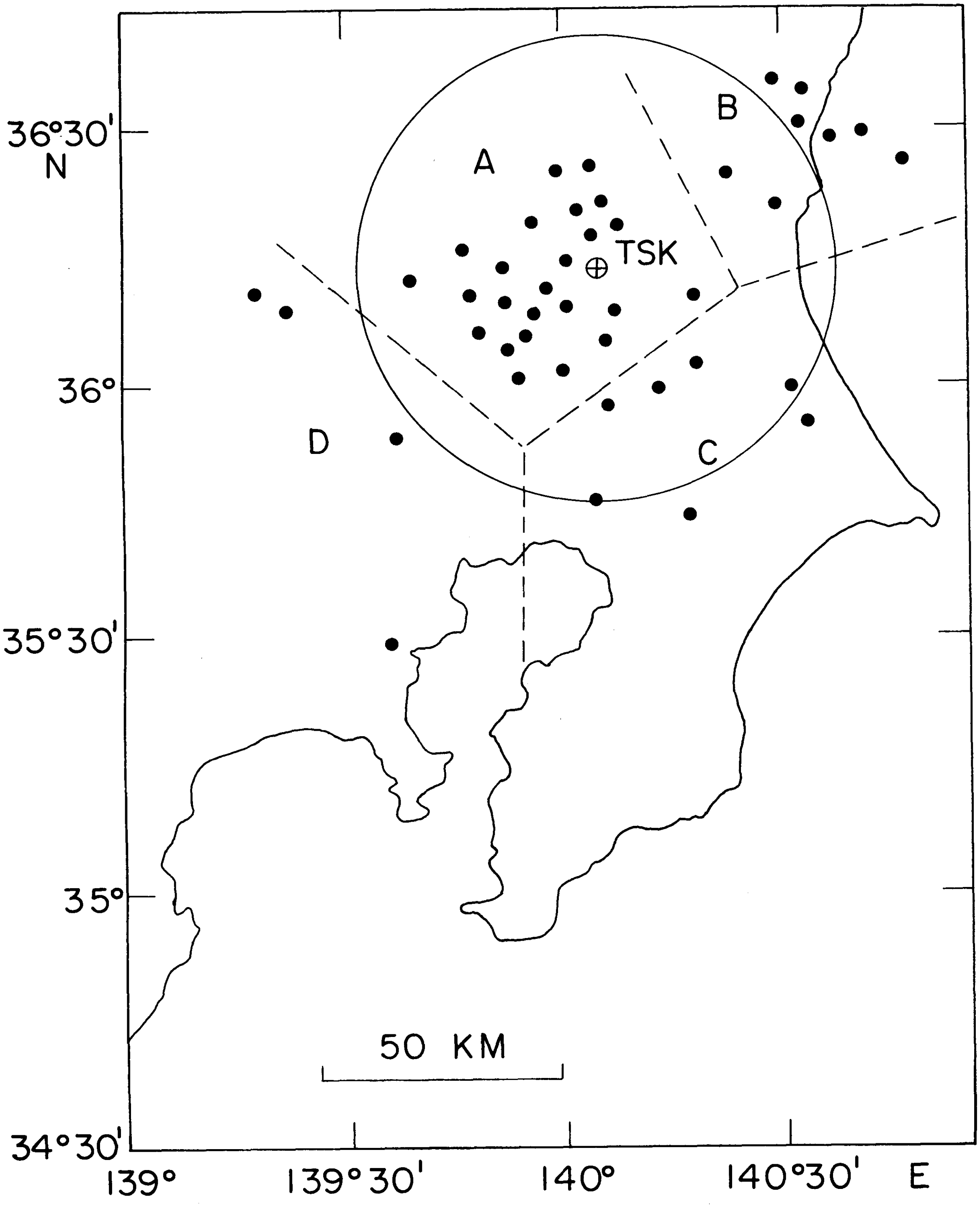

Fig. 3.9. Epicenters of earthquakes near Tsukuba (TSK), Japan, used in the coda analysis. Most epicenters are within a radius of 50 km from the station. Hypocentral depths vary from 20 to 90 km.

and most of their epicenters are within a radius of 50 km from the station. The 43 events we selected cover the magnitude range from 2.6 to 5.5. They are listed in Table 6.

During 6 months, from September 1975 until March 1976, the spectral analyzer was set up in the vault of the M.I.T. Wallace Geophysical Observatory, in eastern Massachusetts. But to our surprise, no local earthquakes were observed in the area during the entire period of operation.

3.2 Data preparation

The envelopes of the coda amplitudes, smoothed manually, were measured from the chart records using an x-y digitizer (1/1000 in. grid resolution). At Stone Canyon, Bickmore Canyon, Oishiyama, and for the coda traces at 0.75, 1.5, and 3 Hz at Kilauea, samples were taken every 2 sec. At San Fernando and for the coda at 6, 12, and 24 Hz in Hawaii, the sampling rate was increased to 1 sample/sec. For the larger events of Tuskuba, one sample was taken every 10 sec. Noise levels were compared before and after each event, and corrections were applied when it was necessary. The thickness of the pen traces, which varied throughout the records was also corrected for. To avoid bias caused by the pen offset which remained in the trace of some channels after the recording of a large event, the coda amplitudes were always referred to the pen trace following the event. The beginning of the digital recording of coda amplitudes was arbitrarily chosen at a point in the seismogram where the seismic signal started to decay in a regular manner. Following digitizing, the amplitude traces were plotted to scale and superposed onto the original coda to check for errors in the sampling process. The records were verified by this method down to a minimum amplitude of about 1 mm. After this preliminary test, time corrections were applied to each channel data to account for the slightly different lengths of the chart recorder pen. Finally, the time series were calibrated to ground displacement amplitudes and interpolated to give samples at integer time units of 1, 2, or 10 sec referred to the earthquake origin time. These coda traces were then replotted on a logarithmic scale (see for example Figs. 3.10, 3.11, and 3.12) to check the tail end of the digitized signal which was not considered in the earlier plots. Because of the loss of accuracy in digitizing the very small amplitudes and shallow slope of the decaying signal at the end of the coda, the last few samples from the time series were usually deleted. For the Hawaiian data, a lower threshold based on the logarithmic plots was established on each channel, below which the remaining samples were removed. The minimum ground displacement amplitudes corresponding to these thresholds were 20 millimicrons at 1.5 Hz, 10 millimicrons at 3 Hz, and 5, 3, and 1 millimicron at 6, 12, and 24 Hz, respectively.

The digitized coda were recorded on tape, one separate file being used for the entire data set from each channel filter for a given area. The tapes were then processed by least squares as described in the next section.

3.3 Data processing

In order to relate the coda amplitudes measured on the records to the coda power defined in equations (2.11) and (2.15), we use the well-known property that the Fourier transform of a power spectrum is the autocorrelation function

$$\phi(\tau) = \langle f(t)f(t+\tau)\rangle = \frac{1}{2\pi}\int_{-\infty}^{\infty} P(\omega|t)e^{i\omega\tau}d\omega \qquad (3.1)$$

For zero lag the autocorrelation function is the mean square of the time series

$$\phi(o) = \langle f^2(t)\rangle \qquad (3.2)$$

In our case of transient time series the mean square may be estimated from a short time sample around a given absolute time. We now write

$$\langle f^2(t)\rangle = \frac{1}{2\pi}\int_{-\infty}^{\infty} P(\omega|t)d\omega \qquad (3.3)$$

Then for a band-passed signal with $P(\omega|t) = P$ (constant) for $\omega_o<|\omega|<\omega_1$ and $P(\omega|t) = 0$ otherwise, we have

$$<f^2(t)> = 2P\Delta f \qquad (3.4)$$

where $\Delta f = (\omega_1 - \omega_o)/2\pi$.

Thus for a rough approximation the mean square amplitude is equal to the product of the power spectral density and the bandwidth. Since our manually smoothed amplitude, $A(\omega|t)$, corresponds roughly to the RMS value of the signal, we write

$$A(\omega|t) = [2P(\omega|t)\Delta f]^{1/2} \qquad (3.5)$$

where Δf is the bandwidth of the filter on the particular channel considered and $P(\omega|t)$ is the coda power defined previously.

As is discussed in the preceding chapter either for the single scattering model or for the diffusion model, the coda power $P(\omega|t)$ will take the following simple form as a function of time measured from the earthquake origin time:

$$P(\omega|t) = S(\omega)t^{-m}e^{-\omega t/Q} \qquad (2.11)$$

Inserting (2.11) into (3.5), we now express the coda amplitude $A(\omega|t)$:

$$A(\omega|t) = c(\omega)t^{-a}e^{-\omega t/2Q} \qquad (3.6)$$

where $c(\omega)$ represents the source term at a particular frequency ω, a is a constant that depends on the geometrical spreading, and Q is the quality factor. From equations (2.11) and (3.5), $a = m/2$ and $c(\omega)$ is related to the source factor of coda $S(\omega)$ by the relation

$$c(\omega) = [2S(\omega)\Delta f]^{1/2} \qquad (3.7)$$

Taking the logarithm of both sides in formula (3.6) we obtain

$$\log_{10}A(\omega|t) = C(\omega) - a\log_{10}t - bt \qquad (3.8)$$

where $C(\omega) = \log_{10} c(\omega)$ and b is related to the quality factor Q by the relation

$$b = (\log_{10}e)\,\frac{\pi f}{Q} \qquad (3.9)$$

To separate out the effects of source factor , geometrical spreading and attenuation in our coda data, we shall use the method of least squares. Treating each channel filter output separately and considering simultaneously all the events of an ensemble of earthquakes recorded on a given channel we rewrite equation (3.8) as

$$\log_{10} {}^{n}A_{ij} = {}^{n}C_{j} - {}^{n}a\log_{10}t_{i} - {}^{n}bt_{i},\ n = 1,\ldots 6 \qquad (3.10)$$

where ${}^{n}A_{ij}$ is the amplitude of the jth earthquake measured at time t_i from origin time for the nth frequency band around f_n. For convenience we now express (3.10) in a matrix form

$$h_{\ell} = U_{\ell(m+2)} \cdot p_{(m+2)} \tag{3.11}$$

where h is the vector of the recorded amplitudes, of dimension ℓ, U is a matrix of dimension $\ell(m + 2)$ and p is the vector of the parameter ${}^{n}a$, ${}^{n}b$ and ${}^{n}C_j$; here m represents the total number of events considered for processing, and ℓ is the total number of samples considered, for all the events, on one particular channel.

The system of equations given by (3.11) has a least square solution which minimizes the scalar quantity

$$\begin{aligned} \eta^2 &= \widetilde{(Up - h)}(Up - h) \\ &= \tilde{p}\tilde{U}Up - 2\tilde{p}\tilde{U}h + \tilde{h}h \end{aligned} \tag{3.12}$$

where η^2 is the square of the residual vector $\eta = Up - h$. The minimization of η^2 yields

$$\tilde{U}Up = \tilde{U}h \tag{3.13}$$

in which the matrix $\tilde{U}U$ is the symmetric matrix of the normal equations, of dimensions (m + 2)(m + 2). Proceeding with the inversion, we obtain

$$p = (\tilde{U}U)^{-1}\tilde{U}h \tag{3.14}$$

The extended formulation of equation (3.14) is given in the Appendix for both choices of the parameter a set free or fixed. When a is free we obtain the least square error estimates

$$(\delta p_r)^2_{RMS} \simeq (\tilde{U}U)^{-1}_{rr} \frac{\sum_i [\overline{R}(t_i)]^2}{\ell-(m+2)} \tag{3.15}$$

where (m + 2) represents the number of independent coordinate functions and $\overline{R}(t_i)$ is the residual of the function at the point t_i. Similarly, when the factor a in equation (3.8) is fixed, we compute the error estimates

$$(\delta p_r)^2_{RMS} \simeq (\tilde{U}U)^{-1}_{rr} \frac{\sum_i [\overline{R}(t_i)]^2}{\ell-(m+1)} \tag{3.16}$$

The error δQ^{-1} is then estimated using equation (3.9):

$$\delta Q^{-1} \simeq \frac{\delta b}{\pi f \log_{10} e} \tag{3.17}$$

3.4 Preliminary results

In solving the least squares problem, provisions were made in the computation for different choices of the spreading factor a: a = free, a = 0.5, or a = 1 (see Appendix). The matrix inversion in equation (3.14) was achieved using the standard Gauss-Jordan elimination method in a double precision routine. To improve the precision of the inversion, and also to test the variability of the least squares estimates in the larger data sets from Stone Canyon and Kilauea the maximum number of earthquakes simultaneously considered for a fit was limited to 50.

Computed residuals show that the coda amplitudes can be expressed by formula (3.8) within errors on the average better than 10% when the parameter a is fixed to the values 0.5 or 1. As shown in Figures 2.1, 3.2, and 3.3 the amplitude decay curve of the coda is very regular. It is also reproducible for many earthquakes of different magnitudes at various frequencies, as illustrated by Figures 3.10, 3.11, and 3.12 for the region of Tsukuba. This observation, along with similar observations made in the other areas that we studied, supports our assumption that both factors a and b are independent of the location of epicenter and of the magnitude of the earthquake. The values computed for the factor a (Table 7), however, are much more uncertain. The different regions yield values of a from about 0 to 3 with slightly more stable values of 0.5 - 1.5 being

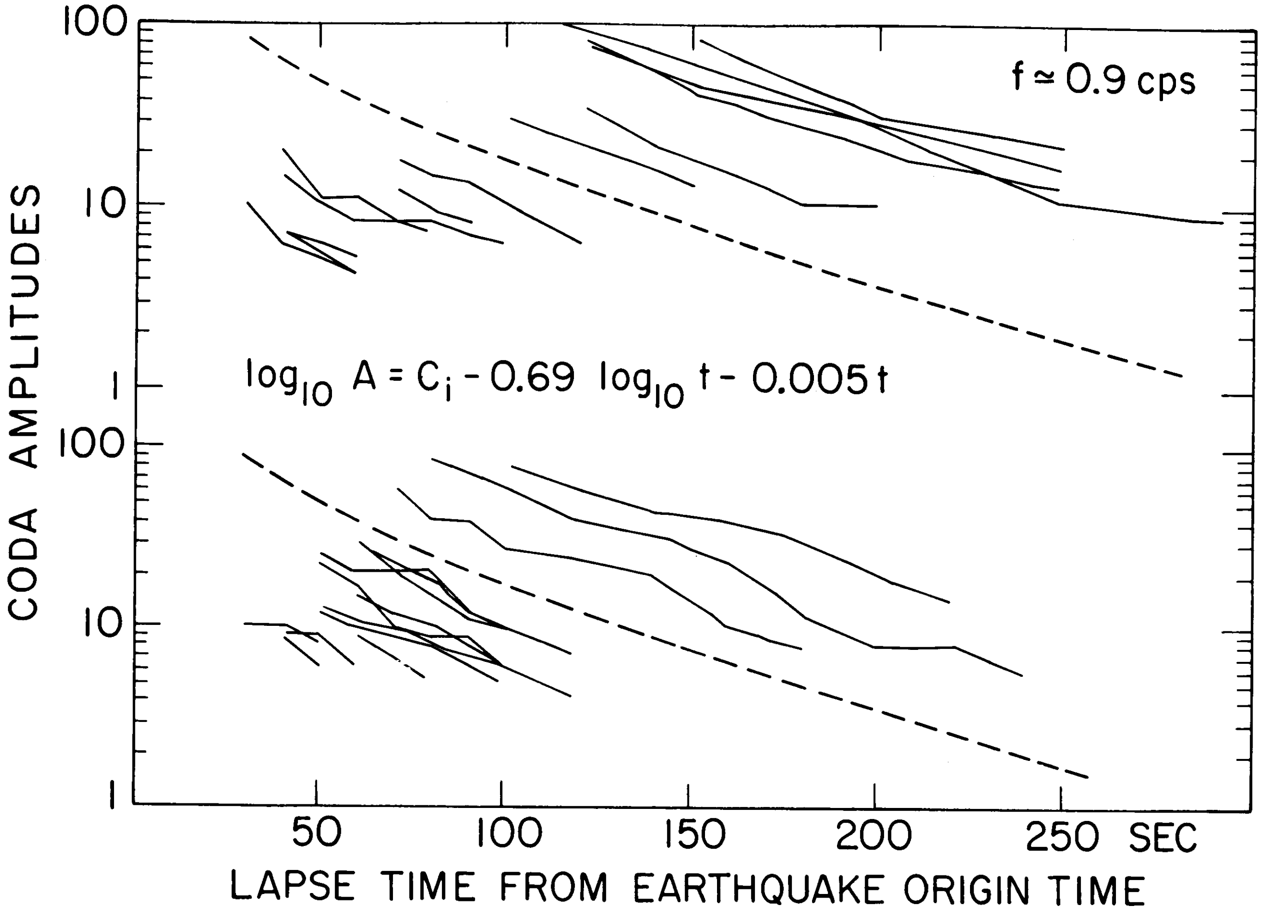

Fig. 3.10. Amplitude decay traces of coda waves measured at 0.9 Hz from earthquakes near Tsukuba, Japan. The dashed lines represent the function $\log_{10}A = C_i - 0.69 \log_{10}t - 0.005t$ obtained by fitting a standard decay curve to this ensemble of traces (see text for explanation of symbols and procedure).

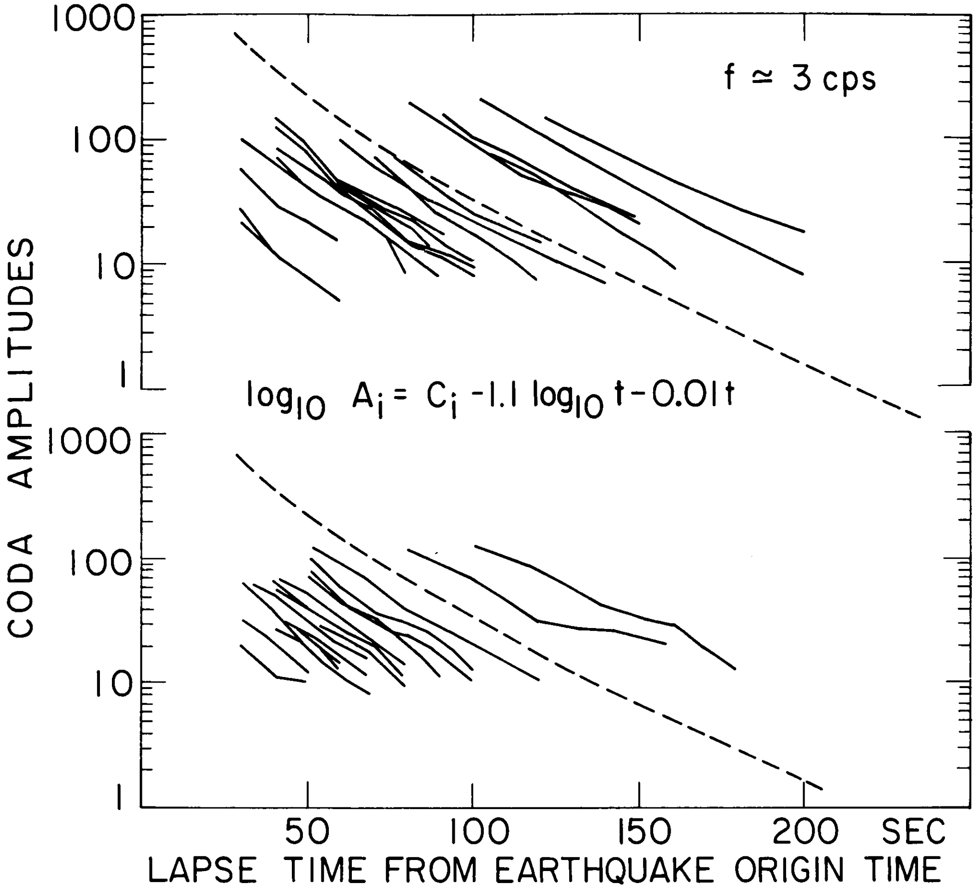

Fig. 3.11. Amplitude decay traces of coda waves at 3 Hz from earthquakes near Tsukuba, Japan. The dashed lines represent the function $\log_{10}A = C_i - 1.1 \log_{10}t - 0.01t$ obtained by fitting a standard decay curve to this ensemble of traces (see text for explanation of procedure).

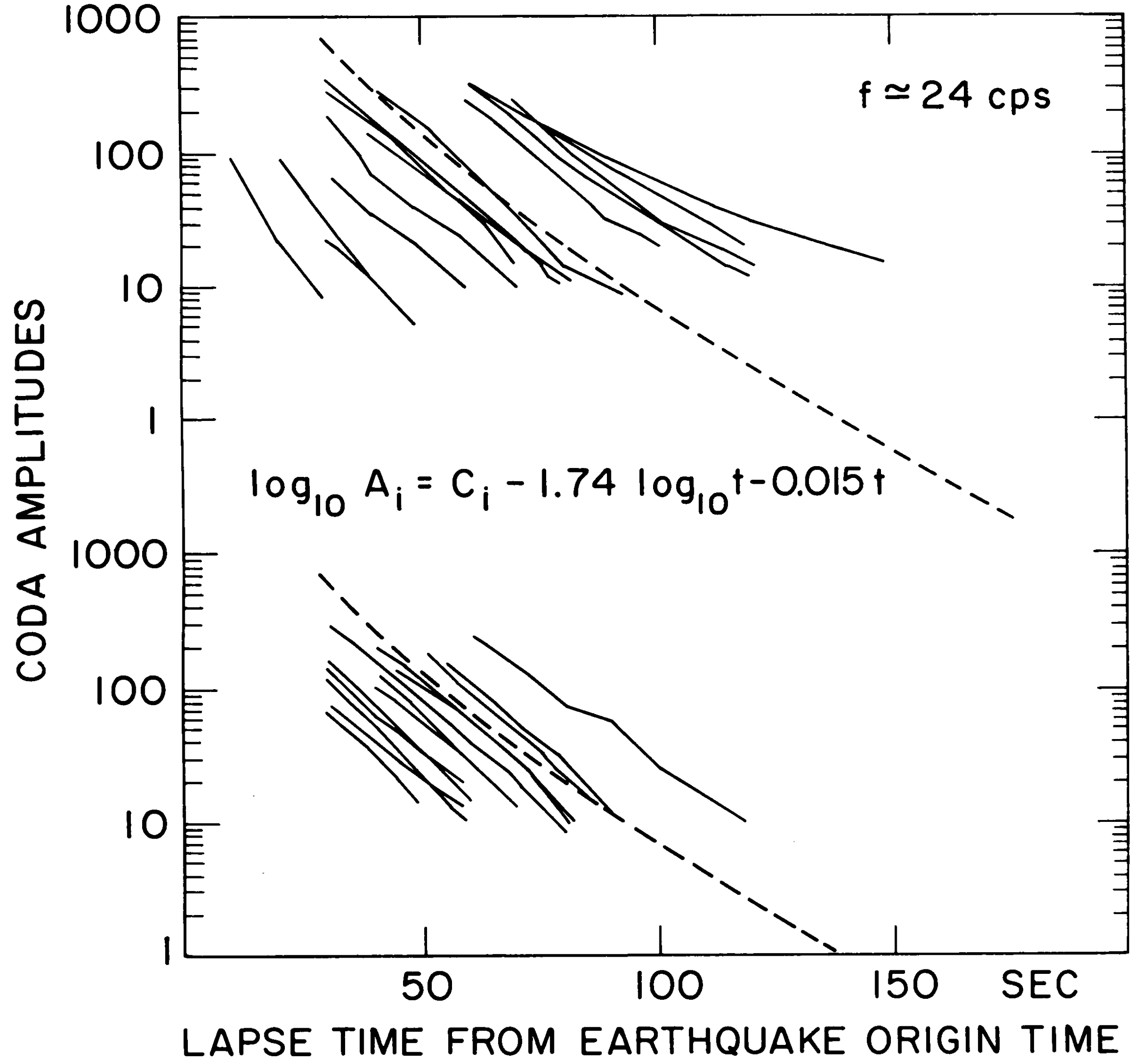

Fig. 3.12. Amplitude decay traces of coda waves at 24 Hz from earthquakes near Tsukuba, Japan. The dashed lines represent the function $\log_{10}A = C_i - 1.74 \log_{10}t - 0.015t$ obtained by fitting a standard decay curve to this ensemble of traces (see text for explanation of procedure). The extent of coda duration at this frequency is of special interest.

observed at the intermediate frequencies from 1.5 to 12 Hz. The erratic behavior of these estimates is understandable because a is very sensitive to the coda amplitude for small t, an amplitude which is not always well-defined. As we mentioned earlier the digital recording of the coda was arbitrarily started at a point where the signal began to decay in a regular manner. Unfortunately, the clipping introduced on some of the recorded events made the beginning of the coda for these earthquakes difficult to recognize. On the other hand, it is also probable that the early portion of the coda that we considered is contaminated by forward scattered waves which are not included in our simple formulation of the single-scattering model. In view of these difficulties, we cannot rely on the parameter a to separate out the different modes of scattering that we proposed. Fortunately, the estimates for b (Tables 8a, 8b, 8c) are not too sensitive to the uncertainty in the estimates of a because the function $a\log_{10}t$, although varying strongly for small t, varies much less than bt over most of the coda length. Indeed we shall find in Chapter 5 that the apparent Q of coda waves derived from b using (3.9) increases with frequency independent of the choice of a (see Figure 5.1).

At Stone Canyon the factor b is consistently smaller for earthquakes recorded during the first 2 months of the experiment than for events recorded later. The variation is particularly well-marked at high frequency and with a fixed to 0.5 or 1. Attempts to process the data after slightly altering the sizes of the sample spaces considered in the least squares procedure confirmed the statistical significance of this result. This interesting temporal variation will be further investigated in Chapter 5. In the next Chapter we shall bring our attention to the source factors of coda calculated for the various areas that we studied.

TABLE 1. Events Recorded at Stone Canyon (36°38'12"N, 121°15'18"W)*

Event	Date	Origin Time, UT	North Latitude	West Longitude	Depth, km	Magnitude
1	07/18/73	08h23m37.9s	36°33.6'	121°11.5'	8.1	2.8
2	07/18/73	22h52m47.9s	36°33.6'	121°11.5'	7.7	1.5
3	07/19/73	20h06m00.1s	36°34.3'	121°12.2'	7.3	2.0
4	07/20/73	15h54m26.6s	36°33.5'	121°11.4'	7.8	1.5
5	07/21/73	09h36m48.8s	36°37.6'	121°16.2'	5.6	2.0
6	07/21/73	09h57m11.0s	36°37.6'	121°16.2'	5.5	2.3
7	07/21/73	11h45m35.0s	36°31.6'	121°08.7'	5.1	2.3
8	07/21/73	14h20m26.3s	36°37.8'	121°16.4'	4.1	1.9
9	07/24/73	22h55m00.8s	36°35.1'	121°13.8'	8.2	1.7
10	07/26/73	17h21m28.2s	36°32.4'	121°09.5'	4.9	2.2
11	08/01/73	02h30m20.5s	36°39.9'	121°19.5'	5.5	2.0
12	08/02/73	16h10m42.3s	36°32.7'	121°10.5'	7.9	3.3
13	08/04/73	05h20m38.2s	36°35.8'	121°13.7'	4.5	1.5
14	08/05/73	16h56m48.7s	36°33.0'	121°10.5'	6.0	2.8
15	08/05/73	17h09m11.5s	36°32.9'	121°10.6'	6.1	2.0
16	08/05/73	20h45m38.5s	36°32.9'	121°10.5'	6.8	2.0
17	08/06/73	05h57m43.2s	36°36.5'	121°14.8'	5.1	2.1
18	08/08/73	15h51m05.5s	36°40.5'	121°20.0'	4.3	1.8
19	08/10/73	11h35m07.7s	36°35.9'	121°13.5'	3.7	3.1
20	08/17/73	16h41m48.3s	36°35.4'	121°13.8'	7.5	2.5
21	08/19/73	00h05m09.0s	36°33.8'	121°11.6'	6.3	2.3
22	08/20/73	07h33m23.1s	36°32.7'	121°10.8'	7.7	2.6
23	08/20/73	12h48m34.2s	36°32.9'	121°10.6'	7.7	1.8
24	08/20/73	17h35m14.2s	36°34.6'	121°12.6'	7.7	2.2
25	08/23/73	10h57m47.6s	36°33.8'	121°11.4'	3.7	2.1
26	09/02/73	04h54m08.6s	36°36.9'	121°14.9'	4.0	1.9
27	09/02/73	17h18m31.0s	36°42.3'	121°21.3'	1.9	2.2
28	09/03/73	03h38m29.5s	36°34.2'	121°12.6'	7.4	1.9
29	09/07/73	02h30m48.4s	36°37.5'	121°16.4'	4.0	1.1
30	09/08/73	22h08m55.3s	36°36.7'	121°14.9'	4.6	1.0
31	09/09/73	14h12m49.3s	36°38.2'	121°15.0'	7.0	1.0
32	09/09/73	16h08m07.9s	36°38.1'	121°17.3'	6.9	1.3
33	09/11/73	03h35m31.8s	36°31.0'	121°08.5'	9.2	2.1
34	09/11/73	03h38m23.6s	36°31.0'	121°08.6'	9.6	2.0
35	09/11/73	05h07m51.5s	36°33.5'	121°09.1'	6.4	2.1
36	09/11/73	19h11m21.9s	36°35.0'	121°13.6'	6.7	1.0

Table 1. (continued)

Event	Date	Origin Time, UT	North Latitude	West Longitude	Depth, km	Magnitude
37	09/12/73	16h37m57.4s	36°42.1'	121°21.7'	2.9	1.4
38	09/14/73	15h22m50.3s	36°32.7'	121°10.5'	5.7	1.6
39	09/20/73	06h29m09.3s	36°40.6'	121°20.3'	3.6	1.2
40	09/20/73	21h14m18.0s	36°38.7'	121°17.5'	4.1	1.7
41	09/22/73	14h29m22.3s	36°34.8'	121°13.4'	8.9	2.1
42	09/22/73	01h53m00.6s	36°33.3'	121°08.8'	13.5	1.7
43	09/22/73	21h10m38.2s	36°32.9'	121°11.0'	6.0	1.6
44	09/23/73	17h40m22.2s	36°37.9'	121°17.9'	11.9	1.0
45	09/23/73	23h06m35.5s	36°39.8'	121°19.2'	4.1	1.6
46	09/24/73	15h41m17.8s	36°34.7'	121°13.2'	7.7	1.7
47	09/25/73	09h42m31.3s	36°40.9'	121°21.0'	5.5	2.1
48	09/25/73	12h12m34.4s	36°33.4'	121°11.1'	7.9	1.5
49	09/27/73	03h07m02.5s	36°34.7'	121°12.4'	4.8	2.6
50	09/27/73	12h39m00.5s	36°38.3'	121°16.9'	4.9	1.1
51	09/27/73	19h28m19.6s	36°33.8'	121°11.5'	5.8	1.7
52	09/27/73	19h30m48.2s	36°33.9'	121°11.8'	5.9	2.3
53	10/03/73	23h52m43.7s	36°32.9'	121°10.8'	6.7	1.7
54	10/04/73	00h39m24.4s	36°32.9'	121°10.7'	7.3	1.6
55	10/04/73	05h37m14.9s	36°38.7'	121°17.9'	6.6	2.9
56	10/04/73	06h16m26.5s	36°38.7'	121°17.9'	5.4	1.6
57	10/04/73	06h50m15.3s	36°33.4'	121°11.3'	8.0	2.1
58	10/04/73	06h52m52.6s	36°39.0'	121°18.1'	4.0	1.0
59	10/04/73	07h10m59.9s	36°38.8'	121°18.1'	4.6	1.6
60	10/04/73	17h43m38.6s	36°38.7'	121°18.1'	6.3	2.3
61	10/08/73	00h30m01.1s	36°31.6'	121°09.2'	5.7	1.6
62	10/08/73	13h38m48.9s	36°36.2'	121°14.3'	4.5	2.2
63	10/09/73	02h18m14.4s	36°35.2'	121°13.8'	9.8	2.7
64	10/09/73	03h33m52.1s	36°34.3'	121°13.8'	9.2	2.6
65	10/10/73	00h46m39.1s	36°34.2'	121°11.9'	6.1	2.4
66	10/11/73	14h57m58.6s	36°34.2'	121°11.5'	2.9	2.7
67	10/12/73	19h19m06.6s	36°32.5'	121°10.5'	7.6	2.8

Table 1. (continued)

Event	Date	Origin Time, UT	North Latitude	West Longitude	Depth, km	Magnitude
68	10/13/73	17h59m33.1s	36°33.0'	121°08.3'	6.1	2.5
69	10/13/73	18h47m50.4s	36°35.6'	121°14.4'	8.8	1.4
70	10/14/73	16h57m00.1s	36°38.6'	121°17.8'	5.2	2.5
71	10/17/73	04h13m31.8s	36°39.5'	121°18.1'	4.0	1.9
72	10/21/73	14h35m33.3s	36°38.7'	121°17.6'	3.3	1.3
73	10/23/73	10h17m49.6s	36°38.0'	121°16.9'	5.4	1.9
74	10/24/73	03h47m16.8s	36°34.4'	121°12.8'	6.6	2.0
75	10/27/73	20h08m08.1s	36°35.9'	121°14.3'	2.2	2.8
76	10/29/73	11h31m31.8s	36°33.3'	121°11.0'	7.5	1.6
77	10/29/73	21h38m25.1s	36°34.8'	121°12.2'	3.4	2.5
78	10/29/73	22h21m48.8s	36°34.5'	121°12.3'	3.6	2.9
79	11/01/73	21h21m03.2s	36°36.0'	121°13.0'	1.1	1.7
80	11/05/73	11h18m39.6s	36°35.6'	121°13.8'	5.9	1.7
81	11/06/73	03h12m39.2s	36°35.7'	121°13.4'	3.6	2.2
82	11/06/73	15h22m57.1s	36°32.8'	121°10.7'	7.1	1.6
83	11/06/73	19h57m15.2s	36°35.5'	121°10.4'	8.7	1.8
84	11/07/73	17h46m46.4s	36°32.6'	121°10.5'	9.9	2.3
85	11/09/73	11h31m20.6s	36°31.8'	121°09.6'	7.1	2.2
86	11/10/73	01h44m10.5s	36°39.9'	121°19.2'	4.5	1.0
87	11/12/73	20h20m16.2s	36°35.1'	121°14.1'	6.3	1.8
88	11/15/73	09h48m09.1s	36°34.8'	121°13.0'	6.0	2.8
89	11/15/73	21h42m13.5s	36°34.6'	121°12.6'	6.5	2.1
90	11/22/73	05h07m57.5s	36°34.6'	121°12.7'	6.0	2.6
91	11/22/73	05h10m51.4s	36°34.5'	121°12.6'	6.1	1.4
92	11/22/73	05h44m31.5s	36°34.5'	121°12.5'	6.6	1.3
93	11/23/73	08h43m20.1s	36°34.5'	121°12.9'	5.9	1.4
94	11/25/73	04h34m55.6s	36°35.5'	121°13.1'	3.6	1.7
95	11/25/73	18h47m28.2s	36°33.4'	121°11.0'	4.7	1.5
96	11/26/73	01h53m03.0s	36°38.2'	121°16.3'	3.1	1.0
97	11/27/73	04h56m37.3s	36°37.9'	121°16.4'	5.3	1.9
98	12/09/73	23h51m59.7s	36°36.4'	121°14.9'	4.9	2.4

Table 1. (continued)

Event	Date	Origin Time, UT	North Latitude	West Longitude	Depth, km	Magnitude
99	12/11/73	19h40m06.4s	36°37.5'	121°15.9'	4.2	2.2
100	12/13/73	05h09m41.8s	36°34.4'	121°12.3'	4.8	2.8
101	12/13/73	18h28m00.2s	36°34.2'	121°12.2'	6.4	1.5
102	12/13/73	22h16m24.2s	36°34.2'	121°12.2'	6.1	2.7
103	12/13/73	22h17m43.2s	36°34.2'	121°12.1'	5.0	2.0
104	12/13/73	22h18m23.1s	36°34.1'	121°12.0'	5.2	1.9
105	12/14/73	11h57m58.2s	36°34.1'	121°12.0'	5.5	1.4
106	12/14/73	12h04m44.3s	36°39.9'	121°18.5'	8.9	2.6
107	12/14/73	12h31m46.5s	36°39.8'	121°18.6'	8.1	2.3
108	12/15/73	16h17m14.6s	36°33.8'	121°11.6'	5.7	2.0
109	12/17/73	13h44m46.1s	36°31.5'	121°08.9'	3.5	1.8
110	12/17/73	20h50m25.4s	36°40.0'	121°18.6'	9.8	1.3
111	12/20/73	22h32m19.4s	36°32.3'	121°10.4'	4.1	2.5
112	12/22/73	22h08m44.3s	36°40.9'	121°20.4'	4.4	1.9
113	12/22/73	22h09m39.0s	36°41.0'	121°20.5'	4.7	2.1
114	12/23/73	08h07m09.2s	36°32.0'	121°09.7'	7.2	2.3
115	12/26/73	16h58m43.7s	36°40.9'	121°20.1'	5.1	1.8
116	01/05/74	17h27m18.9s	36°38.8'	121°17.8'	1.8	1.1
117	01/06/74	01h12m17.1s	36°38.2'	121°17.0'	1.4	1.3
118	01/06/74	04h55m54.1s	36°39.8'	121°19.4'	5.2	2.1
119	01/14/74	05h38m26.6s	36°32.5'	121°11.0'	7.4	2.2
120	01/14/74	06h56m34.1s	36°32.6'	121°11.1'	7.3	2.3
121	01/14/74	07h43m10.2s	36°42.9'	121°22.4'	3.0	1.7
122	01/16/74	15h32m59.6s	36°32.7'	121°11.1'	7.0	1.9
123	01/16/74	22h26m43.6s	36°33.0'	121°11.8'	7.1	1.9
124	01/16/74	23h00m47.2s	36°33.5'	121°11.4'	7.2	2.0
125	01/22/74	00h05m15.3s	36°39.8'	121°19.7'	5.2	2.0
126	01/22/74	19h01m11.9s	36°31.9'	121°10.2'	6.7	1.7
127	01/25/74	20h27m56.2s	36°38.0'	121°16.6'	4.5	1.8
128	01/27/74	13h34m34.8s	36°34.6'	121°12.3'	3.6	1.6
129	01/27/74	19h22m13.7s	36°35.3'	121°14.0'	6.9	2.7

Table 1. (continued)

Event	Date	Origin Time, UT	North Latitude	West Longitude	Depth, km	Magnitude
130	02/01/74	09h17m24.4s	36°38.6'	121°17.5'	6.6	1.0
131	02/05/74	04h19m51.2s	36°32.9'	121°10.9'	7.1	1.9
132	02/05/74	14h57m16.1s	36°32.2'	121°10.4'	7.5	2.1
133	02/06/74	09h37m22.7s	36°38.5'	121°16.5'	7.3	1.8
134	02/09/74	04h47m18.2s	36°33.7'	121°11.4'	5.8	1.8
135	02/09/74	13h57m11.4s	36°33.2'	121°09.3'	10.6	1.9
136	02/10/74	04h57m24.5s	36°32.3'	121°10.4'	8.4	2.4
137	02/10/74	04h59m24.4s	36°32.3'	121°10.2'	7.5	
138	02/10/74	05h11m07.3s	36°32.5'	121°10.3'	6.7	0.9
139	02/13/74	16h15m54.7s	36°38.3'	121°16.4'	4.1	1.4
140	02/14/74	23h10m44.6s	36°30.7'	121°08.7'	9.5	1.7
141	02/20/74	10h55m16.3s	36°36.4'	121°11.9'	8.4	2.8
142	02/25/74	03h46m33.7s	36°42.8'	121°22.3'	3.0	2.0
143	02/28/74	05h40m06.1s	36°41.4'	121°21.2'	4.6	2.3
144	02/28/74	07h52m22.5s	36°41.7'	121°21.3'	4.4	2.2
145	03/04/74	17h51m01.6s	36°35.6'	121°14.6'	8.1	1.4
146	03/08/74	18h55m15.0s	36°38.2'	121°17.6'	4.2	2.8
147	03/08/74	18h56m19.0s	36°38.3'	121°17.6'	4.2	2.9
148	03/08/74	19h10m14.9s	36°38.3'	121°17.5'	4.3	3.1
149	03/10/74	12h27m28.2s	36°34.4'	121°12.4'	5.0	1.9
150	03/13/74	04h21m49.9s	36°34.4'	121°12.4'	3.6	2.2
151	03/14/74	01h05m02.1s	36°38.9'	121°18.7'	7.5	1.3
152	03/14/74	13h54m26.0s	36°32.0'	121°10.2'	7.4	2.2
153	03/17/74	00h29m36.4s	36°33.1'	121°11.1'	3.6	2.5
154	03/27/74	21h13m26.4s	36°42.2'	121°22.4'	3.7	1.5
155	03/30/74	00h25m47.1s	36°34.2'	121°12.1'	5.6	2.0
156	04/05/74	01h01m34.4s	36°34.3'	121°12.8'	6.4	2.0
157	04/07/74	10h47m40.8s	36°33.2'	121°11.2'	3.6	3.0
158	04/07/74	22h07m32.4s	36°32.5'	121°08.0'	9.7	2.8
159	04/09/74	16h37m31.6s	36°34.6'	121°13.0'	4.8	2.8
160	04/10/74	08h46m11.9s	36°36.4'	121°14.1'	3.5	1.7

Table 1. (continued)

Event	Date	Origin Time, UT	North Latitude	West Longitude	Depth, km	Magnitude
161	04/14/74	16h07m33.3s	36°35.4'	121°12.4'	1.0	2.0
162	04/19/74	09h34m32.3s	36°34.2'	121°09.5'	11.1	2.3
163	04/19/74	13h56m47.0s	36°34.1'	121°09.5'	11.1	2.4
164	04/25/74	19h05m53.1s	36°35.5'	121°14.6'	9.9	2.5
165	04/28/74	12h38m22.5s	36°31.9'	121°08.8'	9.0	2.2
166	04/30/74	05h45m06.4s	36°34.4'	121°12.8'	5.3	2.8
167	05/04/74	03h47m30.6s	36°30.9'	121°08.0'	11.1	3.1
168	05/04/74	04h35m22.9s	36°31.1'	121°07.9'	11.0	2.5
169	05/05/74	19h40m02.1s	36°39.2'	121°18.4'	2.1	1.9
170	05/06/74	08h36m35.8s	36°30.9'	121°08.2'	9.8	2.0
171	05/08/74	02h56m44.2s	36°39.5'	121°19.3'	3.9	2.0
172	05/15/74	20h02m59.5s	36°41.4'	121°19.6'	11.7	2.0
173	05/20/74	16h31m26.9s	36°33.3'	121°08.9'	10.7	1.7
174	05/24/74	00h16m11.6s	36°33.0'	121°11.2'	6.0	1.7
175	05/24/74	00h20m34.9s	36°33.3'	121°11.0'	5.7	1.6
176	05/28/74	19h59m14.3s	36°33.2'	121°11.3'	5.0	2.0
177	05/28/74	23h18m46.9s	36°31.1'	121°08.4'	9.8	2.3
178	06/09/74	23h36m53.3s	36°35.0'	121°14.5'	8.4	2.1
179	06/10/74	00h03m56.6s	36°35.0'	121°14.4'	8.4	3.0
180	06/10/74	05h12m11.4s	36°35.2'	121°14.5'	8.5	2.2
181	06/21/74	06h24m27.4s	36°37.9'	121°16.5'	4.1	1.5
182	06/21/74	15h18m40.5s	36°35.7'	121°10.5'	9.8	1.7
183	06/22/74	10h48m06.8s	36°38.5'	121°18.1'	4.3	2.0
184	06/24/74	00h36m26.9s	36°39.8'	121°19.8'	5.5	2.7
185	06/24/74	01h42m06.3s	36°40.0'	121°19.6'	1.6	1.8

* Event parameters determined by U.S.G.S.

TABLE 2. Events Recorded at Bickmore Canyon (36°33'38.4"N, 121°12'21"W)*

Event	Date	Origin Time, UT	North Latitude	West Longitude	Depth, km	Magnitude
1	1/15/73	09h43m29.9s	36°40.3'	121°20.0'	6.3	4.1
2	1/15/73	10h08m32.9s	36°40.3'	121°19.9'	6.1	2.9
3	1/15/73	10h13m38.9s	36°40.6'	121°20.4'	6.8	3.2
4	1/15/73	10h23m52.3s	36°40.7'	121°19.6'	5.8	3.7
5	1/15/73	10h24m48.1s	36°40.3'	121°20.2'	5.9	3.3
6	1/15/73	14h41m22.4s	36°40.1'	121°19.8'	6.4	3.7
7	1/15/73	15h19m26.1s	36°40.7'	121°20.5'	6.1	2.8
8	1/15/73	15h30m08.7s	36°39.6'	121°19.1'	6.3	2.9
9	1/15/73	19h22m31.5s	36°39.8'	121°19.5'	7.4	2.8
10	1/15/73	20h13m46.7s	36°39.6'	121°19.0'	6.6	3.3
11	1/15/73	20h17m04.5s	36°39.7'	121°19.1'	5.5	2.9
12	1/15/73	21h14m50.9s	36°39.4'	121°18.9'	5.9	3.4
13	1/15/73	21h15m36.4s	36°39.6'	121°19.1'	5.7	2.9
14	2/04/73	04h19m24.7s	36°40.4'	121°19.8'	5.8	1.8
15	2/05/73	10h39m21.4s	36°38.4'	121°18.0'	6.2	2.3
16	2/13/73	17h30m12.4s	36°38.5'	121°17.7'	0.1	2.2
17	2/13/73	17h41m08.3s	36°38.7'	121°17.6'	4.7	3.3
18	2/13/73	17h46m48.0s	36°38.8'	121°17.6'	4.4	2.9

* Event parameters determined by U.S.G.S.

TABLE 3. Events Recorded at San Fernando (34°19'46.7"N, 118°23'51"W)*

Event	Date	Origin Time, UT	North Latitude	West Longitude	Depth, km	Magnitude
1	7/16/74	09h48m18.5s	34°27.5'	118°26.0'	10.1	
2	7/23/74	21h30m51.0s	34°23.7'	118°21.1'	6.0	
3	7/23/74	21h31m45.4s	34°23.8'	118°20.5'	5.1	
4	7/24/74	03h35m57.2s	34°26.5'	118°25.4'	12.5	
5	7/25/74	20h39m55.7s	34°25.3'	118°25.4'	2.2	
6	8/14/74	15h21m25.5s	34°23.5'	118°22.6'	9.7	1.9
7	8/14/74	15h32m18.3s	34°21.3'	118°30.4'	1.6	
8	8/14/74	21h57m06.6s	34°21.9'	118°20.7'	4.1	
9	8/14/74	21h57m17.7s	34°23.0'	118°21.6'	5.9	
10	8/15/74	11h55m08.8s	34°23.5'	118°22.0'	6.4	2.0
11	8/15/74	13h46m48.7s	34°23.5'	118°22.0'	8.0	3.0
12	8/15/74	13h50m02.4s	34°21.3'	118°22.0'	3.6	
13	8/15/74	13h52m50.6s	34°23.4'	118°22.9'	8.0	2.8
14	8/15/74	14h02m08.5s	34°22.5'	118°21.8'	5.5	1.7
15	8/15/74	18h56m11.3s	34°22.8'	118°21.0'	8.0	
16	8/15/74	20h39m40.6s	34°23.0'	118°21.6'	5.1	
17	8/15/74	22h25m38.4s	34°22.2'	118°21.1'	4.2	
18	8/16/74	05h36m18.7s	34°23.9'	118°22.0'	9.0	
19	8/17/74	09h56m13.6s	34°25.2'	118°15.8'	8.0	
20	8/18/74	19h39m15.3s	34°23.5'	118°22.7'	8.0	
21	8/19/74	20h00m07.3s	34°21.2'	118°23.0'	3.3	
22	8/20/74	23h43m27.9s	33°53.5'	117°40.5'	6.7	3.0
23	8/21/74	20h20m21.6s	34°18.7'	118°20.9'	1.7	
24	8/26/74	14h36m52.5s	34°23.5'	118°22.5'	8.0	
25	8/31/74	21h57m56.5s	34°26.1'	118°20.7'	3.5	
26	9/01/74	16h27m16.0s	34°25.4'	118°20.3'	10.5	
27	9/02/74	16h04m31.2s	34°24.2'	118°22.6'	4.7	

* Event parameters determined with additional data from the C.I.T. seismic network in southern California.

TABLE 4. Events Recorded at Kilauea (19°23'22.8"N, 155°16'56.4"W)*

Event	Date	Origin Time, UT	North Latitude	West Longitude	Depth, km	Magnitude
1	07/09/75	23h34m23.7s	19°31.2'	155°27.3'	6.6	3.4
2	07/10/75	00h02m19.5s	19°20.1'	155°11.9'	5.7	2.3
3	07/10/75	03h55m49.4s	19°26.9'	155°27.8'	7.8	2.5
4	07/10/75	05h38m26.7s	19°30.7'	155°27.4'	6.6	3.2
5	07/10/75	06h21m32.3s	19°19.5'	155°13.1'	6.8	2.5
6	07/10/75	08h02m11.9s	19°26.5'	155°29.5'	8.3	2.5
7	07/10/75	17h35m27.9s	19°31.1'	155°27.2'	7.3	3.0
8	07/10/75	18h16m37.3s	19°30.5'	155°27.6'	6.5	2.9
9	07/11/75	00h39m42.3s	19°25.9'	155°29.3'	8.6	2.2
10	07/11/75	02h15m12.6s	19°30.8'	155°27.6'	6.4	2.5
11	07/11/75	04h53m25.5s	19°30.8'	155°29.8'	7.1	2.5
12	07/11/75	07h33m07.5s	19°26.6'	155°28.9'	8.0	2.9
13	07/11/75	09h00m10.7s	19°26.7'	155°29.1'	8.2	2.1
14	07/11/75	09h19m00.0s	19°26.8'	155°28.9'	8.3	2.3
15	07/12/75	10h00m19.2s	19°24.5'	155°23.5'	7.9	1.6
16	07/12/75	16h39m39.0s	19°31.1'	155°27.7'	6.9	3.0
17	07/13/75	03h06m13.5s	19°24.1'	155°16.5'	12.9	2.5
18	07/13/75	03h10m12.3s	19°24.2'	155°16.6'	13.0	2.3
19	07/13/75	04h04m14.4s	19°23.8'	155°16.6'	14.4	1.6
20	07/13/75	12h31m52.5s	19°25.1'	155°25.5'	9.2	2.3
21	07/13/75	16h11m13.0s	19°20.5'	155°12.3'	6.7	2.1
22	07/13/75	16h48m59.0s	19°20.5'	155°10.7'	6.4	2.1
23	07/13/75	16h49m40.9s	19°20.2'	155°11.3'	4.5	1.7
24	07/14/75	03h03m21.6s	19°21.8'	155°28.5'	7.7	2.0
25	07/14/75	03h43m06.0s	19°25.9'	155°24.3'	7.3	1.5
26	07/14/75	10h07m17.0s	19°18.0'	155°15.6'	6.7	2.0
27	07/14/75	10h32m49.0s	19°19.4'	155°15.8'	6.1	1.7
28	07/14/75	11h06m54.7s	19°20.7'	155°10.3'	6.1	1.7
29	07/15/75	00h48m24.1s	19°24.4'	155°23.5'	7.7	1.3
30	07/15/75	07h50m13.1s	19°20.3'	155°11.5'	7.5	2.0

Table 4. (continued)

Event	Date	Origin Time, UT	North Latitude	West Longitude	Depth, km	Magnitude
31	07/15/75	13h45m23.4s	19°19.1'	155°15.3'	6.4	1.9
32	07/15/75	14h20m13.4s	19°18.5'	155°13.2'	7.1	2.1
33	07/15/75	20h36m00.9s	19°18.6'	155°13.4'	5.7	1.7
34	07/15/75	20h37m33.3s	19°18.2'	155°13.2'	7.1	2.9
35	07/16/75	05h54m53.0s	19°27.9'	155°24.6'	8.1	1.4
36	07/16/75	09h05m25.4s	19°20.2'	155°12.5'	5.0	1.3
37	07/16/75	17h35m09.1s	19°18.0'	155°13.0'	7.7	2.6
38	07/16/75	18h47m23.3s	19°26.6'	155°20.1'	5.3	1.6
39	07/16/75	19h25m01.4s	19°14.3'	155°31.0'	5.9	1.9
40	07/17/75	03h50m02.2s	19°25.1'	155°23.5'	7.3	2.5
41	07/17/75	05h13m30.4s	19°27.1'	155°28.4'	9.7	1.9
42	07/17/75	10h20m53.6s	19°23.6'	155°24.2'	7.5	1.6
43	07/17/75	12h57m57.2s	19°17.8'	155°13.0'	8.0	2.7
44	07/18/75	05h05m24.0s	19°29.5'	155°29.0'	6.7	2.2
45	07/18/75	21h08m02.7s	19°25.2'	155°21.8'	6.4	1.6
46	07/19/75	06h55m51.2s	19°31.2'	155°27.5'	7.2	2.9
47	07/21/75	11h12m41.6s	19°21.0'	155°10.0'	5.4	1.5
48	07/21/75	11h47m39.4s	19°25.8'	155°24.8'	8.6	1.4
49	07/22/75	10h01m27.7s	19°21.6'	155°30.2'	8.8	1.4
50	07/22/75	13h29m58.3s	19°20.6'	155°09.4'	6.0	1.4
51	07/22/75	15h44m25.6s	19°24.0'	155°25.2'	7.7	1.7
52	07/22/75	20h57m04.1s	19°24.7'	155°24.3'	7.2	1.7
53	07/23/75	00h38m38.1s	19°25.6'	155°22.0'	7.2	2.2
54	07/23/75	07h59m49.5s	19°27.2'	155°26.2'	7.9	1.6
55	07/23/75	08h44m17.7s	19°27.0'	155°26.6'	6.5	1.5
56	07/24/75	05h51m51.5s	19°18.0'	155°12.1'	27.8	1.9
57	07/25/75	02h18m10.9s	19°22.0'	155°18.1'	2.2	0.2
58	07/26/75	19h18m38.8s	19°19.3'	155°12.9'	7.5	2.0
59	07/27/75	05h19m41.7s	19°18.8'	155°23.4'	29.2	2.3
60	07/27/75	05h56m20.3s	19°25.3'	155°22.2'	7.1	2.7

Table 4. (continued)

Event	Date	Origin Time, UT	North Latitude	West Longitude	Depth, km	Magnitude
61	07/27/75	20h48m27.3s	19°20.5'	155°12.0'	7.0	1.9
62	07/28/75	05h36m17.7s	19°27.0'	155°28.8'	8.4	2.5
63	07/28/75	21h59m08.9s	19°20.9'	155°19.6'	26.1	2.3
64	07/29/75	01h07m49.0s	19°24.3'	155°16.2'	2.6	1.0
65	07/29/75	02h03m02.0s	19°19.6'	155°13.1'	6.9	1.5
66	07/29/75	04h57m56.9s	19°24.3'	155°24.6'	7.3	1.9
67	07/29/75	05h13m17.6s	19°24.4'	155°16.4'	2.1	0.4
68	07/29/75	08h10m11.0s	19°19.8'	155°13.9'	6.6	1.4
69	07/29/75	12h00m55.4s	19°16.6'	155°24.1'	3.9	1.9
70	07/29/75	13h49m31.2s	19°24.1'	155°16.1'	2.2	1.2
71	07/29/75	20h40m49.1s	19°26.3'	155°27.9'	8.0	1.7
72	07/29/75	22h20m16.4s	19°26.3'	155°15.5'	21.7	2.3
73	07/30/75	13h20m51.7s	19°23.5'	155°17.2'	13.3	2.3
74	07/30/75	22h46m27.7s	19°23.6'	155°17.2'	13.4	2.3
75	07/31/75	00h42m29.4s	19°19.4'	155°13.8'	7.5	1.5
76	07/31/75	01h24m33.0s	19°24.3'	155°16.6'	2.9	1.0
77	07/31/75	17h55m08.7s	19°17.8'	155°20.9'	7.5	2.1
78	08/01/75	02h17m01.8s	19°19.0'	155°13.9'	6.0	1.6
79	08/01/75	09h26m37.2s	19°22.0'	155°18.3'	2.0	0.5
80	08/01/75	21h52m37.9s	19°25.2'	155°17.8'	13.1	1.5
81	08/02/75	15h33m28.9s	19°16.1'	155°29.6'	6.9	2.5
82	08/03/75	06h09m34.5s	19°25.5'	155°22.5'	6.9	2.4
83	08/05/75	08h05m37.9s	19°17.1'	155°24.3'	3.0	2.1
84	08/05/75	13h49m56.1s	19°20.4'	155°13.8'	7.3	2.0
85	08/05/75	17h38m13.5s	19°16.1'	155°22.3'	7.1	2.5
86	08/05/75	17h50m47.0s	19°16.4'	155°22.5'	7.3	2.5
87	08/06/75	01h03m25.3s	19°16.3'	155°23.4'	4.2	1.6
88	08/06/75	01h32m53.0s	19°16.5'	155°23.1'	4.0	1.9
89	08/06/75	05h18m32.6s	19°16.4'	155°23.3'	5.1	1.6
90	08/06/75	06h54m42.9s	19°20.5'	155°10.4'	6.5	1.6
91	08/06/75	11h16m40.7s	19°17.9'	155°15.0'	7.1	1.7

Table 4. (continued)

Event	Date	Origin Time, UT	North Latitude	West Longitude	Depth, km	Magnitude
92	08/06/75	15h05m59.6s	19°16.5'	155°23.1'	6.0	1.6
93	08/06/75	15h49m12.9s	19°19.5'	155°13.8'	7.1	1.1
94	08/06/75	20h26m42.5s	19°19.0'	155°15.6'	6.8	1.6
95	08/07/75	09h29m24.7s	19°16.4'	155°22.7'	7.1	2.5
96	08/07/75	09h42m51.2s	19°19.3'	155°15.3'	7.1	1.6
97	08/07/75	10h32m21.6s	19°19.4'	155°17.7'	26.5	1.8
98	08/10/75	05h42m06.1s	19°19.4'	155°15.1'	8.6	1.4
99	08/10/75	07h43m42.7s	19°16.4'	155°23.1'	7.2	2.4
100	08/10/75	14h55m52.1s	19°26.3'	155°23.9'	9.5	1.1
101	08/10/75	20h14m32.7s	19°20.2'	155°12.4'	7.7	1.6
102	08/10/75	21h02m09.7s	19°19.0'	155°17.9'	10.7	1.4
103	08/11/75	02h15m14.8s	19°26.7'	155°29.4'	8.4	1.8
104	08/11/75	05h59m10.1s	19°21.3'	155°08.1'	6.8	2.0
105	08/11/75	09h42m34.5s	19°25.7'	155°28.4'	8.6	2.4
106	08/11/75	13h08m41.8s	19°20.3'	155°10.3'	6.9	1.7
107	08/11/75	21h40m39.1s	19°19.8'	155°12.2'	6.8	2.6
108	08/12/75	00h02m32.4s	19°23.9'	155°17.4'	2.1	1.1
109	08/12/75	04h25m47.4s	19°27.5'	155°30.4'	7.5	2.1
110	08/12/75	17h10m19.2s	19°23.6'	155°17.0'	3.1	1.1
111	08/12/75	19h23m41.2s	19°24.1'	155°24.4'	7.5	2.8

---

* Event parameters determined by U.S.G.S.

TABLE 5. Events Recorded at Oishiyama (34°05'56"N, 130°19'00"E)

Event	Date	Travel Time, s	Latitudinal Distance, km	Longitudinal Distance, km	Depth, km	Magnitude
1	07/10/70	4.4	6.52	9.46	5.74	2.5
2	07/12/70	3.2	-2.14	25.68	7.00	3.1
3	07/14/70	3.9	21.68	13.63	4.23	3.6
4	07/16/70	2.8	-2.22	28.24	1.38	2.1
5	07/17/70	2.9	23.50	21.73	3.19	3.6
6	07/19/70	3.0	21.19	20.48	6.76	2.1
7	07/20/70	2.4	8.86	18.56	1.83	2.3
8	07/20/70	2.0	3.92	23.82	1.85	2.3
9	07/22/70	4.5	19.01	9.51	4.91	2.4
10	07/25/70	3.7	16.82	12.74	4.95	2.1
11	07/25/70	3.2	13.47	15.58	6.79	2.4
12	07/27/70	3.7	9.66	12.30	5.75	2.9
13	07/29/70	3.4	18.88	15.32	4.31	2.0
14	07/29/70	2.8	7.55	17.74	5.32	2.7
15	07/30/70	3.8	13.55	11.52	4.91	2.5
16	07/31/70	4.1	20.65	12.39	5.01	2.3
17	07/31/70	4.0	21.60	13.54	5.13	2.2
18	07/31/70	2.8	24.31	26.45	5.47	3.1
19	08/01/70	2.9	15.47	16.12	0.53	1.9
20	08/03/70	4.6	7.38	8.85	7.50	3.1
21	08/04/70	3.9	21.64	14.29	5.77	1.8
22	08/04/70	3.1	-1.60	24.93	5.72	3.3
23	08/05/70	3.3	24.86	21.20	4.91	2.1
24	08/06/70	4.0	5.98	12.10	6.94	2.1
25	08/08/70	3.5	13.39	12.77	3.36	2.2
26	08/09/70	4.1	21.11	12.55	4.67	1.9
27	08/10/70	2.3	9.51	19.37	3.19	2.0
28	08/11/70	5.0	-2.01	10.94	8.19	2.9
29	08/12/70	3.6	5.81	13.34	4.03	2.0
30	08/12/70	3.2	23.94	21.00	4.97	2.1

Table 5. (continued)

Event	Date	Travel Time, s	Latitudinal Distance, km	Longitudinal Distance, km	Depth, km	Magnitude
31	08/14/70	4.2	4.05	10.86	4.60	2.2
32	08/15/70	3.6	12.74	12.71	5.66	3.1
33	04/01/71	2.1	14.35	19.76	0.50	3.0
34	04/02/71	2.2	14.28	19.73	2.16	3.0
35	06/01/71	2.2	14.34	19.70	3.01	2.0
36	06/19/71	2.5	18.33	19.91	2.42	2.6
37	06/19/71	4.1	20.75	11.82	4.18	3.0
38		3.6	26.61	21.48	5.81	3.3
39	08/26/71	2.2	1.84	26.72	2.67	4.3
40	10/16/71	3.9	23.99	15.10	3.41	2.6
41	10/19/71	3.9	13.73	11.18	5.53	3.8
42	11/24/71	3.4	23.33	18.18	3.50	3.6
43	11/26/71	4.1	27.07	17.06	5.35	3.6
44	12/03/71	2.0	4.34	23.82	2.58	4.1

Event positions are referred to 34°N latitude and 135°E longitude.
Distances north and east are positive.

TABLE 6. Events Recorded at Tsukuba (36°12'39"N, 140°06'35"E)

Event	Date	Origin Time*	North Latitude	East Longitude	Depth, km	Magnitude
1	12/24/69	04h45m05.3s	36°23'	140°01'	70	
2	12/25/69	03h10m31.8s	36°36'	140°31'	60	3.6
3	01/29/70	15h03m20.3s	35°53'	140°35'	60	5.1
4	02/04/70	02h14m13.8s	36°28'	140°38'	50	3.8
5	02/04/70	19h17m45.8s	36°26'	140°47'	40	4.8
6	02/17/70	15h24m08.0s	36°12'	139°18'	80	
7	03/03/70	21h17m32.9s	36°15'	140°03'	50	3.2
8	03/07/70	07h31m51.7s	36°11'	140°00'	90	
9	03/09/70	19h04m55.9s	36°35'	140°33'	50	3.8
10	03/15/70	17h18m32.6s	36°02'	140°18'	40	4.6
11	03/18/70	01h47m41.6s	35°44'	140°17'	80	
12	04/28/70	22h07m57.0s	35°54'	139°37'	20	3.5
13	05/04/70	06h15m17.6s	36°23'	140°06'	70	
14	06/10/70	22h54m22.3s	36°06'	139°49'	50	4.2
15	06/16/70	02h40m41.7s	36°10'	139°56'	50	
16	07/10/70	06h04m29.1s	36°05'	140°07'	80	
17	07/11/70	23h28m15.1s	36°30'	140°35'	50	5.1
18	07/14/70	03h11m27.0s	36°12'	139°51'	60	4.0
19	07/20/70	21h05m40.0s	36°10'	140°18'	60	
20	07/21/70	08h55m51.6s	36°01'	140°01'	70	
21	07/26/70	03h00m20.0s	35°59'	140°13'	40	3.4
22	08/02/70	15h44m24.4s	36°11'	139°21'	80	
23	08/04/70	10h30m11.9s	35°59'	140°33'	50	3.3
24	08/27/70	20h53m16.2s	36°08'	139°56'	60	3.9
25	09/09/70	03h22m56.2s	36°13'	139°41'	80	
26	09/09/70	07h11m13.3s	36°19'	140°31'	50	
27	09/12/70	11h23m47.8s	36°24'	140°24'	60	3.0
28	09/18/70	15h01m59.2s	36°06'	140°08'	70	
29	09/30/70	03h43m35.6s	36°02'	139°55'	40	3.3
30	09/30/70	04h26m24.3s	35°29'	139°38'	40	4.8
31	06/21/71	07h57m10.9s	36°11'	139°48'	60	4.9
32	06/29/71	16h57m				2.7

Table 6. (continued)

Event	Date	Origin Time*	North Latitude	East Longitude	Depth, km	Magnitude
33	07/02/71	02h04m			59	3.5
34	07/03/71	01h51m			48	2.6
35	07/11/71	21h37m17.0s			48	4.1
36	07/27/71	08h08m39.5s	35°56'	140°08'	80	5.5
37	08/04/71	00h32m43.7s	36°21'	140°07'	70	4.9
38	08/05/71	16h05m			50	3.0
39	08/10/71	10h34m34.7s	36°15'	139°47'	60	3.8
40	08/12/71	04h02m06.0s	35°45'	140°05'	76	4.9
41	08/12/71	12h02m			75	2.8
42	08/13/71	16h01m			57	3.2
43	08/15/71	15h46m			49	3.2

* Origin times are referred to Japanese Standard Time.

TABLE 7. Values of the Parameter a in (3.8) Derived from the Least Square Computation

Region	Events*	f = 1.50	f = 3.00	f = 6.00	f = 12.00	f = 24.00
Stone Canyon	1 - 36	0.94(±0.06)	1.01(±0.04)	0.83(±0.04)	0.12(±0.10)	-0.02(±0.06)
	37 - 86	1.13(±0.08)	1.47(±0.08)	1.53(±0.09)	0.41(±0.09)	0.45(±0.11)
	87 - 136	1.46(±0.13)	1.02(±0.12)	1.30(±0.08)	0.51(±0.09)	0.23(±0.09)
	137 - 185	1.81(±0.11)	1.44(±0.08)	1.05(±0.07)	0.22(±0.18)	-0.10(±0.13)
	1 - 47	1.02(±0.06)	1.08(±0.04)	1.05(±0.05)	0.21(±0.10)	0.14(±0.10)
	48 - 93	1.23(±0.08)	1.65(±0.10)	1.38(±0.09)	0.33(±0.10)	0.32(±0.10)
	94 - 139	0.80(±0.18)	1.17(±0.11)	1.40(±0.09)	0.62(±0.10)	0.11(±0.09)
	140 - 185	1.81(±0.11)	1.44(±0.08)	1.03(±0.07)	0.28(±0.20)	0.07(±0.14)
Bickmore Canyon^{+}	1 - 18	0.96(±0.09)	1.45(±0.07)	1.24(±0.07)	--	--
San Fernando	1 - 27	0.91(±0.07)	1.26(±0.06)	1.22(±0.07)	0.59(±0.11)	1.08(±0.09)
Kilauea	1 - 37	0.60(±0.06)	0.58(±0.04)	1.61(±0.05)	3.14(±0.07)	2.56(±0.26)
	38 - 74	0.54(±0.08)	0.63(±0.05)	1.56(±0.06)	3.09(±0.08)	2.36(±0.23)
	75 - 111	-0.15(±0.08)	0.61(±0.06)	0.99(±0.07)	2.52(±0.09)	1.80(±0.22)
Oishiyama	1 - 44	2.46(±0.09)	2.11(±0.09)	1.52(±0.08)	1.13(±0.08)	--
Tsukuba^{++}	1 - 43	0.99(±0.11)	1.11(±0.12)	1.69(±0.20)	2.23(±0.12)	1.74(±0.15)

f is frequency in Hz.

* Numbers refer to events listed in Tables 1 to 6.

$^{+}$ Values of the parameter a for Bickmore Canyon at 0.75 and 13.5 Hz are 3.02 (± 0.43) and 0.50(± 0.09), respectively.

$^{++}$Value of the parameter a for Tsukuba at 0.75 Hz is 0.69(± 0.11)

TABLE 8a. VALUES OF THE PARAMETER b IN (3.8) DERIVED FROM THE LEAST SQUARES COMPUTATION WITH THE FACTOR a IN (3.8) SET FREE

Region	Events*	f = 1.50	f = 3.00	f = 6.00	f = 12.00	f = 24.00
Stone Canyon	1 - 36	$1.54 \times 10^{-2} (\pm 0.07 \times 10^{-2})$	$1.82 \times 10^{-2} (\pm 0.06 \times 10^{-2})$	$2.09 \times 10^{-2} (\pm 0.07 \times 10^{-2})$	$3.82 \times 10^{-2} (\pm 0.22 \times 10^{-2})$	$4.23 \times 10^{-2} (\pm 0.16 \times 10^{-2})$
	37 - 86	$2.03 \times 10^{-2} (\pm 0.10 \times 10^{-2})$	$1.99 \times 10^{-2} (\pm 0.12 \times 10^{-2})$	$1.77 \times 10^{-2} (\pm 0.14 \times 10^{-2})$	$3.74 \times 10^{-2} (\pm 0.16 \times 10^{-2})$	$3.83 \times 10^{-2} (\pm 0.22 \times 10^{-2})$
	87 - 136	$1.76 \times 10^{-2} (\pm 0.16 \times 10^{-2})$	$3.08 \times 10^{-2} (\pm 0.20 \times 10^{-2})$	$2.12 \times 10^{-2} (\pm 0.13 \times 10^{-2})$	$3.71 \times 10^{-2} (\pm 0.16 \times 10^{-2})$	$4.34 \times 10^{-2} (\pm 0.17 \times 10^{-2})$
	137 - 185	$1.40 \times 10^{-2} (\pm 0.10 \times 10^{-2})$	$2.01 \times 10^{-2} (\pm 0.09 \times 10^{-2})$	$2.23 \times 10^{-2} (\pm 0.09 \times 10^{-2})$	$4.64 \times 10^{-2} (\pm 0.31 \times 10^{-2})$	$5.13 \times 10^{-2} (\pm 0.24 \times 10^{-2})$
	1 - 47	$1.49 \times 10^{-2} (\pm 0.07 \times 10^{-2})$	$1.77 \times 10^{-2} (\pm 0.06 \times 10^{-2})$	$1.84 \times 10^{-2} (\pm 0.09 \times 10^{-2})$	$3.84 \times 10^{-2} (\pm 0.24 \times 10^{-2})$	$4.07 \times 10^{-2} (\pm 0.25 \times 10^{-2})$
	48 - 93	$1.84 \times 10^{-2} (\pm 0.09 \times 10^{-2})$	$1.88 \times 10^{-2} (\pm 0.15 \times 10^{-2})$	$2.08 \times 10^{-2} (\pm 0.14 \times 10^{-2})$	$3.94 \times 10^{-2} (\pm 0.17 \times 10^{-2})$	$4.01 \times 10^{-2} (\pm 0.19 \times 10^{-2})$
	94 - 139	$2.87 \times 10^{-2} (\pm 0.23 \times 10^{-2})$	$2.69 \times 10^{-2} (\pm 0.19 \times 10^{-2})$	$1.85 \times 10^{-2} (\pm 0.14 \times 10^{-2})$	$3.47 \times 10^{-2} (\pm 0.17 \times 10^{-2})$	$4.57 \times 10^{-2} (\pm 0.19 \times 10^{-2})$
	140 - 185	$1.40 \times 10^{-2} (\pm 0.10 \times 10^{-2})$	$2.02 \times 10^{-2} (\pm 0.09 \times 10^{-2})$	$2.26 \times 10^{-2} (\pm 0.09 \times 10^{-2})$	$4.56 \times 10^{-2} (\pm 0.33 \times 10^{-2})$	$4.88 \times 10^{-2} (\pm 0.25 \times 10^{-2})$
Bickmore Canyon+	1 - 18	$1.64 \times 10^{-2} (\pm 0.08 \times 10^{-2})$	$1.54 \times 10^{-2} (\pm 0.07 \times 10^{-2})$	$2.10 \times 10^{-2} (\pm 0.10 \times 10^{-2})$	-------	-------
San Fernando	1 - 27	$2.76 \times 10^{-2} (\pm 0.14 \times 10^{-2})$	$2.54 \times 10^{-2} (\pm 0.14 \times 10^{-2})$	$3.32 \times 10^{-2} (\pm 0.16 \times 10^{-2})$	$5.61 \times 10^{-2} (\pm 0.29 \times 10^{-2})$	$5.40 \times 10^{-2} (\pm 0.26 \times 10^{-2})$
Kilauea	1 - 37	$1.15 \times 10^{-2} (\pm 0.05 \times 10^{-2})$	$1.97 \times 10^{-2} (\pm 0.05 \times 10^{-2})$	$2.09 \times 10^{-2} (\pm 0.09 \times 10^{-2})$	$-0.64 \times 10^{-2} (\pm 0.13 \times 10^{-2})$	$2.43 \times 10^{-2} (\pm 0.73 \times 10^{-2})$
	38 - 74	$1.04 \times 10^{-2} (\pm 0.06 \times 10^{-2})$	$1.79 \times 10^{-2} (\pm 0.06 \times 10^{-2})$	$1.94 \times 10^{-2} (\pm 0.10 \times 10^{-2})$	$-0.81 \times 10^{-2} (\pm 0.15 \times 10^{-2})$	$3.23 \times 10^{-2} (\pm 0.71 \times 10^{-2})$
	75 - 111	$1.73 \times 10^{-2} (\pm 0.07 \times 10^{-2})$	$1.65 \times 10^{-2} (\pm 0.06 \times 10^{-2})$	$2.82 \times 10^{-2} (\pm 0.12 \times 10^{-2})$	$0.03 \times 10^{-2} (\pm 0.19 \times 10^{-2})$	$4.79 \times 10^{-2} (\pm 0.80 \times 10^{-2})$
Oishiyama	1 - 44	$0.21 \times 10^{-2} (\pm 0.09 \times 10^{-2})$	$0.88 \times 10^{-2} (\pm 0.11 \times 10^{-2})$	$2.31 \times 10^{-2} (\pm 0.12 \times 10^{-2})$	$3.33 \times 10^{-2} (\pm 0.14 \times 10^{-2})$	-------
Tsukuba++	1 - 43	$0.72 \times 10^{-2} (\pm 0.05 \times 10^{-2})$	$0.99 \times 10^{-2} (\pm 0.07 \times 10^{-2})$	$1.11 \times 10^{-2} (\pm 0.12 \times 10^{-2})$	$0.86 \times 10^{-2} (\pm 0.08 \times 10^{-2})$	$1.52 \times 10^{-2} (\pm 0.12 \times 10^{-2})$

f is frequency in Hz.

* Numbers refer to events in Tables 1 to 6.

\+ Values of the parameter b for Bickmore Cayon at 0.75 and 13.5 Hz are $0.32 \times 10^{-2} (\pm 0.28 \times 10^{-2})$ and $3.35 \times 10^{-2} (\pm 0.16 \times 10^{-2})$, respectively.

++Value of the parameter b for Tsukuba at 0.75 Hz is $0.48 \times 10^{-2} (\pm 0.04 \times 10^{-2})$.

TABLE 8b. VALUES OF THE PARAMETER b IN (3.8) DERIVED FROM THE LEAST SQUARES COMPUTATION WITH THE FACTOR a IN (3.8) FIXED TO 1

Region	Events*	f = 1.50	f = 3.00	f = 6.00	f = 12.00	f = 24.00
Stone Canyon	1 - 36	$1.48 \times 10^{-2} (\pm 0.03 \times 10^{-2})$	$1.83 \times 10^{-2} (\pm 0.03 \times 10^{-2})$	$1.83 \times 10^{-2} (\pm 0.03 \times 10^{-2})$	$1.82 \times 10^{-2} (\pm 0.07 \times 10^{-2})$	$1.73 \times 10^{-2} (\pm 0.06 \times 10^{-2})$
	37 - 86	$2.17 \times 10^{-2} (\pm 0.03 \times 10^{-2})$	$2.65 \times 10^{-2} (\pm 0.04 \times 10^{-2})$	$2.58 \times 10^{-2} (\pm 0.05 \times 10^{-2})$	$2.73 \times 10^{-2} (\pm 0.05 \times 10^{-2})$	$2.74 \times 10^{-2} (\pm 0.06 \times 10^{-2})$
	87 - 136	$2.27 \times 10^{-2} (\pm 0.05 \times 10^{-2})$	$3.11 \times 10^{-2} (\pm 0.06 \times 10^{-2})$	$2.55 \times 10^{-2} (\pm 0.05 \times 10^{-2})$	$2.92 \times 10^{-2} (\pm 0.05 \times 10^{-2})$	$2.88 \times 10^{-2} (\pm 0.06 \times 10^{-2})$
	137 - 185	$2.12 \times 10^{-2} (\pm 0.03 \times 10^{-2})$	$2.47 \times 10^{-2} (\pm 0.03 \times 10^{-2})$	$2.29 \times 10^{-2} (\pm 0.03 \times 10^{-2})$	$3.36 \times 10^{-2} (\pm 0.08 \times 10^{-2})$	$3.18 \times 10^{-2} (\pm 0.07 \times 10^{-2})$
	1 - 47	$1.51 \times 10^{-2} (\pm 0.03 \times 10^{-2})$	$1.87 \times 10^{-2} (\pm 0.03 \times 10^{-2})$	$1.91 \times 10^{-2} (\pm 0.04 \times 10^{-2})$	$2.03 \times 10^{-2} (\pm 0.06 \times 10^{-2})$	$1.94 \times 10^{-2} (\pm 0.08 \times 10^{-2})$
	48 - 93	$2.08 \times 10^{-2} (\pm 0.03 \times 10^{-2})$	$2.76 \times 10^{-2} (\pm 0.05 \times 10^{-2})$	$2.62 \times 10^{-2} (\pm 0.04 \times 10^{-2})$	$2.88 \times 10^{-2} (\pm 0.05 \times 10^{-2})$	$2.73 \times 10^{-2} (\pm 0.05 \times 10^{-2})$
	94 - 139	$2.62 \times 10^{-2} (\pm 0.06 \times 10^{-2})$	$2.96 \times 10^{-2} (\pm 0.06 \times 10^{-2})$	$2.46 \times 10^{-2} (\pm 0.05 \times 10^{-2})$	$2.83 \times 10^{-2} (\pm 0.05 \times 10^{-2})$	$2.85 \times 10^{-2} (\pm 0.06 \times 10^{-2})$
	140 - 185	$2.12 \times 10^{-2} (\pm 0.03 \times 10^{-2})$	$2.46 \times 10^{-2} (\pm 0.03 \times 10^{-2})$	$2.29 \times 10^{-2} (\pm 0.03 \times 10^{-2})$	$3.40 \times 10^{-2} (\pm 0.09 \times 10^{-2})$	$3.25 \times 10^{-2} (\pm 0.07 \times 10^{-2})$
Bickmore Canyon^{+}	1 - 18	$1.61 \times 10^{-2} (\pm 0.04 \times 10^{-2})$	$1.95 \times 10^{-2} (\pm 0.03 \times 10^{-2})$	$2.39 \times 10^{-2} (\pm 0.04 \times 10^{-2})$	-------	-------
San Fernando	1 - 27	$2.59 \times 10^{-2} (\pm 0.06 \times 10^{-2})$	$3.06 \times 10^{-2} (\pm 0.06 \times 10^{-2})$	$3.75 \times 10^{-2} (\pm 0.07 \times 10^{-2})$	$4.60 \times 10^{-2} (\pm 0.11 \times 10^{-2})$	$5.62 \times 10^{-2} (\pm 0.09 \times 10^{-2})$
Kilauea	1 - 37	$0.84 \times 10^{-2} (\pm 0.02 \times 10^{-2})$	$1.53 \times 10^{-2} (\pm 0.02 \times 10^{-2})$	$3.06 \times 10^{-2} (\pm 0.02 \times 10^{-2})$	$3.12 \times 10^{-2} (\pm 0.05 \times 10^{-2})$	$6.74 \times 10^{-2} (\pm 0.19 \times 10^{-2})$
	38 - 74	$0.71 \times 10^{-2} (\pm 0.02 \times 10^{-2})$	$1.39 \times 10^{-2} (\pm 0.02 \times 10^{-2})$	$2.87 \times 10^{-2} (\pm 0.03 \times 10^{-2})$	$3.12 \times 10^{-2} (\pm 0.05 \times 10^{-2})$	$7.30 \times 10^{-2} (\pm 0.21 \times 10^{-2})$
	75 - 111	$0.77 \times 10^{-2} (\pm 0.03 \times 10^{-2})$	$1.22 \times 10^{-2} (\pm 0.02 \times 10^{-2})$	$2.80 \times 10^{-2} (\pm 0.03 \times 10^{-2})$	$3.20 \times 10^{-2} (\pm 0.06 \times 10^{-2})$	$7.57 \times 10^{-2} (\pm 0.22 \times 10^{-2})$
Oishiyama	1 - 44	$1.53 \times 10^{-2} (\pm 0.05 \times 10^{-2})$	$2.23 \times 10^{-2} (\pm 0.05 \times 10^{-2})$	$3.07 \times 10^{-2} (\pm 0.04 \times 10^{-2})$	$3.55 \times 10^{-2} (\pm 0.05 \times 10^{-2})$	-------
Tsukuba^{++}	1 - 43	$0.72 \times 10^{-2} (\pm 0.02 \times 10^{-2})$	$1.05 \times 10^{-2} (\pm 0.02 \times 10^{-2})$	$1.50 \times 10^{-2} (\pm 0.05 \times 10^{-2})$	$1.57 \times 10^{-2} (\pm 0.03 \times 10^{-2})$	$2.03 \times 10^{-2} (\pm 0.04 \times 10^{-2})$

f is frequency in Hz.

* Numbers refer to events listed in Tables 1 to 6.

$^{+}$ Values of the parameter b for Bickmore Canyon at 0.75 and 13.5 Hz are $1.61 \times 10^{-2} (\pm 0.07 \times 10^{-2})$ and $2.48 \times 10^{-2} (\pm 0.06 \times 10^{-2})$, respectively.

$^{++}$Value of the parameter b for Tsukuba at 0.75 Hz is $0.38 \times 10^{-2} (\pm 0.02 \times 10^{-2})$

TABLE 8c. VALUES OF THE PARAMETER b IN (3.8) DERIVED FROM THE LEAST SQUARES COMPUTATION WITH THE FACTOR a IN (3.8) FIXED TO 0.5

Region	Events*	f = 1.50	f = 3.00	f = 6.00	f = 12.00	f = 24.00
Stone Canyon	1 - 36	$1.99 \times 10^{-2} (\pm 0.03 \times 10^{-2})$	$2.47 \times 10^{-2} (\pm 0.03 \times 10^{-2})$	$2.57 \times 10^{-2} (\pm 0.03 \times 10^{-2})$	$2.95 \times 10^{-2} (\pm 0.06 \times 10^{-2})$	$2.95 \times 10^{-2} (\pm 0.05 \times 10^{-2})$
	37 - 86	$2.72 \times 10^{-2} (\pm 0.03 \times 10^{-2})$	$3.35 \times 10^{-2} (\pm 0.05 \times 10^{-2})$	$3.34 \times 10^{-2} (\pm 0.05 \times 10^{-2})$	$3.59 \times 10^{-2} (\pm 0.05 \times 10^{-2})$	$3.74 \times 10^{-2} (\pm 0.06 \times 10^{-2})$
	87 - 136	$2.83 \times 10^{-2} (\pm 0.05 \times 10^{-2})$	$3.91 \times 10^{-2} (\pm 0.06 \times 10^{-2})$	$3.28 \times 10^{-2} (\pm 0.05 \times 10^{-2})$	$3.73 \times 10^{-2} (\pm 0.05 \times 10^{-2})$	$3.82 \times 10^{-2} (\pm 0.05 \times 10^{-2})$
	137 - 185	$2.56 \times 10^{-2} (\pm 0.03 \times 10^{-2})$	$2.97 \times 10^{-2} (\pm 0.03 \times 10^{-2})$	$2.87 \times 10^{-2} (\pm 0.03 \times 10^{-2})$	$4.18 \times 10^{-2} (\pm 0.08 \times 10^{-2})$	$4.06 \times 10^{-2} (\pm 0.06 \times 10^{-2})$
	1 - 47	$2.04 \times 10^{-2} (\pm 0.03 \times 10^{-2})$	$2.55 \times 10^{-2} (\pm 0.03 \times 10^{-2})$	$2.69 \times 10^{-2} (\pm 0.04 \times 10^{-2})$	$3.17 \times 10^{-2} (\pm 0.06 \times 10^{-2})$	$3.18 \times 10^{-2} (\pm 0.07 \times 10^{-2})$
	48 - 93	$2.60 \times 10^{-2} (\pm 0.03 \times 10^{-2})$	$3.44 \times 10^{-2} (\pm 0.05 \times 10^{-2})$	$3.33 \times 10^{-2} (\pm 0.05 \times 10^{-2})$	$3.67 \times 10^{-2} (\pm 0.05 \times 10^{-2})$	$3.67 \times 10^{-2} (\pm 0.05 \times 10^{-2})$
	94 - 139	$3.25 \times 10^{-2} (\pm 0.06 \times 10^{-2})$	$3.77 \times 10^{-2} (\pm 0.06 \times 10^{-2})$	$3.23 \times 10^{-2} (\pm 0.06 \times 10^{-2})$	$3.67 \times 10^{-2} (\pm 0.05 \times 10^{-2})$	$3.82 \times 10^{-2} (\pm 0.06 \times 10^{-2})$
	140 - 185	$2.56 \times 10^{-2} (\pm 0.03 \times 10^{-2})$	$2.97 \times 10^{-2} (\pm 0.03 \times 10^{-2})$	$2.87 \times 10^{-2} (\pm 0.03 \times 10^{-2})$	$4.20 \times 10^{-2} (\pm 0.08 \times 10^{-2})$	$4.13 \times 10^{-2} (\pm 0.06 \times 10^{-2})$
Bickmore Canyon+	1 - 18	$2.03 \times 10^{-2} (\pm 0.04 \times 10^{-2})$	$2.41 \times 10^{-2} (\pm 0.04 \times 10^{-2})$	$3.00 \times 10^{-2} (\pm 0.05 \times 10^{-2})$	-------	-------
San Fernando	1 - 27	$3.55 \times 10^{-2} (\pm 0.06 \times 10^{-2})$	$4.08 \times 10^{-2} (\pm 0.07 \times 10^{-2})$	$4.75 \times 10^{-2} (\pm 0.08 \times 10^{-2})$	$5.82 \times 10^{-2} (\pm 0.11 \times 10^{-2})$	$6.99 \times 10^{-2} (\pm 0.10 \times 10^{-2})$
Kilauea	1 - 37	$1.23 \times 10^{-2} (\pm 0.02 \times 10^{-2})$	$2.07 \times 10^{-2} (\pm 0.02 \times 10^{-2})$	$3.85 \times 10^{-2} (\pm 0.03 \times 10^{-2})$	$4.00 \times 10^{-2} (\pm 0.06 \times 10^{-2})$	$8.12 \times 10^{-2} (\pm 0.20 \times 10^{-2})$
	38 - 74	$1.07 \times 10^{-2} (\pm 0.02 \times 10^{-2})$	$1.93 \times 10^{-2} (\pm 0.02 \times 10^{-2})$	$3.70 \times 10^{-2} (\pm 0.03 \times 10^{-2})$	$4.06 \times 10^{-2} (\pm 0.06 \times 10^{-2})$	$8.78 \times 10^{-2} (\pm 0.22 \times 10^{-2})$
	75 - 111	$1.19 \times 10^{-2} (\pm 0.02 \times 10^{-2})$	$1.77 \times 10^{-2} (\pm 0.02 \times 10^{-2})$	$3.65 \times 10^{-2} (\pm 0.03 \times 10^{-2})$	$4.25 \times 10^{-2} (\pm 0.06 \times 10^{-2})$	$9.30 \times 10^{-2} (\pm 0.23 \times 10^{-2})$
Oishiyama	1 - 44	$1.98 \times 10^{-2} (\pm 0.06 \times 10^{-2})$	$2.84 \times 10^{-2} (\pm 0.06 \times 10^{-2})$	$3.79 \times 10^{-2} (\pm 0.05 \times 10^{-2})$	$4.37 \times 10^{-2} (\pm 0.05 \times 10^{-2})$	-------
Tsukuba++	1 - 43	$0.92 \times 10^{-2} (\pm 0.02 \times 10^{-2})$	$1.31 \times 10^{-2} (\pm 0.03 \times 10^{-2})$	$1.79 \times 10^{-2} (\pm 0.05 \times 10^{-2})$	$1.86 \times 10^{-2} (\pm 0.04 \times 10^{-2})$	$2.38 \times 10^{-2} (\pm 0.04 \times 10^{-2})$

f is frequency in Hz.

* Numbers refer to events listed in Tables 1 to 6.

\+ Values of the parameter b for Bickmore Canyon at 0.75 and 13.5 Hz are $1.93 \times 10^{-2} (\pm 0.07 \times 10^{-2})$ and $3.34 \times 10^{-2} (\pm 0.06 \times 10^{-2})$, respectively.

++Value of the parameter b for Tsukuba at 0.75 Hz is $0.54 \times 10^{-2} (\pm 0.02 \times 10^{-2})$.

CHAPTER 4

Regional Variation of the Scaling Law of Earthquake Source Spectrum

4.1 Introduction

The spectral content of earthquake motion changes systematically with the earthquake magnitude in a given seismic area. The manner in which the spectrum changes with magnitude is called the scaling law of seismic spectrum. A reliable scaling law gives us the basis for predicting strong motion of a large earthquake using the data from smaller earthquakes in the same seismic area. Since the number of earthquakes increases exponentially with the decreasing magnitude, the data collection for smaller earthquakes is much more efficiently done. Accurate determination of the scaling law for these smaller events is thus a promising way of estimating the strong motion for earthquakes in an area where past records of strong motion are unavailable.

The scaling law also plays an important role in the problem of discriminating earthquakes from underground explosions. The applicability of the M_s-m_b discriminant relies upon a feature of the scaling law of seismic spectrum: i.e., the relative excitation at two different frequencies 1 and 0.05 Hz, for earthquakes and explosions. For a reliable discriminant, it is important to know the scaling law for all the seismic areas concerned.

The scaling law is usually illustrated, as for example in Fig. 4.15, by the absolute value of the Fourier transform of the displacement due to body waves which would have been recorded if both the earthquake source and the seismograph were buried at a fixed, long distance in a uniform, unbounded elastic medium. The spectral curve is expected to be flat at low frequencies for fault slip with a step-like time function. The height of the flat part of the spectrum is proportional to the seismic moment, which represents the strength of the point source equivalent to an earthquake. In terms of the parameters of the dislocation model, the seismic moment is equal to the product of the amount of final slip integrated over the fault area and the rigidity of the elastic medium in which the slip occurred (Aki, 1966; Brune, 1970, 1971; Randall, 1973; Molnar et al., 1973). The seismic moment corresponding to each spectral curve in Fig. 4.15 is indicated in the vertical coordinate.

A very simple scaling law was proposed by Aki (1967) based on the assumption that large and small earthquakes are similar phenomena in a medium with given elastic constants and density. The assumption implies the same geometry, a constant stress drop, and constant rupture and slip velocities independent of fault length. In this model, all the earthquakes share the same spectral shape which decays inversely proportional to the square of frequency beyond a corner frequency. For this behavior, we shall call the scaling law the ω^2-law. From the similarity assumption, the corner frequency is inversely proportional to the fault length and the seismic moment is proportional to the cube of the fault length. Thus, the locus of the corner frequency predicted by Aki's model lies on a straight line with slope -3. The locus was determined to fit various observations such as the fault versus magnitude relations (Tocher, 1958, 1960), spectral ratios (Berkhemer, 1962), and relations between different magnitude scales (Gutenberg and Richter, 1956). Further testing of the ω^2-law was made recently by Aki (1972b) confirming its general validity for earthquakes with magnitudes (M_S) greater than 6 and for periods longer than 10 sec. The earthquakes under this scaling law show the stress-drop in the range of 10 to 100 bars (Aki, 1972a).

Accurate testing of the ω^2-law for periods shorter than 10 sec was difficult because the separation of the source effect from the effect of scattering and attenuation became increasingly difficult at frequencies above 1 Hz. In this Chapter, we shall overcome this difficulty by using the source factor of coda waves from local earthquakes.

4.2 Source factors of coda

Equation (3.8) provides us with the least square estimates $C(\omega)$ from which the source terms $c(\omega) = 10^{C(\omega)}$ are derived. Then using equation (3.7) we obtain the source factors of coda $(S(\omega))^{1/2}$ which are independent of filter bandwidths. These source factors are shown plotted against frequency in Figs. 4.1, 4.2a, 4.3a, and 4.4 through 4.6 for the various areas that we considered. Each line depicted represents an earthquake. The shorter lines define events for which one or more filter channels were not operating or for which the signal was too weak to be digitized accurately. These plots were obtained by using the single scattering model for body waves, that is by fixing the factor a in equation (3.6) to the value 1. This choice of a, however, is of no consequences for the present application because the relative magnitude of $(S(\omega))^{1/2}$ among earthquakes does not depend on the value of a. A value of a of 0.5, for example, merely shifts down the absolute level of the spectral curves shown in these figures.

Variations in the gross features of these plots are readily discernable. In California, as in Hawaii, the source factors tend to decay regularly with increasing frequency and, while the curves are parallel for the San Fernando area (Fig. 4.3a), it appears that the spread of curves is greater at low frequency and gets narrower for high frequencies at Bickmore Canyon (Fig. 4.2a) and Kilauea (Fig. 4.4). Although less conspicuous, this scale effect with earthquake magnitude is also present at 24 versus 1.5 Hz for a few large events at Stone Canyon (Fig. 4.1). On the other hand, in Japan, the source factors show a rather weak dependence on frequency. At Tsukuba, they appear somewhat richer

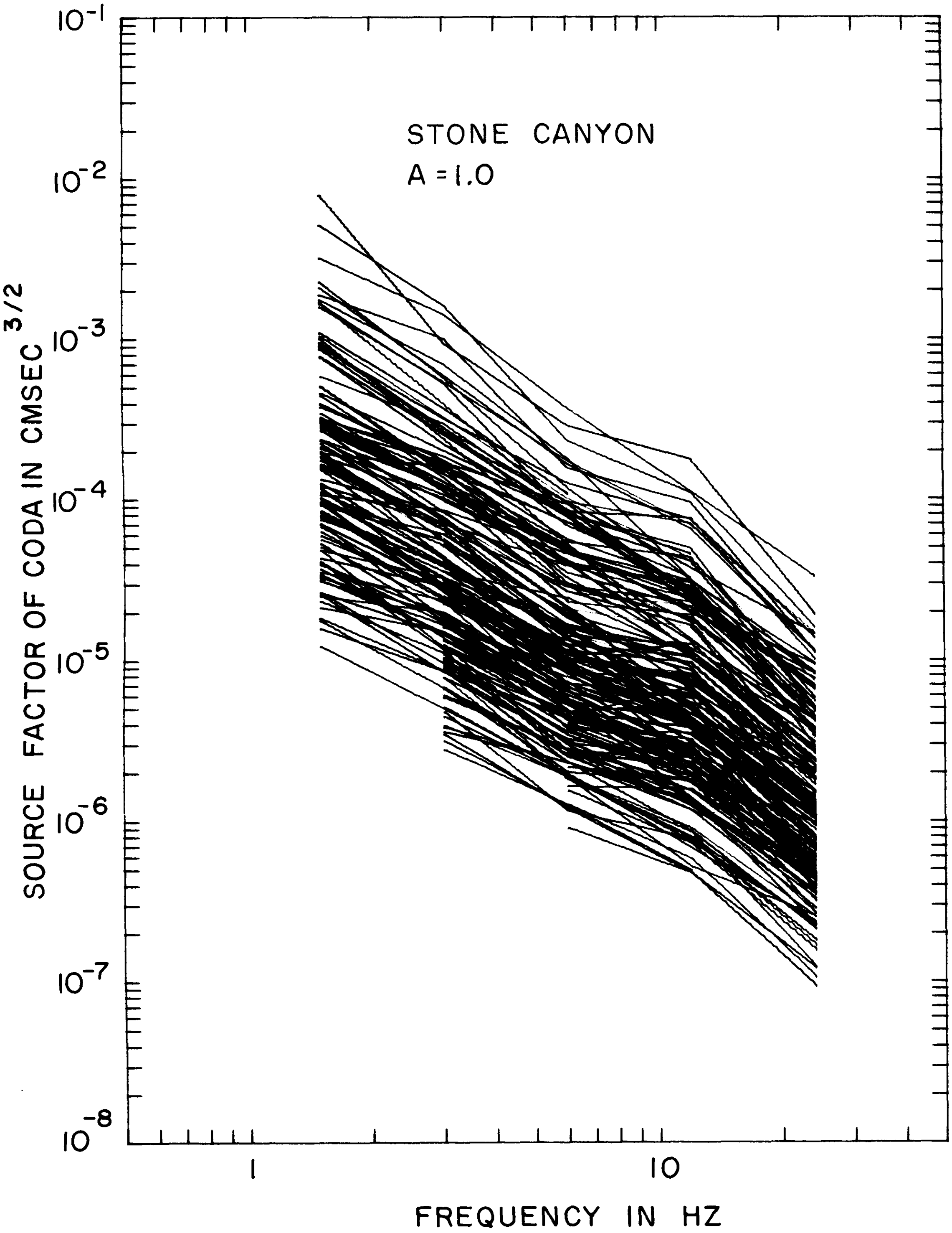

Fig. 4.1. Source factors of coda in the range of 1.5 to 24 Hz for the events recorded at Stone Canyon, central California.

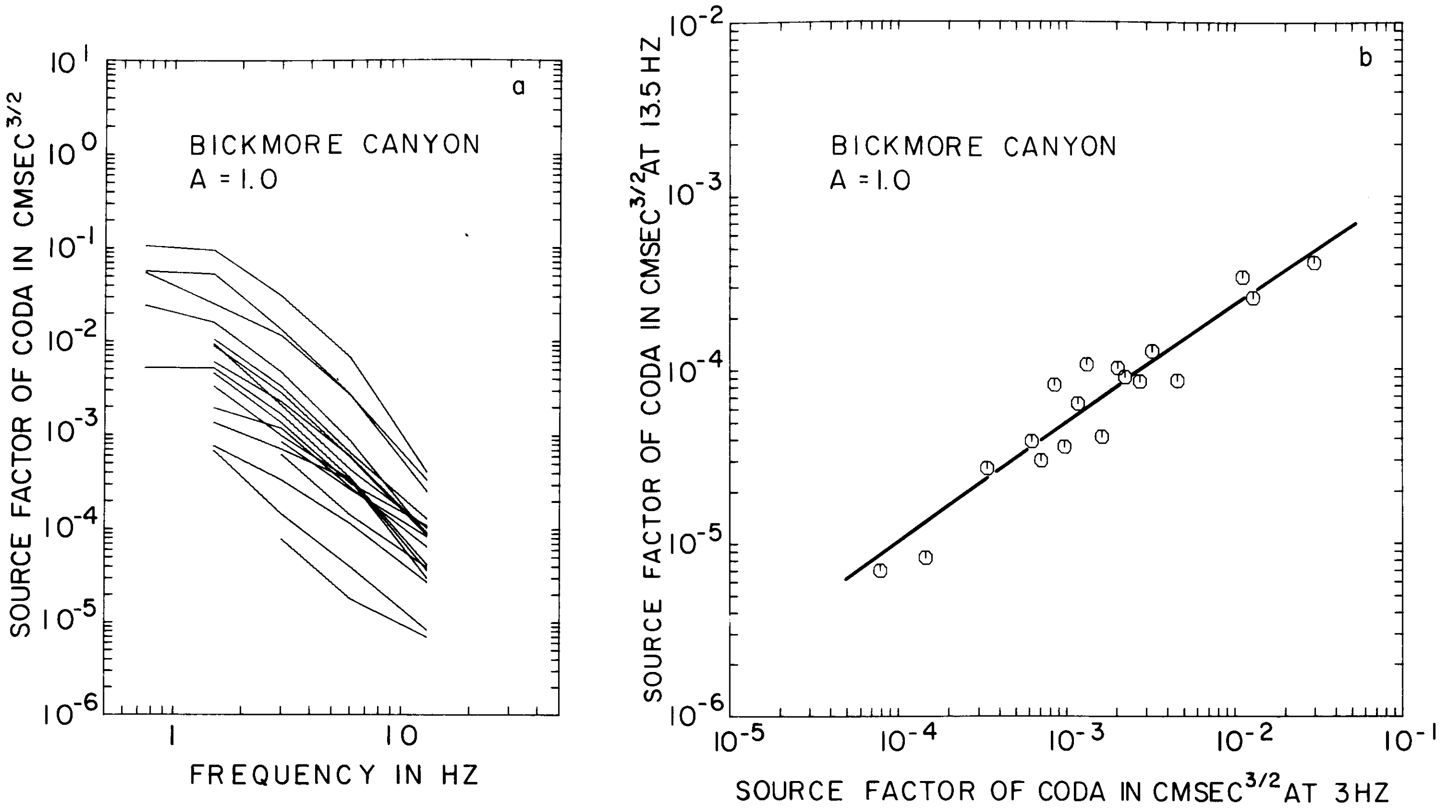

Fig. 4.2. (a) Source factors of coda in the range of 0.75 to 13.5 Hz for the events recorded at Bickmore Canyon, central California, and (b) relation between these coda source factors at 13.5 and 3 Hz. The rate of increase of the source factors is slower at 13.5 Hz than at 3 Hz, indicating a change in spectral shape with increasing magnitude in this frequency range.

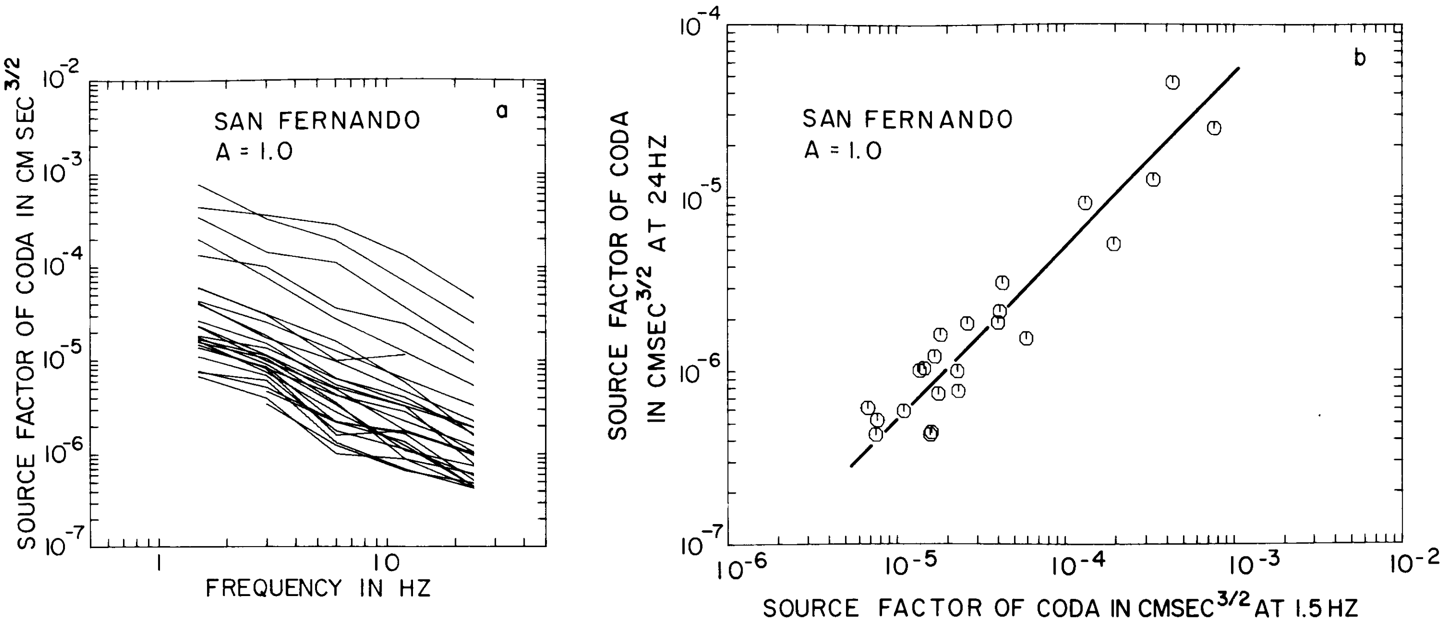

Fig. 4.3. (a) Source factors of coda in the range of 1.5 to 24 Hz for the events recorded at San Fernando, southern California, and (b) relation between these coda source factors at 24 and 1.5 Hz. The same rate of increase observed at 1.5 and 24 Hz implies that the spectral shape of earthquake source does not change with magnitude within this frequency range.

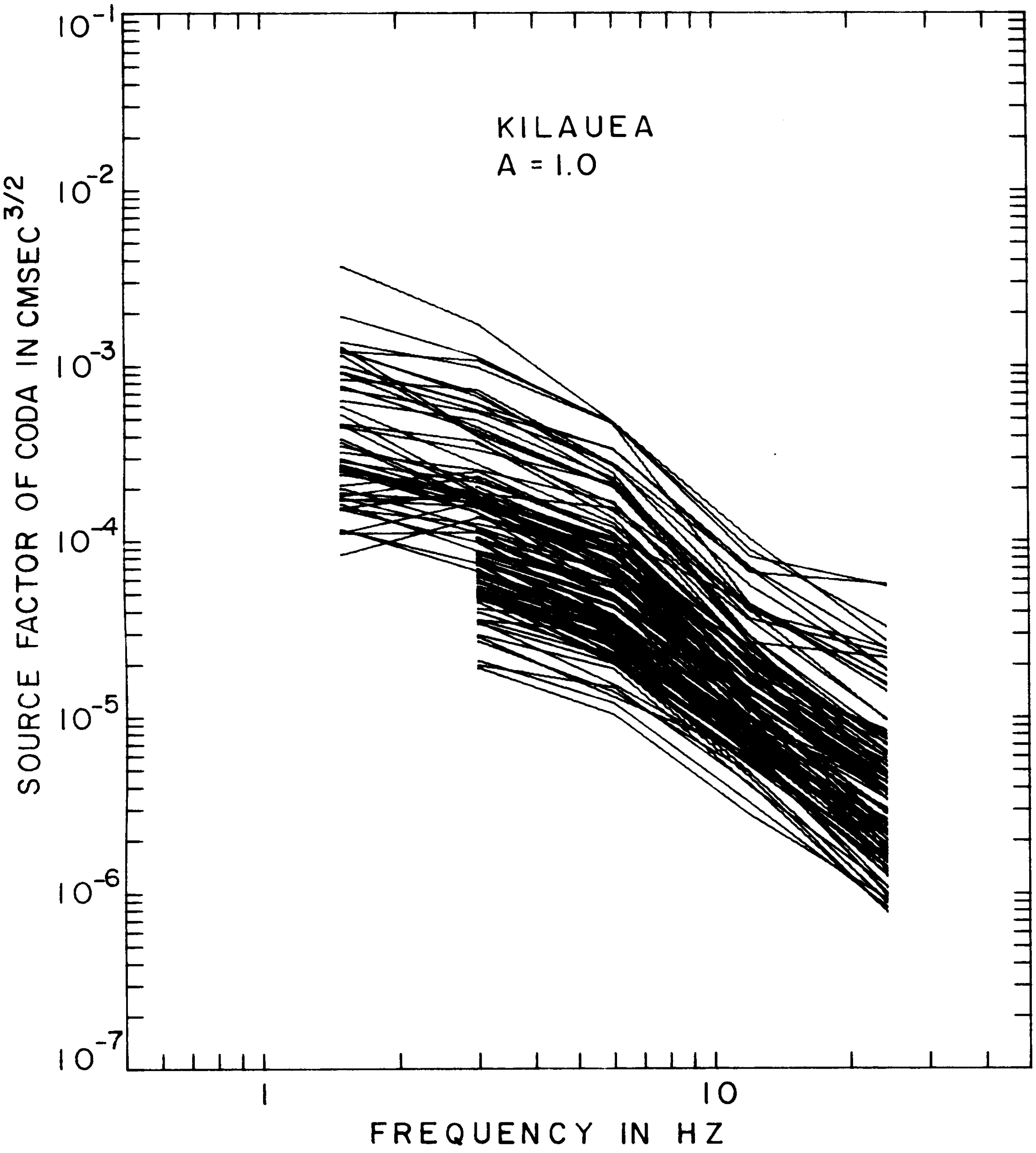

Fig. 4.4. Source factors of coda in the range of 1.5 to 24 Hz for the events recorded at Kilauea, Hawaii.

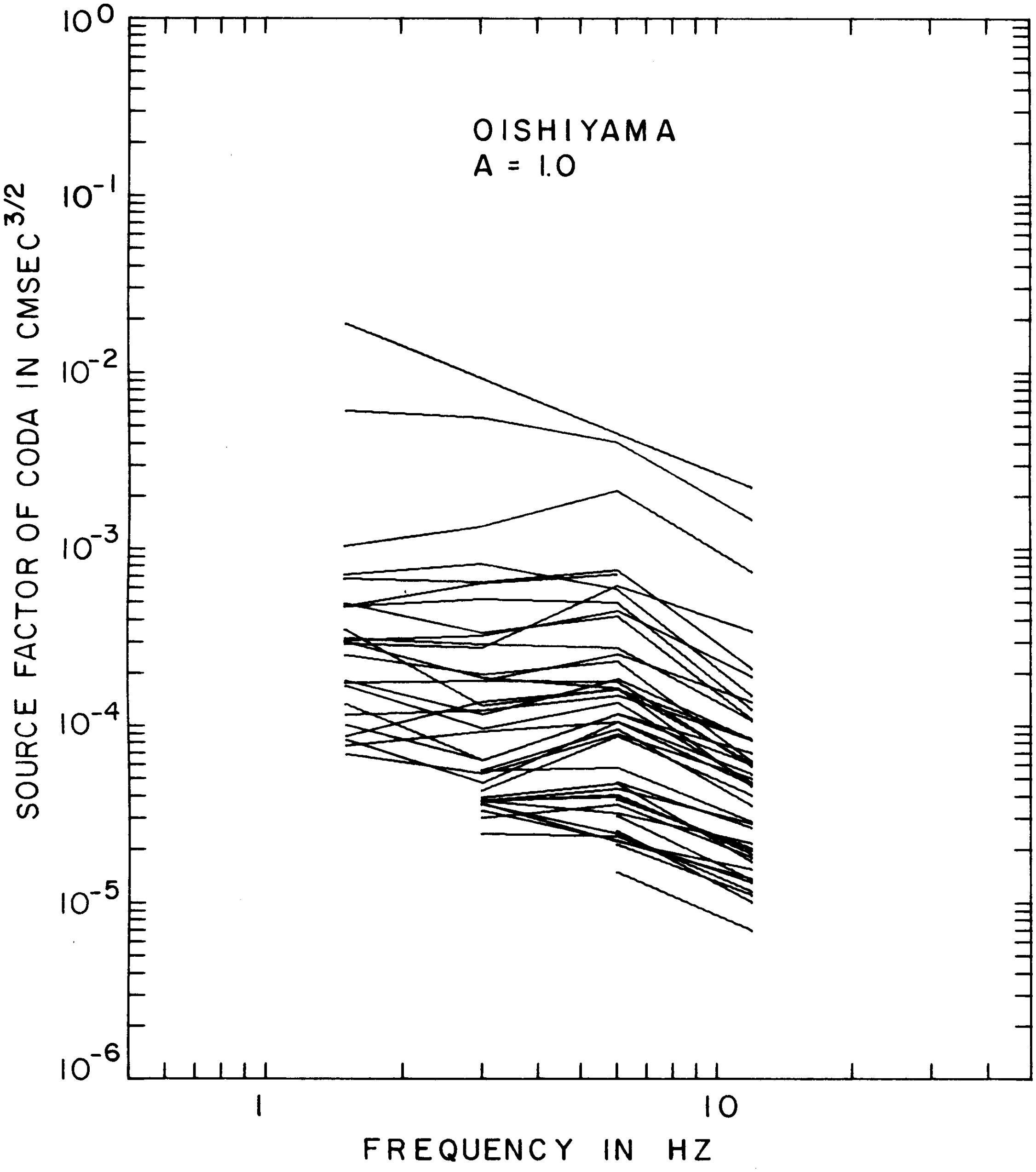

Fig. 4.5. Source factors of coda in the range of 1.5 to 12 Hz for the events recorded at Oishiyama, Japan.

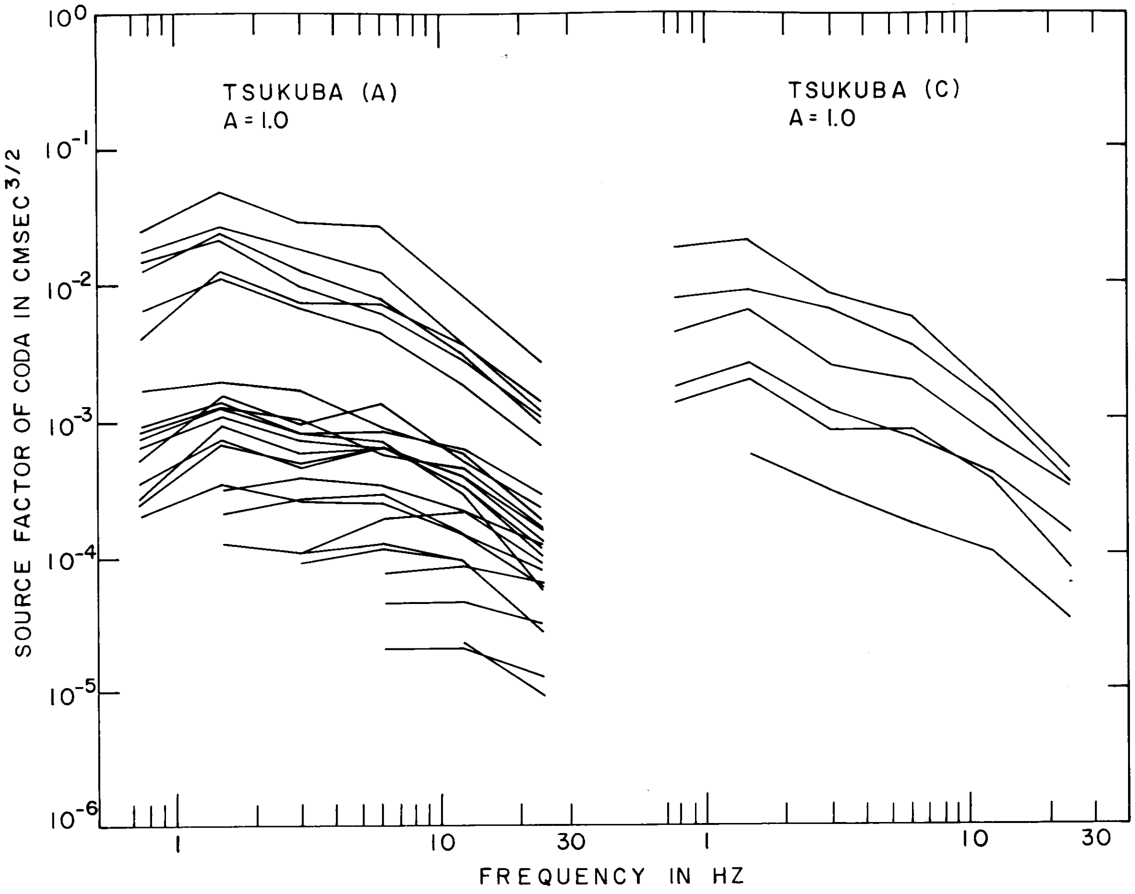

Fig. 4.6. Source factors of coda in the range of 0.75 to 24 Hz for the events recorded at Tsukuba, Japan. The source factors are slightly richer in high frequencies in region A than in region C (see Figure 3.9).

in high frequencies in region A than in region C (see Fig. 3.9). To the exception of two larger earthquakes, the spectral shape of coda source factor at Oishiyama is practically flat and does not even seem to depend on earthquake magnitude.

These various features observed in the growth of the coda source factor for each area may be more clearly seen if we plot the source factor at one frequency as a function of the source factor at another. For example, in Fig. 4.7 we plot the coda spectral amplitude at 12 and 24 Hz versus 1.5 or 3 Hz for the events recorded at Stone Canyon. Each point represents an earthquake as derived directly from Fig. 4.1. The non-linear trend in these plots is approximated by segments of lines drawn through the data such as to minimize the perpendicular distances from the data points to the line with the additional constraint that the slope and relative position of the resulting segments obtained at various frequencies be consistent with the smooth spectral curve of earthquake source shown in Fig. 4.11b. The magnitudes of the events shown in Fig. 4.7 range from 1 to 3.3 and the break in the slope of the lines drawn through these earthquakes occurs at a magnitude of about 2.1. The good fit of the straight line with slope unity for the smaller events implies that the spectral shape of these earthquakes does not change with magnitude in the frequency range of 1.5 to 24 Hz. For events larger than M2.1, however, a change in spectral shape of earthquake source is clearly indicated by the slower rate of

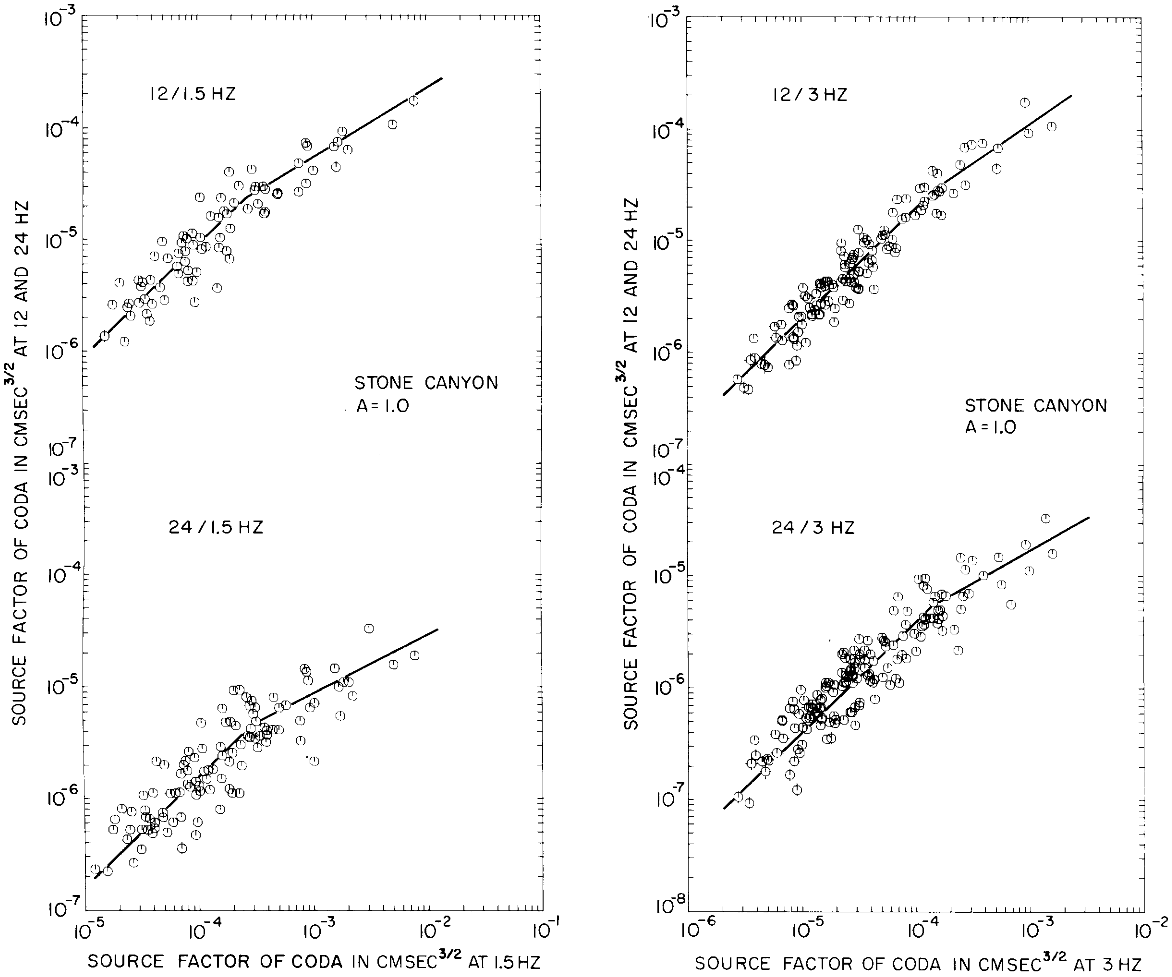

Fig. 4.7. Relations between the coda source factors at 12 and 24 Hz and the coda source factors at 1.5 or 3 Hz for the events recorded at Stone Canyon, central California. The rates of increase of the spectral densities are the same at various frequencies for the smaller events, but above approximately M2.1, the rates of increase become smaller for the spectral densities at 12 and 24 Hz than for the spectral densities at 1.5 or 3 Hz, indicating a change in the shape of earthquake source with increasing magnitude in the frequency range of 1.5 to 24 Hz.

increase in the spectral densities* at 12 and 24 Hz in relation to the spectral densities at 1.5 or 3 Hz. The earthquakes recorded at Bickmore Canyon, which share the same source region as the earthquakes recorded at Stone Canyon (see Figures 3.4 and 3.5) but range in magnitude from 2 to 4, further confirm this scale effect. The slow rate of increase of the source factors at 13.5 Hz compared to the rate of increase of the source factors at 3 Hz for these events (Fig. 4.2b) is consistent with the growth rates observed in the larger earthquakes at Stone Canyon. A similar behavior is again seen in the bandwidth of 3 to 12 Hz for the events with magnitudes ranging from 1.3 to 3 recorded at Kilauea (Fig. 4.8). In this particular series of events the data points at 24 Hz were not considered for the scaling because the high attenuation ($Q = 450$ as shown in Fig. 5.2) and uncertainty in the path correction of the coda at this frequency caused too much variability in the source factor estimates.

For earthquakes with magnitudes from 1.3 to 3 at San Fernando, the relative growth of the spectral amplitudes of coda is the same at 1.5 and 24 Hz (Fig. 4.3b) and although not shown here, it is the same also at 3, 6 and 12 Hz. At Oishiyama (Fig. 4.9) a small deviation from the slope unity

---

*More precisely, these are spectral densities per unit of square root of bandwidth which, for the special case of the factor a (equation 3.8) fixed to 1, have the dimension of cm $\sec^{3/2}$.

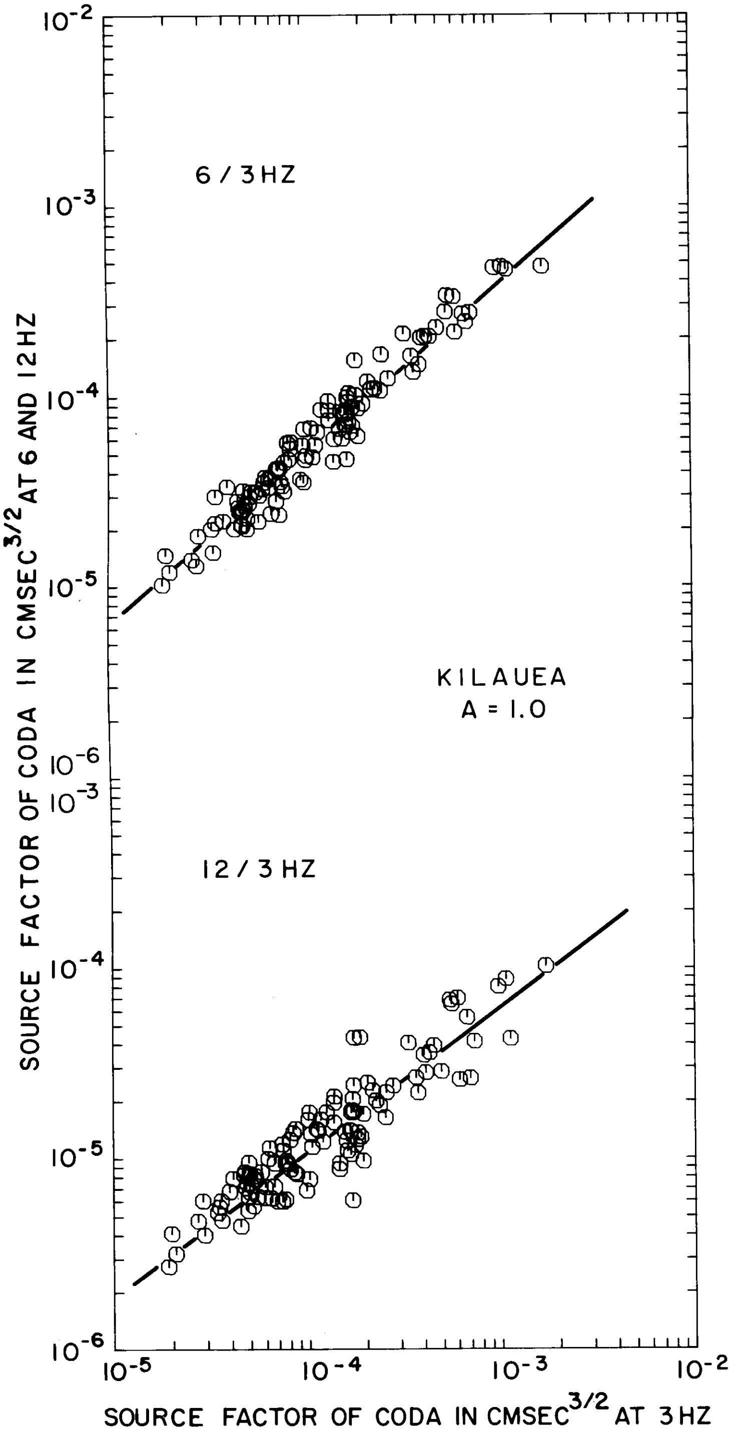

Fig. 4.8. Relations between the coda source factors at 6 and 12 Hz and the coda source factors at 3 Hz for the events recorded at Kilauea, Hawaii. The rates of increase of the spectral densities are slower at 6 and 12 Hz than at 3 Hz, indicating a change in the spectral shape of these earthquakes with increasing magnitude in the frequency range of 3 to 12 Hz.

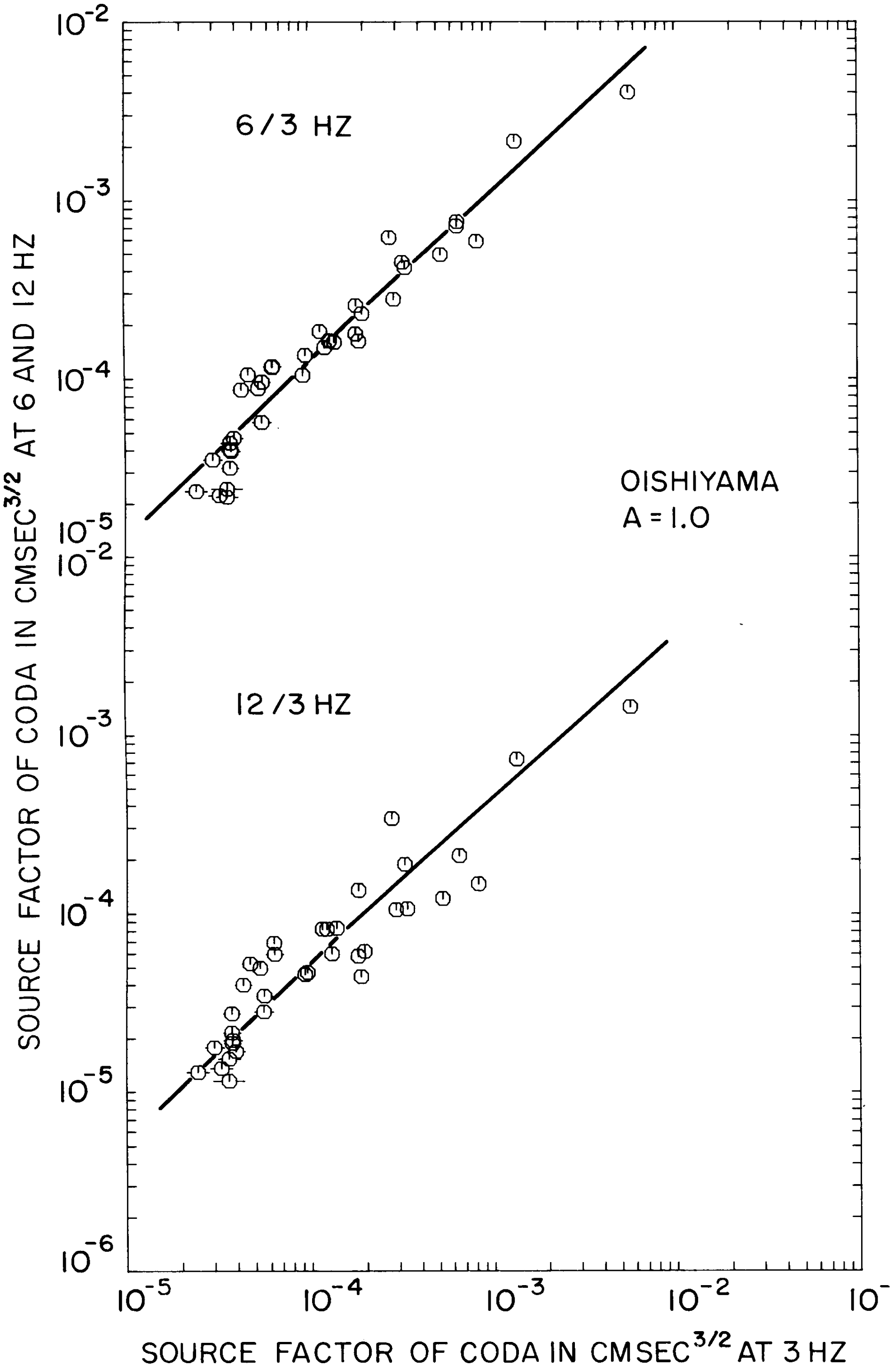

Fig. 4.9. Relations between the coda source factors at 6 and 12 Hz and the coda source factors at 3 Hz for the events at Oishiyama. The relative growth of the spectral amplitudes is only weakly dependent on magnitude as indicated by the slight departure from the slope unity required in the lines drawn to fit the larger events observed.

is required in the lines shown at 6/3 Hz and 12/3 Hz to fit the larger events in the observed magnitude range of 2 to 4.

For the sake of clarity, only the errors larger than 9% which exceed the size of the circles used to represent the data points, are shown in the above figures. Most residuals are of the order of 5 to 10%, the largest error being about 20%. The spread of the data about the line for a given magnitude thus cannot be explained in terms of least square residuals but rather is a reflection of the actual variability between coda source factors. Some of this fluctuation may undoubtedly be attributed to variations between earthquake sources. At Stone Canyon, the larger spread observed in the plot of the source factors at 24 Hz relative to those at 1.5 Hz (Fig. 4.7) is also related to a temporal change in the coda excitation (see Table 8b). This effect will be further discussed in section 4.4 and in Chapter 5. A comparison of the trends depicted in Figs. 4.2b, 4.3b, 4.7, 4.8 and 4.9, however, demonstrates beyond any doubt that for the frequencies considered, the relative growth of the coda source factors with magnitude is different for earthquakes at Kilauea and for large earthquakes within the San Andreas rift zone than for earthquakes at San Fernando and Oishiyama, or smaller events occurring on the San Andreas. Let us now find how the differences observed in these various figures are projected into the differences in the scaling law of earthquake source spectra.

4.3 Construction of the scaling law

The source factor of coda amplitude is proportional to the square root of total seismic energy within a unit frequency band around ω (equation (2.15)) or equivalently to the absolute value of the Fourier transform of primary waves at a reference distance in the far field (equation (2.19)). Then the relative values of the source spectrum for two different earthquakes can be determined from the ratio of the source factor of coda amplitude. In order to fix their absolute values, however, one must apply more direct methods to at least one of the earthquakes. We shall apply the far field solution of an infinitesimal dislocation buried in an infinite medium (e.g., Maruyama, 1963) to the smallest and closest earthquakes for which the distance to the station is short enough for scattering to be negligible and long enough to be in the far field.

Examples of the records of these smallest and closest earthquakes obtained by the Tsujiura band-pass filter seismograph are shown for Stone Canyon in Figure 4.10. They show simple P and S wavelets, suggesting the validity of applying the simple far field solution outlined above. Similar records are used at San Fernando, Kilauea, and Oishiyama. Unfortunately, we cannot find such simple records for Tsukuba because the nearest earthquakes there are more than 40 km away, which is too far.

On the assumption that coda waves are mostly composed of shear waves, as postulated by Aki and Chouet (1975), the

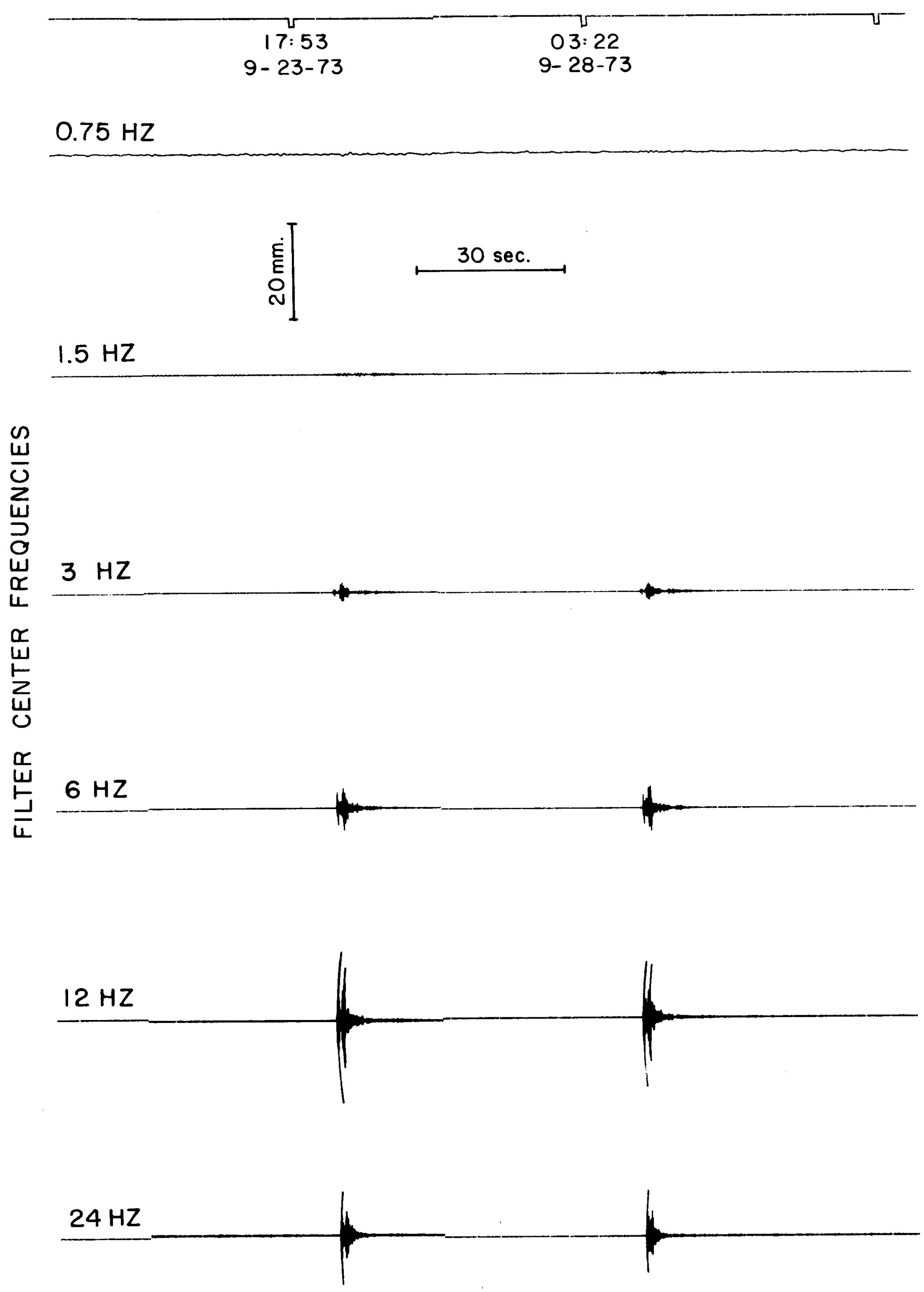

Fig. 4.10. Typical events recorded on the band-pass seismograph and used to determine the absolute level and spectral characteristics of the M0.85 earthquake at Stone Canyon. These small events show clear P and S pulses with very little scattering, thereby suggesting the applicability of the direct deterministic analysis. Similar events are used to determine the spectra of the M1.3 earthquake at San Fernando, M0.7 earthquake at Kilauea, and M1.2 earthquake at Oishiyama.

choice of S waves appears more natural to define the absolute spectrum upon which the relative measurements from the source factors of coda are to be superposed. Consider then a point dislocation source with the seismic moment having the Fourier transform $M(\omega)$. The Fourier transform $F(\omega)$ of displacement due to far field S waves in an unbounded homogeneous elastic medium at a distance r from the source can be written as

$$|F(\omega)| = c(4\pi\rho\beta^3 r)^{-1} \dot{M}(\omega) \qquad (4.1)$$

where c is a geometrical factor equal to or less than 1, ρ is the density, β is the shear-wave velocity, and $\dot{M}(\omega)$ is the Fourier transform of the time derivative of seismic moment. For a band-passed signal with $|F(\omega)| = F$ (constant) in $\omega_o < |\omega| < \omega_1$, $|F(\omega)| = 0$ otherwise, and $\phi(\omega) = 0$ for all ω, the corresponding signal f(t) is written as

$$f(t) = \frac{1}{2\pi} \int_{-\omega_1}^{-\omega_o} Fe^{i\omega t} d\omega + \frac{1}{2\pi} \int_{\omega_o}^{\omega_1} Fe^{i\omega t} d\omega$$

$$= 2Ff_1 \frac{\sin\omega_1 t}{\omega_1 t} - 2Ff_o \frac{\sin\omega_o t}{\omega_o t} \qquad (4.2)$$

where $f_o = \omega_o/2\pi$ and $f_1 = \omega_1/2\pi$. The maximum amplitude is at $t = 0$ and is equal to

$$f_o = 2F(f_1 - f_o) = 2F\Delta f \qquad (4.3)$$

Thus for a rough approximation the amplitude of a wavelet is the product of its amplitude spectral density and twice the bandwidth. From known bandwidth of the band-pass filter and the amplitude of the S wave measured on the record we estimate $F(\omega)$ for many small events with similar sizes, then correct each source spectrum for attenuation as described below and finally average over the resulting ensemble to obtain the source spectrum of the reference earthquake from which the scaling law is constructed.

The reference earthquake at Stone Canyon is based on two events (Table 9 and Fig. 4.10) at hypocentral distances of 6.6 and 4.2 km. For the direct paths of S waves within this distance range along the San Andreas values of Q_β between 20 and 150 seem reasonable (Kurita, 1975; Bakun and Bufe, 1975; Bakun et al. 1976). While a Q_β of 20 is clearly too low in our case, an intermediate Q_β of 65 produces spectra which are fairly flat at the low frequency end and decay with frequency roughly proportional to ω^{-2} beyond the corner frequency (Fig. 4.11a). The spectral curve smoothed through this data (Fig. 4.11b) shows a constant value of 4.4×10^{-7} cm sec at low frequency and has a corner frequency f_o at about 13 Hz.

TABLE 9. Events Used to Fix the Absolute Level of Earthquake Source Spectrum at Stone Canyon.*

Event	Date	Origin Time, UT	North Latitude	West Longitude	Depth, km	Magnitude
1	9/23/73	17h53m05.1s	36°36.5'	121°14.8'	5.7	0.9
2	9/28/73	03h22m07.9s	36°37.0'	121°15.2'	3.5	0.8

* Event parameters determined by U.S.G.S.

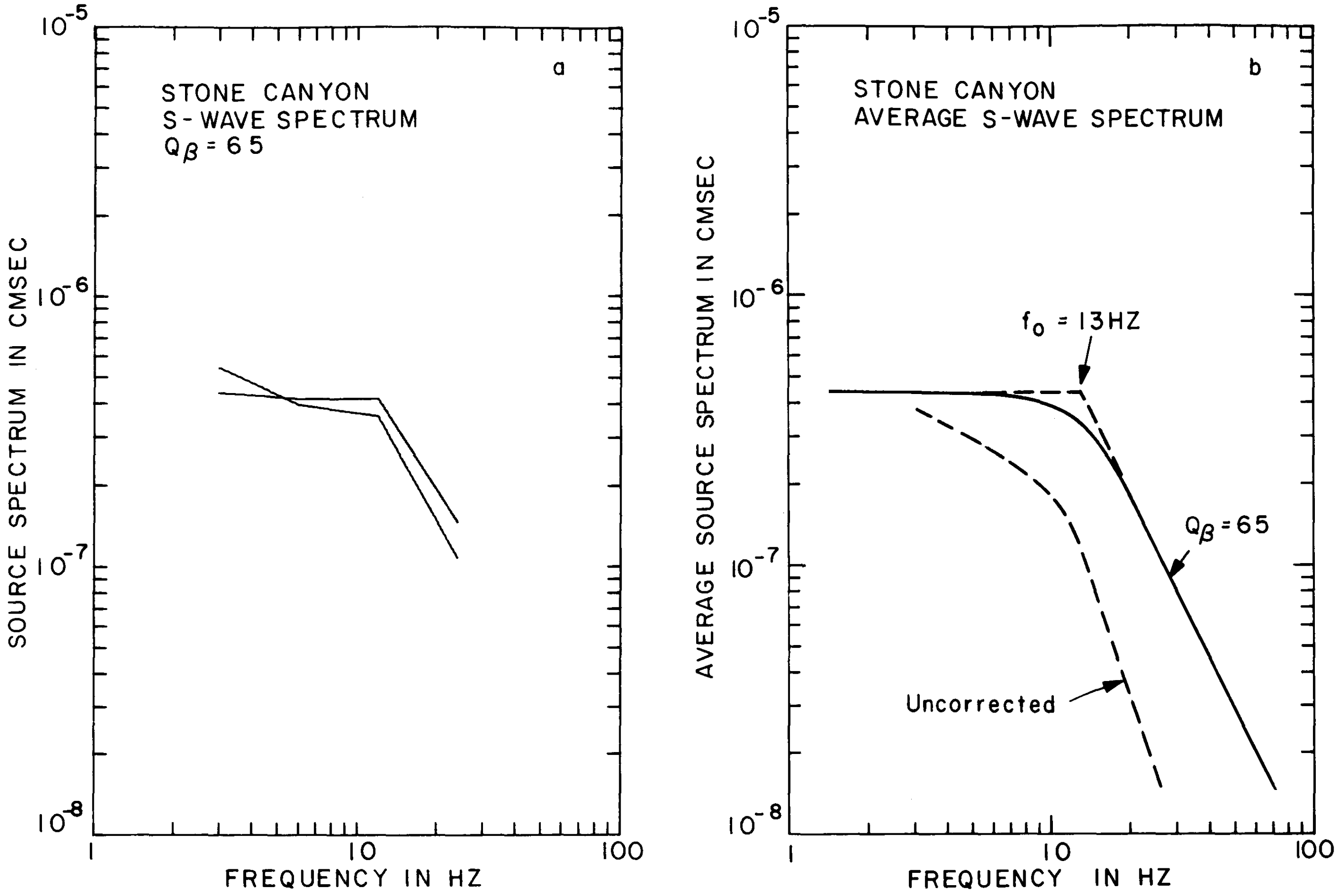

Fig. 4.11. S wave spectra for the smallest and closest earthquakes at Stone Canyon. a) Original spectra corrected for attenuation with $Q_\beta = 65$, and b) resulting average spectrum, with the approximate corner frequency of 13 Hz. The uncorrected average spectrum is shown for comparison.

According to the data from Table 9 this average earthquake is given the magnitude 0.85.

At San Fernando, 25 earthquakes within 14 km of station PAC (Table 10) are available for the determination of a reference spectrum. Their magnitude is estimated at 1.3 from the values of the moment. Following Tucker and Brune (1973) we assume a Q_β of 250 to be characteristic of the area near Pacoima Canyon and compute the corrected source spectra shown in Fig. 4.12a. The average spectrum for these events has frequency characteristics similar to those of the average event at Stone Canyon. The corner frequency of the reference earthquake is at 5 Hz and the level of the flat part of its spectrum is at 1.1×10^{-6} cm sec (Fig. 4.12b).

Because of the lack of S wave attenuation data at Kilauea, attempts to correct the spectra at this location are made by assuming various values of Q_β ranging from 50 to 300. Values of Q_β below 200 are too low, producing spectra which tend to decay with slopes shallower than ω^{-1} or even grow with frequency. A value of 250 identical to that used at San Fernando, however, gives reasonable spectra similar in their features to those obtained in California. The corrected spectra shown in Fig. 4.13a are calculated from S waves of 15 earthquakes within 6 km from the station. Accurate locations being not available for these shocks, their hypocentral distances are computed from the S-P delays measured on their band-passed seismograms. From the values of the moment and total duration of the signals, their magnitude is

TABLE 10. Events Used to Fix the Absolute Level of Earthquake Source Spectrum at San Fernando*

Event	Date	Origin Time, UT	North Latitude	West Longitude	Depth, km
1	8/14/74	15h12m50.1s	34°19.9'	118°23.9'	9.9
2	8/14/74	15h18m09.2s	34°19.9'	118°23.9'	10.6
3	8/14/74	15h55m09.8s	34°20.9'	118°30.2'	0.2
4	8/14/74	15h55m18.8s	34°21.4'	118°30.2'	1.6
5	8/14/74	16h35m31.2s	34°22.3'	118°28.6'	8.0
6	8/14/74	17h13m18.9s	34°21.5'	118°29.4'	1.7
7	8/14/74	18h22m08.3s	34°22.4'	118°31.2'	3.5
8	8/14/74	18h47m20.1s	34°21.5'	118°30.2'	2.4
9	8/14/74	18h51m48.8s	34°20.8'	118°29.1'	2.3
10	8/14/74	19h37m34.2s	34°22.3'	118°28.6'	8.0
11	8/14/74	21h28m22.1s	34°19.9'	118°23.9'	10.5
12	8/14/74	22h58m59.2s	34°17.7'	118°24.7'	8.0
13	8/15/74	03h32m35.3s	34°22.8'	118°21.2'	8.0
14	8/15/74	12h41m03.6s	34°21.8'	118°28.8'	4.7
15	8/16/74	00h32m16.4s	34°19.9'	118°23.9'	8.0
16	8/16/74	12h44m16.5s	34°22.1'	118°20.6'	3.8
17	8/17/74	07h39m07.5s	34°20.5'	118°21.7'	0.6
18	8/17/74	08h00m21.3s	34°19.9'	118°23.9'	13.3
19	8/17/74	08h01m02.6s	34°20.5'	118°24.2'	0.9
20	8/17/74	10h40m26.8s	34°19.9'	118°23.9'	8.0
21	8/20/74	00h47m32.8s	34°24.7'	118°29.7'	3.2
22	8/21/74	16h08m00.8s	34°23.5'	118°24.1'	10.1
23	8/22/74	08h36m35.3s	34°22.4'	118°24.1'	11.5
24	8/27/74	23h38m32.3s	34°23.5'	118°24.1'	11.7
25	8/28/74	06h16m37.9s	34°24.1'	118°21.0'	8.3

---

* Events parameters determined with additional data from the C.I.T. seismic network in southern California.

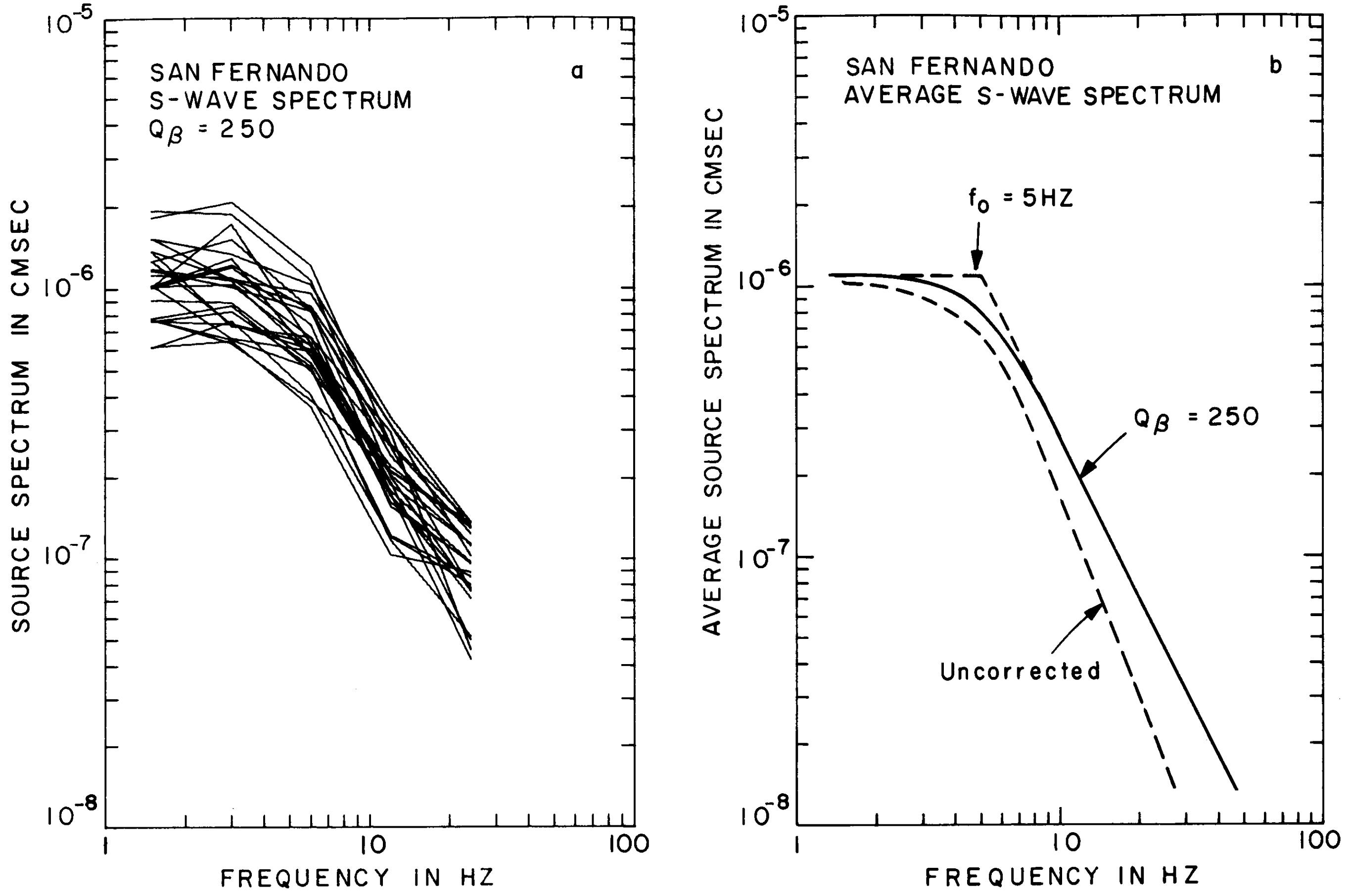

Fig. 4.12. S wave spectra for the smallest and closest earthquakes at San Fernando. a) Original spectra corrected for attenuation with Q_β = 250, and b) resulting average spectrum, with the approximate corner frequency of 5 Hz. The uncorrected average spectrum is shown for comparison.

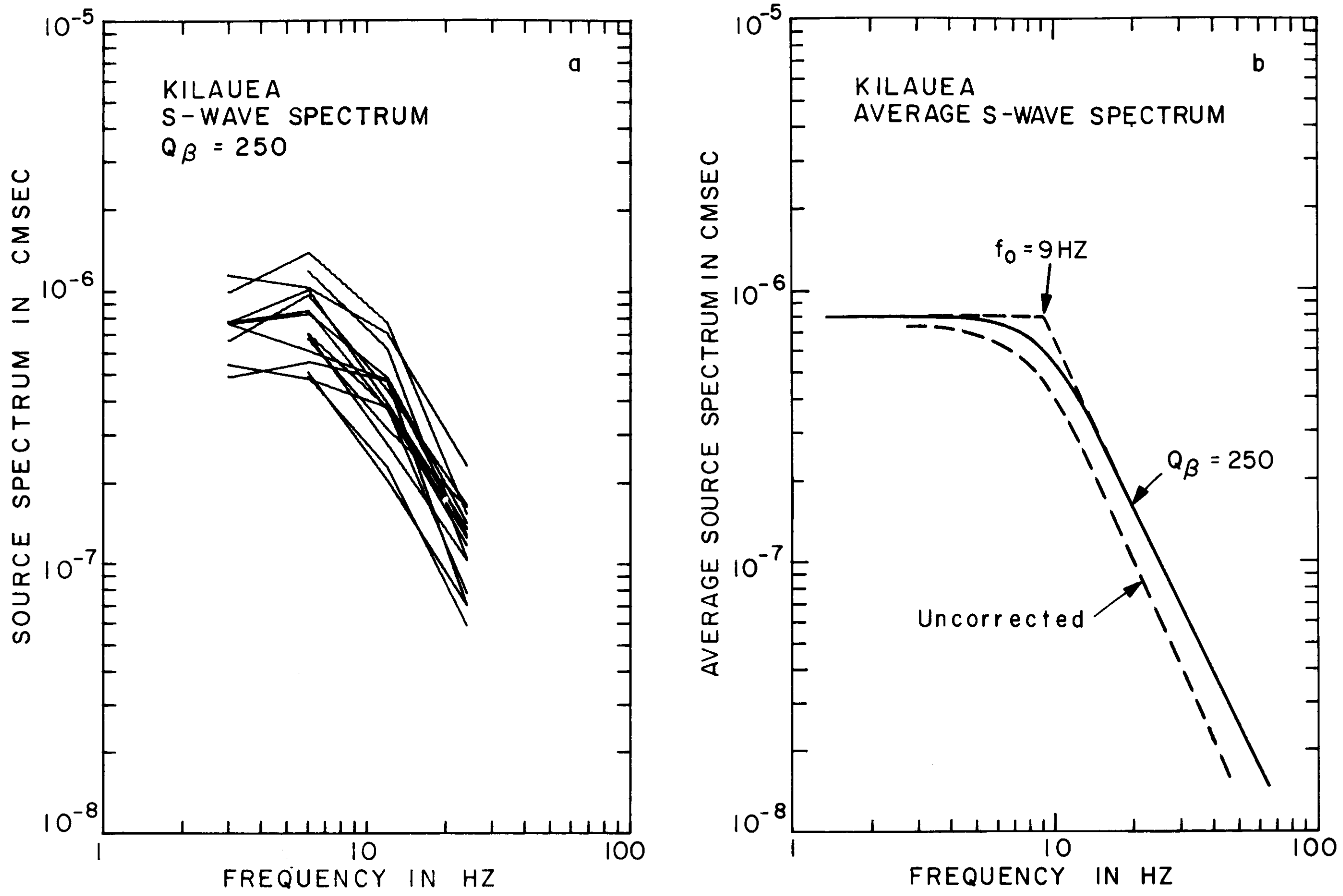

Fig. 4.13. S wave spectra for the smallest and closest earthquakes at Kilauea. a) Original spectra corrected for attenuation with Q_β = 250, and b) resulting average spectrum, with the approximate corner frequency of 9 Hz. The uncorrected average spectrum is shown for comparison.

estimated at 0.7. An ω^2-model approximating the corrected spectra is shown in Fig. 4.13b. The average spectral curve has the low frequency level at 8×10^{-7} cm sec and shows a corner frequency at 9 Hz.

As for Kilauea, S wave attenuation data are not available at Oishiyama, and several values of Q_β are assumed in order to correct the available spectra in this area. On the basis of preliminary results obtained with quality factors ranging from 100 to 400, and owing to the limited spectral resolution of the two earthquakes selected at this station, a Q_β of 200 seems appropriate. The corrected spectra of the two shocks are shown in Fig. 4.14a. The spectral curve drawn through this data has a corner frequency f_o at about 8 Hz and a constant low frequency level of 8.8×10^{-7} cm sec (Fig. 4.14b). The hypocentral distances of these events calculated from their S-P delays, are about 16 km, and their magnitude estimated from the values of the moment is 1.2.

Source spectra of the type shown in Figs. 4.11 through 4.14 have been obtained by Brune (1970) and others who followed his approach (Douglas and Ryall, 1972; Thatcher, 1972; Hanks and Wyss, 1972; Tucker and Brune, 1973; Thatcher and Hanks, 1973). The source spectra $|\dot{M}(\omega)|$ calculated from $|F(\omega)|$ according to (4.1) are shown at the bottom of Figures 4.15, 4.16, 4.17 and 4.18 for the four regions in which an absolute source spectrum is available. For these computations, the factor c in (4.1) was assigned the value 0.8, correcting

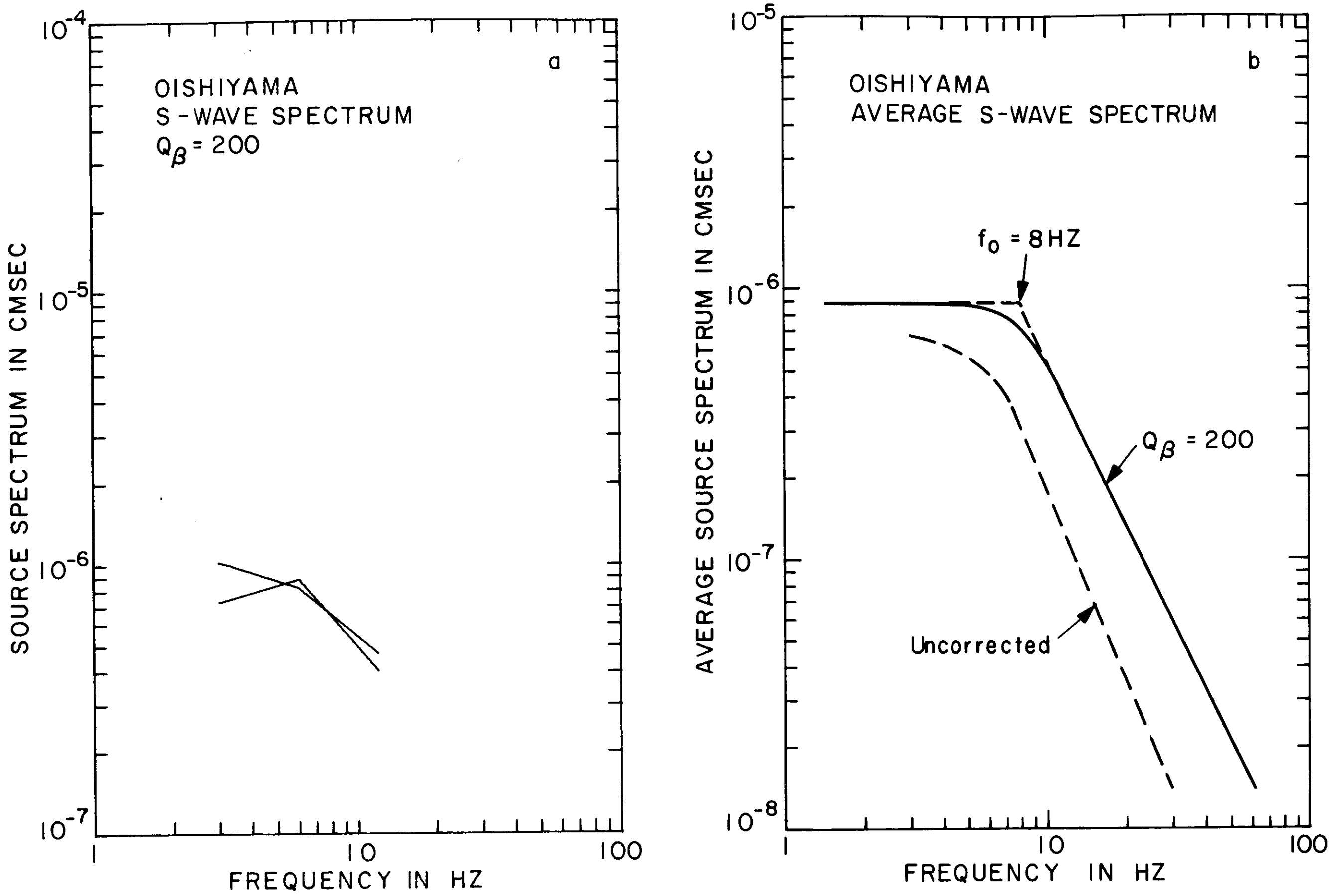

Fig. 4.14. S wave spectra for the smallest and closest earthquakes at Oishiyama. a) Original spectra corrected for attenuation with Q_β = 200, and b) resulting average spectrum, with the approximate corner frequency of 8 Hz. The uncorrected average spectrum is shown for comparison.

both for the RMS average of the shear displacement radiation pattern and for free surface effect. The seismic moment of the average M0.85 event at Stone Canyon (Fig. 4.15) was estimated using $\beta = 3.5$ km/sec, $\rho = 2.7$ g/cm^3 (Bakun et al., 1976), an average hypocentral distance r of 5.4 km, and with $|F(\omega = 0)| = 4.4 \times 10^{-7}$ cm sec. The value of the moment is 4.3×10^{17} dyne cm or $\log_{10} |\dot{M}(\omega = 0)| = 17.6$, as indicated in the vertical coordinate of Fig. 4.15. Similarly, we calculated the seismic moment of the M1.3 event at San Fernando (Fig. 4.16) assuming $\beta = 3.5$ km/sec and $\rho = 2.8$ g/cm^3 (Tucker and Brune, 1973). The small events recorded at PAC are located at an average hypocentral distance of 11.5 km. Then, with $|F(\omega = 0)| = 1.1 \times 10^{-6}$ cm sec we obtained a moment of 2.4×10^{18} dyne cm or $\log_{10} |\dot{M}(\omega = 0)| = 18.4$, as shown in Fig. 4.16. The S wave velocity at shallow depth near Kilauea is about 2.4 km/sec (Eaton, 1962; Ryall and Bennett, 1968; Hill, 1969). Assuming $\rho = 2.7$ g/cm^3, an average hypocentral distance of 4.7 km for the 15 events selected, and with $|F(\omega = 0)| = 8 \times 10^{-7}$ cm sec as derived above, the seismic moment of the M0.7 earthquake in Hawaii is 2.2×10^{17} dyne cm or $\log_{10} |\dot{M}(\omega = 0)| = 17.3$ (Fig. 4.17). Finally, at Oishiyama, we used $\beta = 2.7$ km/sec, $\rho = 3$ g/cm^3 (Ishida, 1974), $r = 16$ km, and $|F(\omega = 0)| = 8.8 \times 10^{-7}$ cm sec to obtain a moment of 1.4×10^{18} dyne cm or $\log_{10} |\dot{M}(\omega = 0)| = 18.1$ as indicated on the vertical axis of Fig. 4.18.

Once the *absolute* value of source spectrum for the smallest earthquake is fixed, those for greater earthquakes can be obtained by using the source factor of coda amplitude relative to that of the smallest earthquake. Let us start, for example, with the data from Stone Canyon and construct a family of spectral curves by superposing the relative spectral densities shown in Figs. 4.2b and 4.7 over the absolute spectral curve for M0.85 earthquakes shown in Fig. 4.11b. Starting with the 12 Hz/3 Hz and 24 Hz/3 Hz plots in Fig. 4.7, we find from the magnitudes attached to the source factors that the average M0.85 earthquake has a source factor of coda of 3×10^{-6} cm sec$^{3/2}$ at 3 Hz while the average M 2.1 event has a source factor of 1.4×10^{-4} cm sec$^{3/2}$ at the same frequency. This represents a relative growth in the spectral amplitudes at 3 Hz in the ratio of 1.4×10^{-4} cm sec$^{3/2}$/ 3×10^{-6} cm sec$^{3/2}$ or a contribution of 1.67 units in the logarithmic scale of Fig. 4.15. By making the same measurement at the other available filter frequencies we obtain a set of points through which the spectral curve for M2.1 earthquakes can be drawn. The procedure repeated for events up to magnitude 4 then yields the results summarized in Fig. 4.15. From the smallest event at M0.85 and up to magnitude 2.1 the spectral shape of earthquake source remains unchanged as required by the segments with slope unity in Fig. 4.7. Above magnitude 2.1, however, the superposition upon the spectrum for M2.1 earthquakes of the strong scale effect on spectral shape observed in Figs. 4.2b and 4.7 results in a decrease of

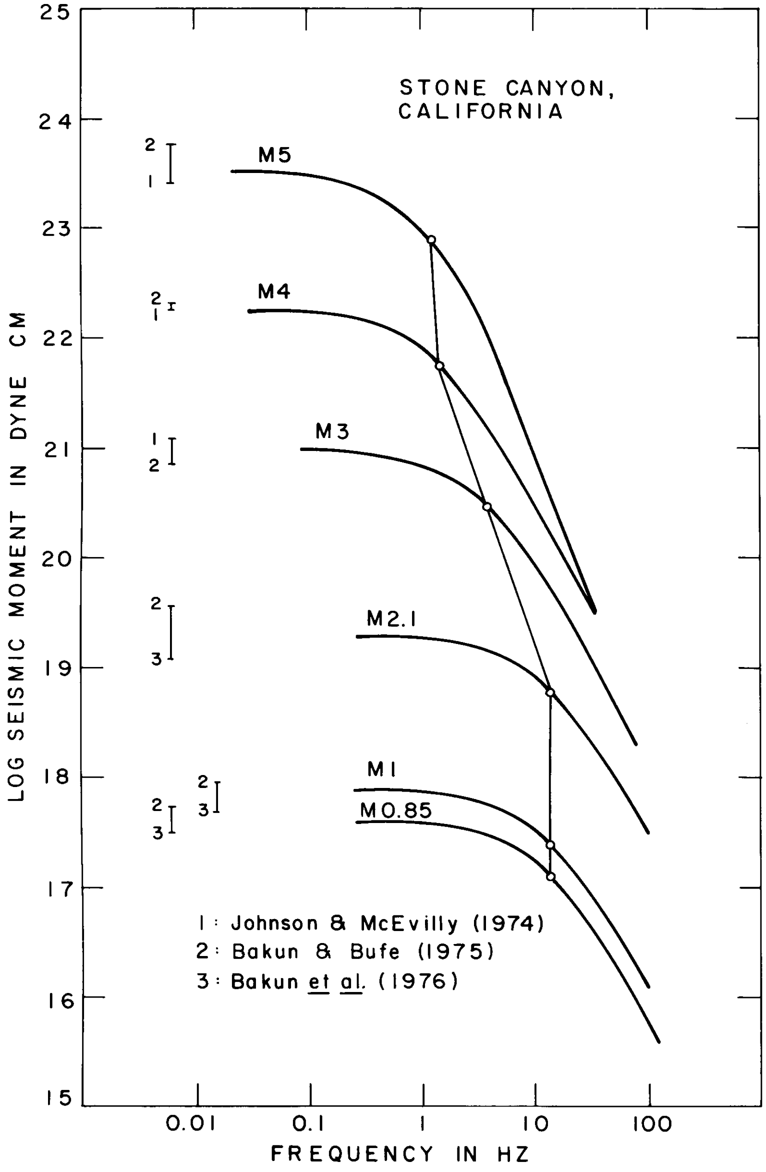

Fig. 4.15. Growth of the seismic source spectrum with magnitude for earthquakes within the San Andreas rift zone near Stone Canyon, central California. The locus of corner frequencies appears to consist of 3 distinct segments between the M1 and M5 earthquakes. The first segment, along the line of constant corner frequency, and the third segment, along a path of weakly decreasing corner frequency, reflect inhomogeneity lengths characteristic to the earth's crust in the area. The intermediate segment, with the slope -3 expected from the similarity assumption underlying the ω^2-law, reflects a characteristic strength of the crust in that same area. As indicated at the left of the spectral curves, the seismic moments obtained at Stone Canyon compare well on an absolute scale with those predicted from the relations between seismic moment and local magnitude obtained in the area by Johnson and McEvilly (1974), Bakun and Bufe (1975), and Bakun et al. (1976).

corner frequency with increasing magnitude from 13 Hz down to 1.5 Hz at M4 along a path which the slope -3. All the spectra from M0.85 and up to M4 earthquakes decay roughly like ω^{-2} beyond the corner frequency. The frequency content of these spectra is fixed with good accuracy in the range of 1.5 to 24 Hz from the data of Fig. 4.7.

A very strong scale effect is found on the seismic spectrum at Stone Canyon beyond M4 as indicated in Table 11. Incorporating this effect into Fig. 4.15 we observe that the corner frequency now decreases weakly with increasing magnitude from 1.5 Hz at M4 down to about 1.3 Hz at M5. It is also interesting to note that the high-frequency asymptote of ω^{-2} for the M4 earthquakes becomes distinctly steeper for the M5 earthquakes.

The upper bound given by the M5 earthquakes and lower bound determined for the smallest and closest earthquakes in Fig. 4.15 appear to divide 6 decades of seismic moment range into 4 units of local magnitudes. This is consistent with the relations of seismic moment and local magnitude obtained by Wyss and Brune (1968), Aki (1969), and Thatcher and Hanks (1973). Furthermore, as indicated by the vertical bars shown at the left of the spectral curves drawn in Fig. 4.15, the seismic moments obtained at Stone Canyon compare well on an absolute scale with those predicted from the relations between seismic moment and local magnitude obtained in the Bear Valley area by Johnson and McEvilly (1974), Bakun and

TABLE 11. Spectral Ratios

	Magnitude Ratios		
Frequency, Hz	4.4/3.5*	5.5/4.4*	5/4+
0.75	10	55	13
1.5	8	50	10
3	5	22	9
6	3	20	3
12	2	16	2
24	-	15	1.5

* Values for Oishiyama.

\+ Value for Stone Canyon.

Bufe (1975), and Bakun et al. (1976).

On the other hand, when we superpose the data shown in Fig. 4.3b upon the absolute spectrum of the M1.3 event at San Fernando (Fig. 4.12b), we find that the corner frequency is kept constant at about 5 Hz for the magnitude range extending from 1.3 to 3 as indicated in Fig. 4.16. The fixed corner frequency within this magnitude range is somewhat lower than the average value of the corner frequencies derived by Tucker and Brune (1973) for SH waves from aftershocks of the 1971 San Fernando earthquake. The spectrum of the San Fernando earthquake, with a seismic moment of 10^{26} dyne cm, corner frequency at around 0.1 Hz and high-frequency decay roughly like ω^{-2}, has been well established (Hanks, 1974, 1975). Hanks (1975) found that southern California earthquakes of magnitudes greater than 6 including the San Fernando earthquake have roughly a constant stress drop independent of magnitude. The locus of corner frequency for these events is shown extrapolated down to the M3 event in Fig. 4.16. The apparent good fit of the locus of corner frequency derived from our study with the extrapolated locus from Hanks' data at M3 is harmonizing, but cannot be considered as established since no data was available to us for events of magnitudes larger than 3. The seismic moments of the M1.3 and M3 events at San Fernando are compared at the left of the spectra shown in Fig. 4.16 with those for events of the same sizes in southern California as derived according to the relations of moment and local magnitude obtained by Wyss and Brune (1968)

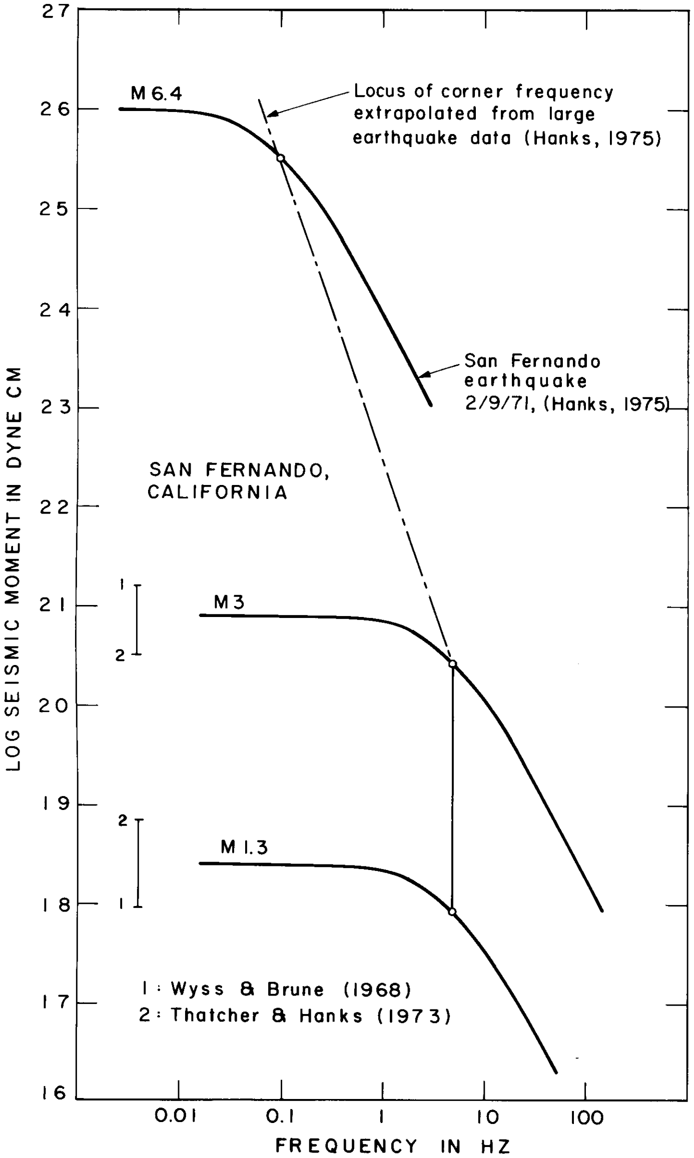

Fig. 4.16. Growth of the seismic source spectrum with magnitude for earthquakes in the San Fernando area, southern California. The locus of corner frequencies shown by the vertical line extending from the M1.3 event to the M3 event reflects an inhomogeneity length characteristic to the earth's crust in the area. The locus of corner frequencies shown by the dashed line between the M3 and M6.4 earthquakes is extrapolated from Hanks' (1975) data in southern California. The intersection at M3 of this constant stress drop path with the path derived in our study is harmonizing, but cannot be considered as established since no data was available to us for events of magnitudes larger than 3. The seismic moments of the M1.3 and M3 earthquakes at San Fernando are compared at the left of the spectral curves with those for events of the same sizes in southern California as derived according to the relations of moment and local magnitude obtained by Wyss and Brune (1968) and Thatcher and Hanks (1973).

and Thatcher and Hanks (1973).

A yet different scaling law is found at Kilauea for earthquakes with magnitudes ranging from 0.7 to 3. To fill the gap between the absolute spectrum of the M0.7 event shown in Fig. 4.13b and M1.3 events at the lower end of the magnitude range depicted in Fig. 4.8 we assume that the trend shown by the spectral amplitudes plotted in this figure remains unchanged down to the magnitude 0.7. Then, using the spectrum of the M0.7 earthquake as a reference for the frequency content between 3 and 12 Hz of the larger events, we derive the scaling law shown in Fig. 4.17 by fixing the seismic moment of the M3 earthquake to the value 10^{21} dyne cm, a value equivalent to those found at Stone Canyon and San Fernando for events of the same magnitude. The path of the corner frequency from 9 Hz at M0.7 down to about 0.9 Hz at M3 implies a weak increase of stress drop with magnitude in that observed range.

The manner in which the spectrum for earthquakes near Oishiyama changes with increasing magnitude (Fig. 4.18) is quite similar to that found in the earthquakes at San Fernando. The corner frequency is kept constant in the magnitude range from 1.2 to 2.7 and decreases for magnitudes greater than 2.7. The path of constant corner frequency at 8 Hz is fixed by the absolute spectrum for M1.2 earthquakes shown in Fig. 4.14b and the trend of the spectral amplitudes of coda (Fig. 4.9) extrapolated down to this magnitude. Beyond M2.7

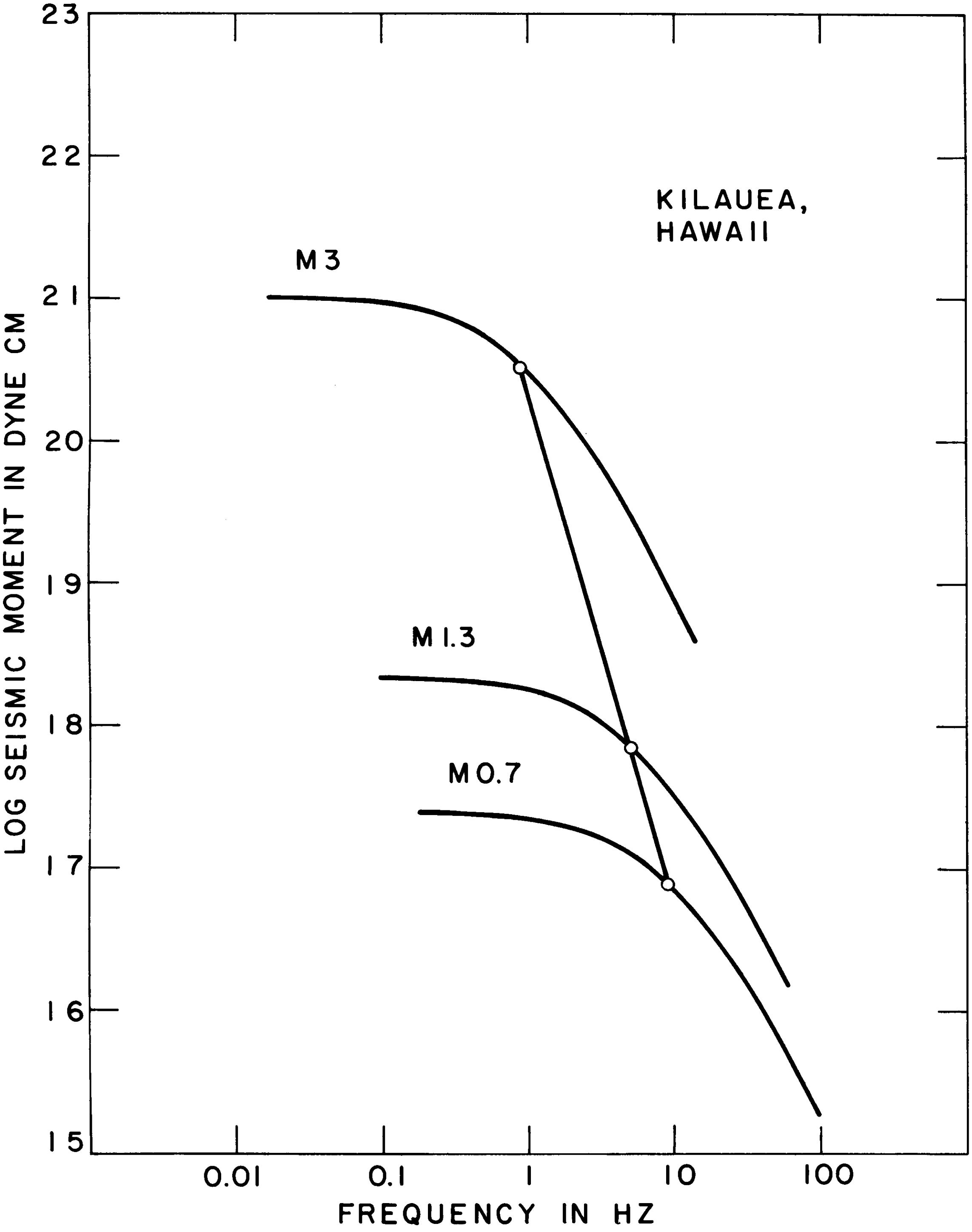

Fig. 4.17. Growth of the seismic source spectrum with magnitude for earthquakes in the Kilauea area, island of Hawaii. The locus of corner frequencies implies a weak increase of the stress drop with magnitude in the observed range.

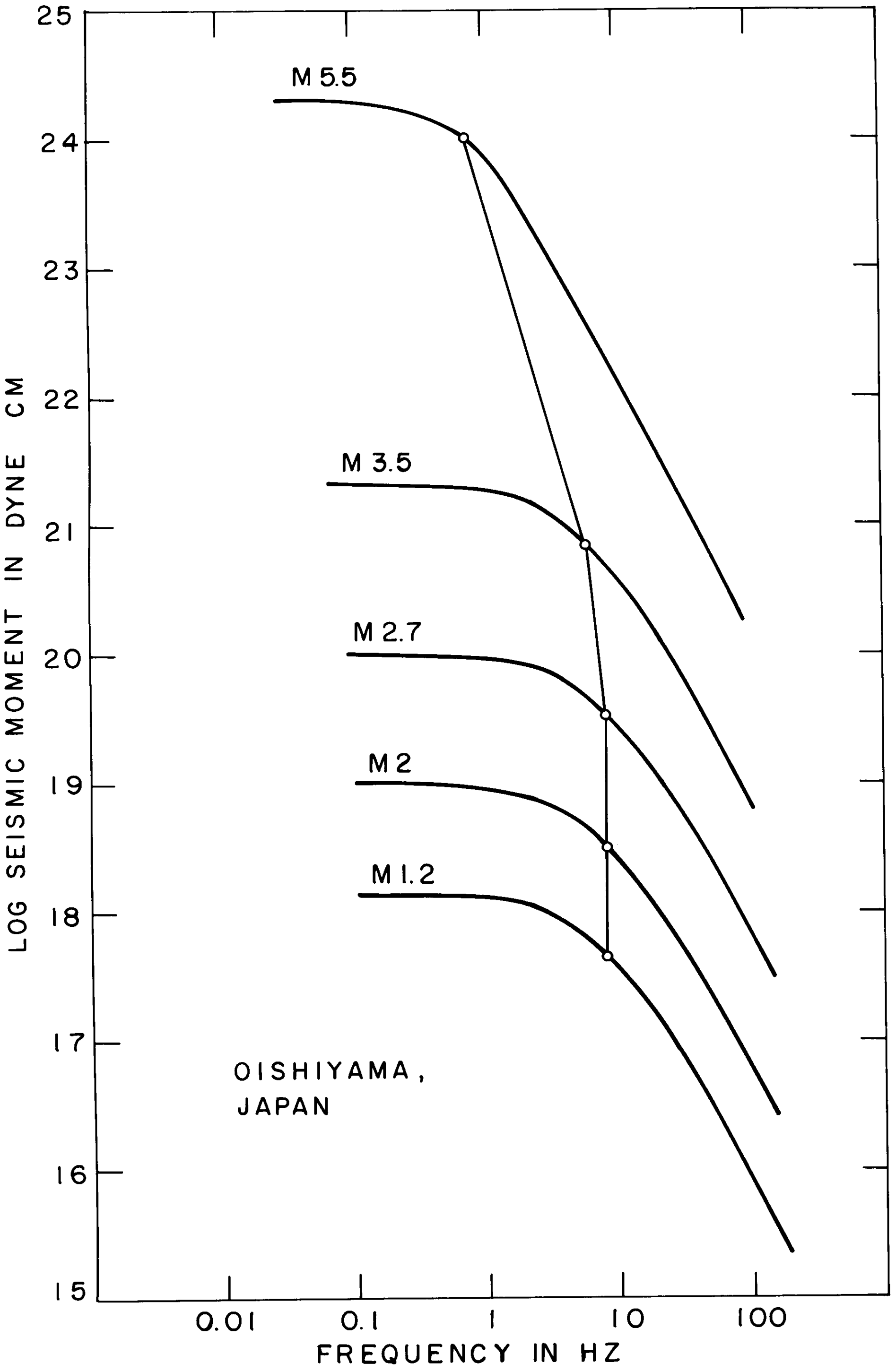

Fig. 4.18. Growth of the seismic source spectrum with magnitude for earthquakes at Oishiyama, Japan. The manner in which the spectrum changes with increasing magnitude is quite similar to that found for the earthquakes at San Fernando.

the slightly gentler slopes of the source factors plotted in Fig. 4.9 lead to a small decrease in corner frequency down to approximately 6 Hz at the magnitude 3.5. Incorporating the spectral ratios given in Table 11 upon the spectrum of the M3.5 earthquake then results in a stronger decrease of the corner frequency down to 0.7 Hz at M5.5. The seismic moments corresponding to the magnitudes shown in Fig. 4.18 are consistent with the data of Ishida (1974) and agree also well with the seismic moment-magnitude relationship proposed by Thatcher and Hanks (1973). The fault radii implied by the path of corner frequencies between the M3.5 and M5.5 earthquakes, however, are about 10 to 15 times smaller than those derived by Ishida (1974) for events of magnitudes 4.2 to 5 in the Kii peninsula. As suggested by the uncorrected spectrum in Fig. 4.14b, the choice of a higher value for Q_β could significantly lower the corner frequency of the reference earthquake used to construct our scaling law, thereby shifting to the left the loci of corner frequencies shown in Fig. 4.18 and leading to larger source dimensions. On the the other hand, it is also possible that Ishida's fault length estimates, which are based on a measure of the frequency at the first minimum in amplitude of the earthquake source spectrum, may reflect spectral holes due to multipathing rather than source effects. Her other estimations of fault sizes from the spatial distribution of aftershocks may again overestimate the fault areas by a factor of 3 to 5

(Aki, 1968). The lack of spectral resolution of the data available to us for the determination of the absolute spectrum at Oishiyama and the lack of attenuation data in the area, unfortunately, prevent a more definite answer to this discrepancy.

4.4 Discussion

Several studies of earthquake source spectra have been made in the Bear valley region of California during the past few years. A comparison of the scaling law obtained at Stone Canyon with the results of some of these studies is shown in Fig. 4.19. Johnson and McEvilly (1974) made a careful analysis of the source characteristics of 13 earthquakes recorded on broad-band (0.03 to 10 Hz) instruments at two sites of the San Andreas Geophysical Observatory, SAGO-Central and SAGO-East, stradling the San Andreas fault some 8 km south of Hollister. Eight of these events, with magnitudes ranging from 2.4 to 5.1, share a common source region with the earthquakes recorded at Stone Canyon. Their corner frequencies derived by Johnson and McEvilly from whole-record spectra as well as from synthetic seismograms studied both in the time and frequency domains are shown in Fig. 4.19 for each of the components available at the two stations. The numbers attached to these events refer to the data listed in Tables 1 and 2 of their paper. The moments at SAGO-East have been divided by a factor of 3, so the plot can

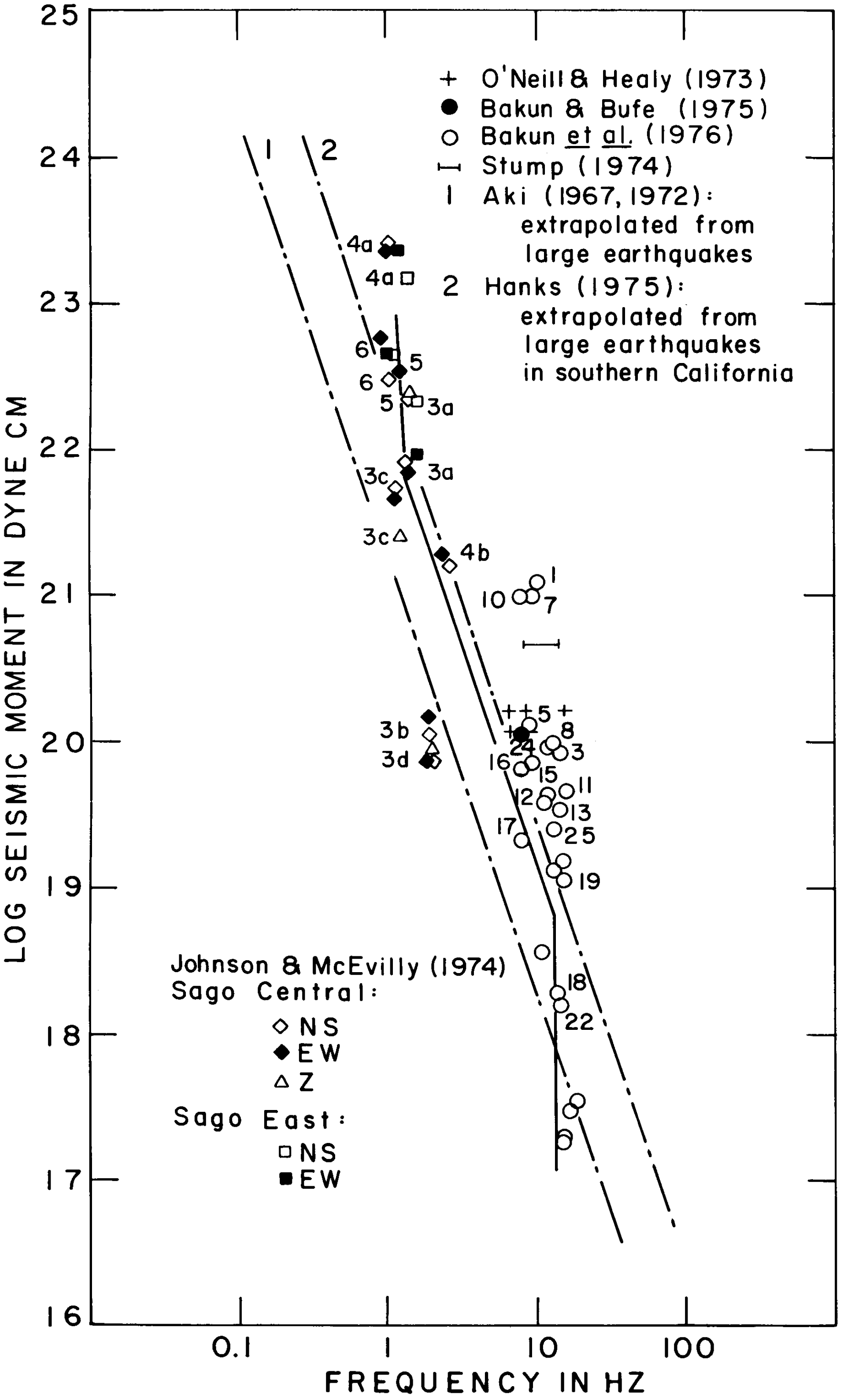

Fig. 4.19. Comparison of the scaling law obtained at Stone Canyon with the corner frequencies derived from various studies in the same area. The loci of corner frequencies extrapolated from Hanks' data in southern California and from Aki's original ω^2-model are also indicated.

be considered appropriate for bedrock southwest of the San Andreas fault. In constructing the plot, we have also assumed that the drop-off in the level of the source spectrum at the corner frequency is identical to that shown by the spectra plotted in Fig. 4.15. To the exception of the two smaller earthquakes 3b and 3d the agreement with our scaling law is excellent.

Another set of 20 earthquakes near Stone Canyon, which includes events 3b and 3d above, was studied by O'Neill and Healy (1973). The magnitude range covered in this case is from $M_L = 0.9$ to $M_L = 4.1$. Using a simple model of earthquake source, O'Neill and Healy estimated the source radii of these events from measurements of the pulse width of the P wave, corrected for Q and instrument response. From the source radius and the local magnitude estimated from the signal duration, they also determined the stress drop. Their results summarized in Fig. 14 of their paper, are consistent with our data, showing a trend of constant fault dimension for events with magnitudes between 1 and 2, followed by events with a roughly constant stress drop from magnitude 2 up to magnitude 4. Using the relation between corner frequency and source radius given in O'Neill and Healy's source model, we now obtain another set of estimates of the corner frequency of P wave spectrum for events 3b and 3d. These corner frequencies determined at three different stations of the U.S. Geological Survey (see Table 2 and Fig. 8 of their paper) are plotted in Fig. 4.19. They are about 4 to 10 times larger than those estimated by Johnson and McEvilly. Our own data at these magnitudes gives an intermediate result.

Also shown in Fig. 4.19 are the corner frequencies determined by Bakun et al. (1976) for SH spectra of 26 earthquakes on the San Andreas fault together with the single data point from Bakun and Bufe (1975) and the estimate of Stump (1974). As for the other data shown in this figure, the spectral level at the corner frequency was obtained from the value of the moment by assuming a drop-off identical to that shown by the spectra of Fig. 4.15. In their determination of source characteristics, Bakun and Bufe, and later Bakun et al. used the spectral ratio from two events of different sizes but with nearly identical source locations to estimate a propagation-path correction which they then applied to the observed spectra of the other earthquakes in the same region. The earthquakes which were also used in our analysis of the coda (Table 2) are marked by numbers in Fig. 4.19 according to the data in Table 1 of Bakun et al. (1976). The agreement with our scaling law is good for the smaller earthquakes but gets worse as magnitude increases. There is also a marked difference between this data and the corner frequencies obtained by Johnson and

McEvilly in the magnitude range from 2.5 to 4. Bakun et al. used a rectangular (boxcar) time window of 2.2 sec length to obtain the SH signal from which they computed the spectrum after correction for instrument response. The earthquake source spectrum was then derived by applying a total path Q_β of 100-150 to this result. It is possible that their time window includes a significant amount of scattered waves which cannot be characterized by a single Q_β. In Fig. 5.3 we show the apparent Q of coda derived for the same earthquakes. While the Q of coda waves at 1.5 Hz is about 130, consistent with the Q_β determined by Bakun et al., the Q required to explain the coda at 13.5 Hz is of the order of 750. This observation is related to a combined effect of variation of Q with depth and frequency-dependent composition of scattered waves as described in Chapter 5. The high corner frequencies derived by Bakun et al. could thus be due entirely to an overcorrection of the Q effect at high frequencies.

Interestingly, our scaling law at Stone Canyon is quite different from the scaling law obtained at the same station by Aki and Chouet (1975). Their data differs from ours mainly in the small earthquakes where it shows a constant stress drop path in the magnitude range from 1 to 3. Let us then compare the first 36 events of Table 1, which are used in both studies, with the remaining 149 earthquakes of this Table, used only in the present scaling law. The source factors of coda for the two data sets are shown in Figs. 4.20 and 4.21, and the relative growths of these coda amplitudes with magnitude are displayed in Figs. 4.22 and 4.23 for a few frequencies. In both of the latter figures the magnitude range covered is from 1, at the lower left of each plot depicted, to roughly 3 at the upper right of these plots. Close scrutiny of these figures shows that the spectral densities are the same for earthquakes of magnitude 1 but differ noticeably as magnitude increases beyond 1. The scaling laws displayed in Fig. 4.23 are identical to those shown in Fig. 4.7 with slightly less scatter due to the removal of the first 36 events. The slopes of the lines drawn in Fig. 4.22, however, are gentler than 1, as required by the scaling law proposed by Aki and Chouet. This discrepancy in the spectral densities between magnitudes 1 and 3 does not seem to be related to a change in the source location of earthquakes. In both data sets the median focal depth remains at 5.6 km and the epicenters are all within the same area (Fig. 4.24). On the other hand, the apparent Q of coda is found to be different between the two periods. At each channel filter frequency, the Q of the first 36 events is about 1.5 times higher than the Q derived for the later events (see Figs. 5.3 and 5.4). As shown in Fig. 4.25 for two earthquakes of the same magnitude and sharing the same source region, the difference in coda excitation responsible for this change in the apparent Q is quite pronounced at 24 Hz and noticeable also at 12 Hz. To determine whether this temporal variation in the coda character is related to a source or a

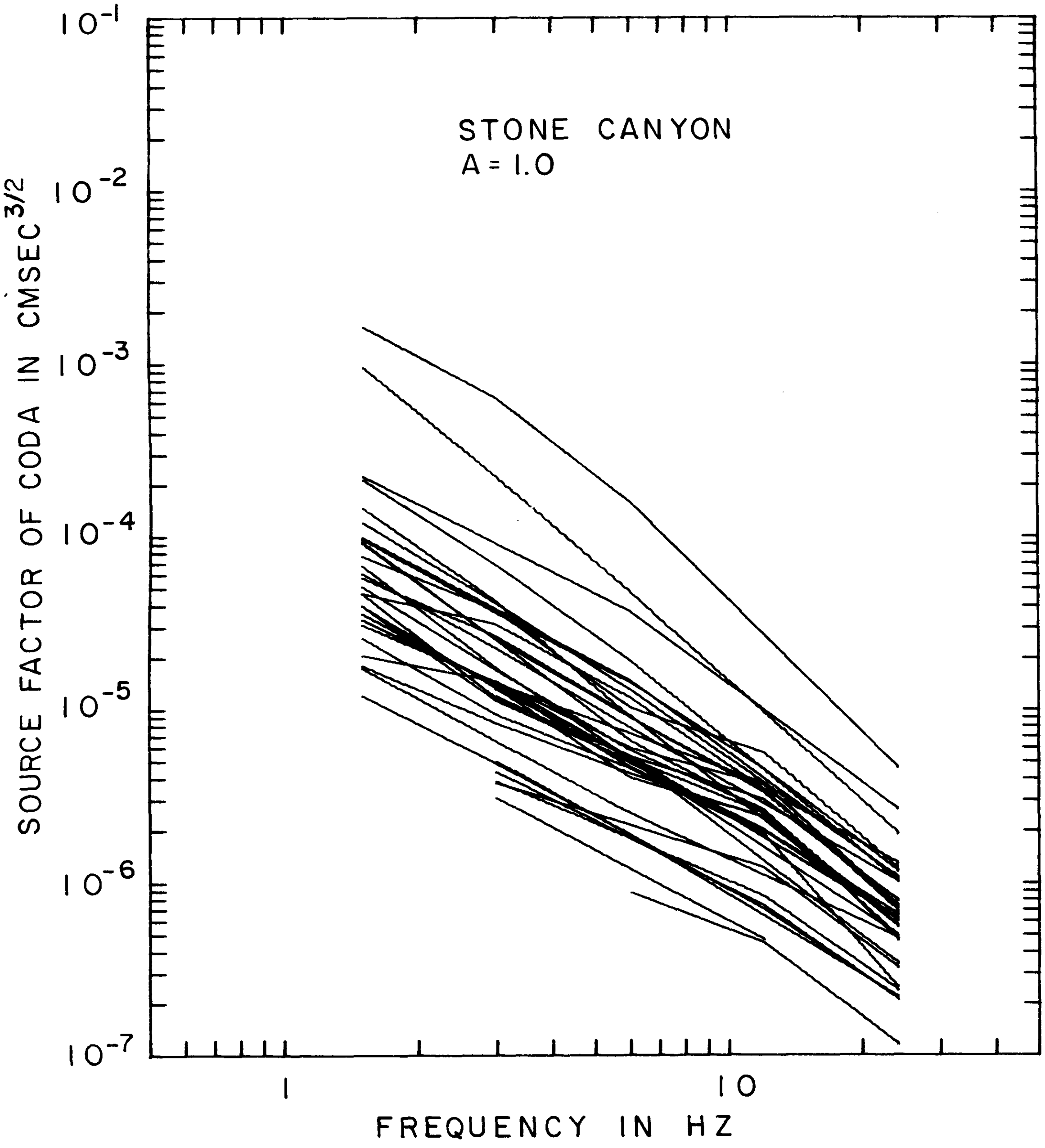

Fig. 4.20. Source factors of coda in the range of 1.5 to 24 Hz for the first 36 events recorded at Stone Canyon (see Table 1).

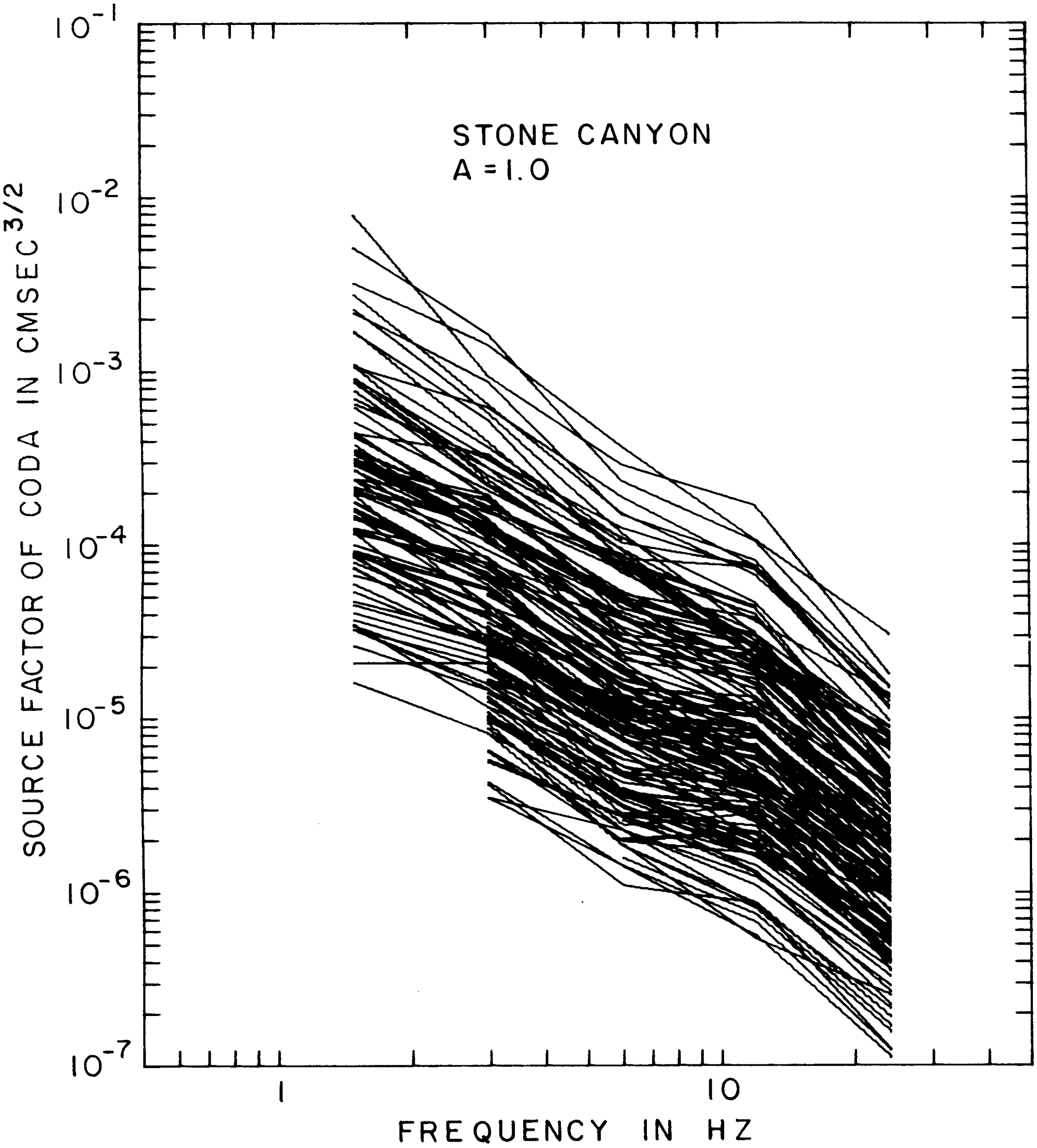

Fig. 4.21. Source factors of coda in the range of 1.5 to 24 Hz for the last 149 events recorded at Stone Canyon (see Table 1).

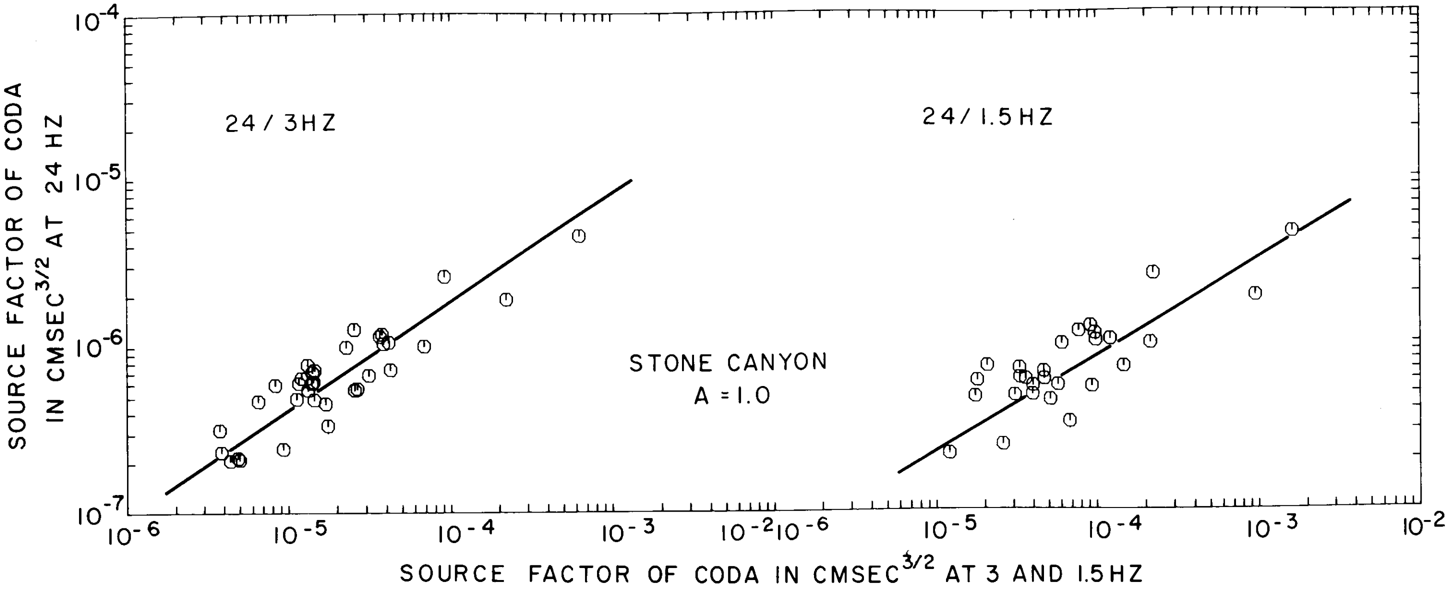

Fig. 4.22. Relations between the source factors of coda at 24 Hz and the source factors at 1.5 and 3 Hz for the first 36 events recorded at Stone Canyon. The rate of increase of the spectral densities with magnitude is slower at 24 Hz than at the lower frequencies.

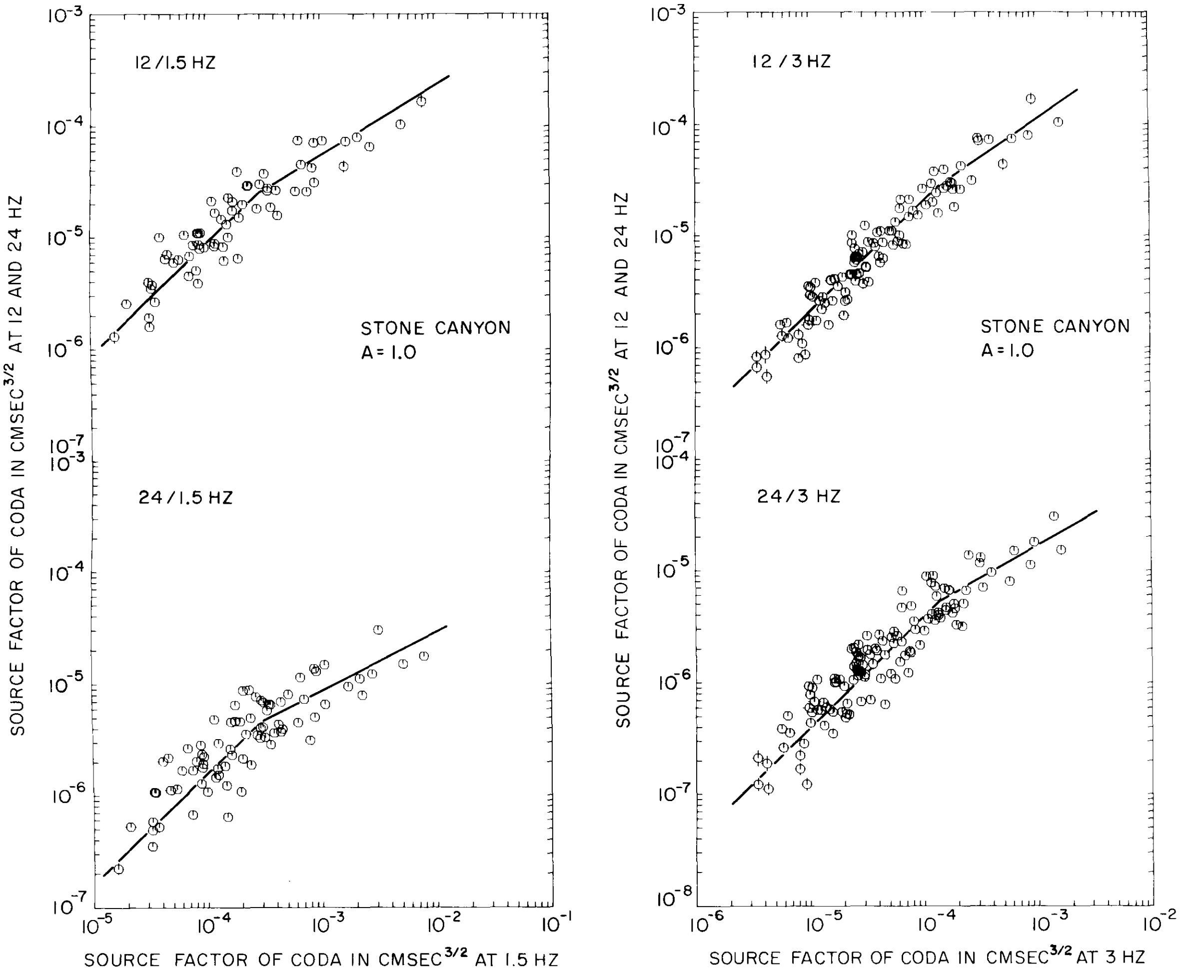

Fig. 4.23. Relations between the coda source factors at 12 and 24 Hz and the coda source factors at 1.5 or 3 Hz for the last 149 events recorded at Stone Canyon (see caption of Figure 4.7).

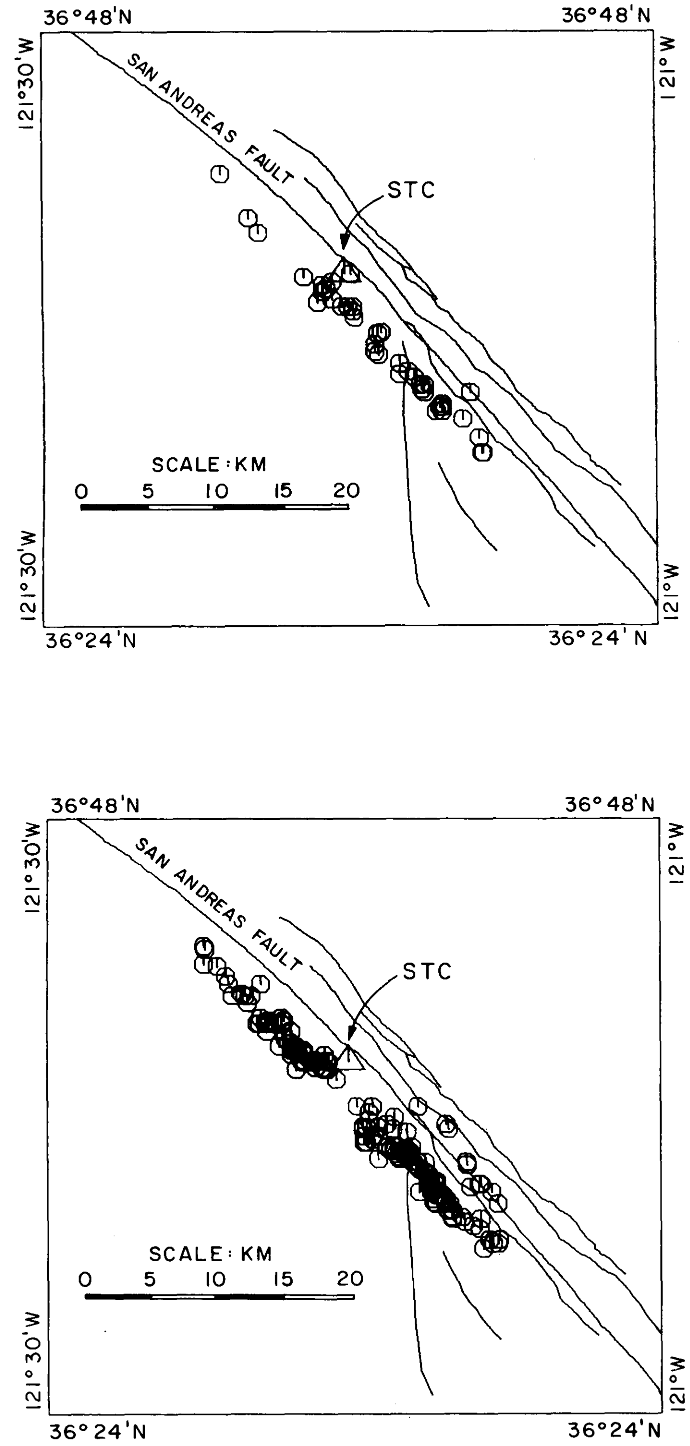

Fig. 4.24. Comparison between epicenters of the first 36 events (top) and remaining 149 events (bottom) recorded at Stone Canyon (STC). The median depth of focus is 5.6 km for both data sets (see also Table 1 and Figure 3.4).

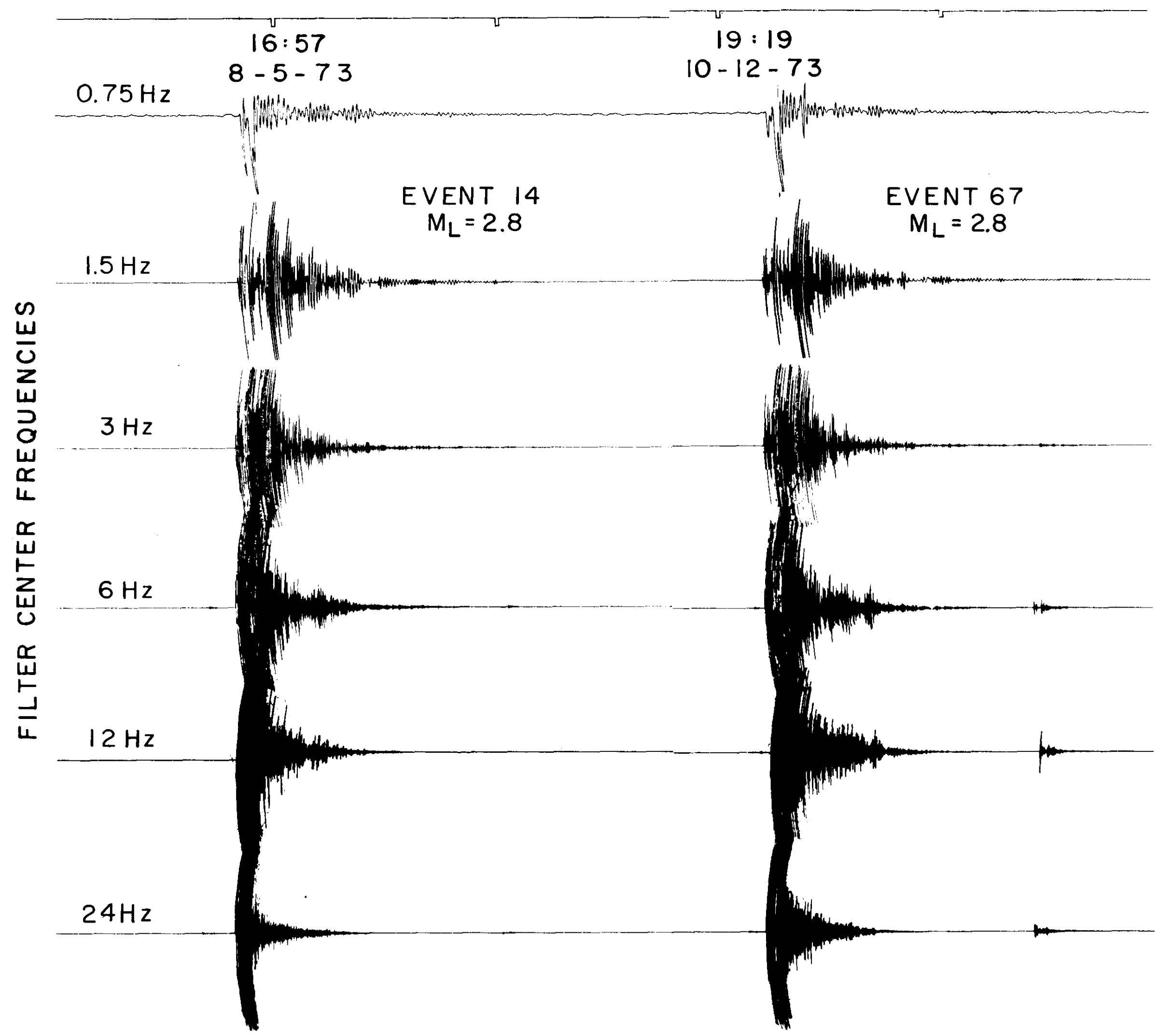

Fig. 4.25. Filtered traces of two events of magnitude 2.8 recorded at Stone Canyon in August and October 1973. The distance separating the two sources is 1.7 km. The hypocentral distance of event 14 is 12.1 km and that of event 67 is 13.4 km (see also Table 1). The difference in coda excitation for these two earthquakes, which share the same source region and have the same total duration, is quite pronounced at 24 Hz and noticeable at 12 Hz.

path effect, or both, we use Fig. 4.26. This figure shows the amplitude decay traces for the 24 Hz coda of the 185 earthquakes recorded at Stone Canyon. The first 36 events are depicted in Fig. 4.26a and the last 149 events in Figs. 4.26b, c, and d. The calibration traces $ct^{-1}(-24\pi t/Q)$ determined by the least squares method (Table 8b) for the four separate series of earthquakes are shown by the heavy curves drawn below the coda data in these plots. To the exception of events 39, 40, 44, 47, 50, 58 in Fig. 4.26b, event 96 in Fig. 4.26c, and events 139, 151 and 181 in Fig. 4.26d, which all show an anomalously steep amplitude decay, the parallelism between coda traces and their respective calibration curve in these last three plots is reasonably good. Of the 10 anomalous earthquakes only 2 have a measured coda trace at the frequency of 1.5 Hz and 9 have a corresponding trace available at 3 Hz. Disregarding these events thus removes two data points in the 24/1.5 Hz plot shown in Fig. 4.23, one of which is the lowermost point in that scaling, the other having the coordinates $6.42 \cdot 10^{-7}$ cmsec$^{3/2}$ and $1.46 \cdot 10^{-4}$ cmsec$^{3/2}$ at 24 and 1.5 Hz, respectively. Similarly, 9 data points are removed from the 24/3 Hz plot in that same figure, 4 of which are the leftmost points in that plot, the other 5 being distributed throughout the lower section of the plot with slope unity. It is clear then that the inclusion or exclusion of these peculiar small earthquakes does not affect the trend shown by the source factors plotted in Fig. 4.23 or the

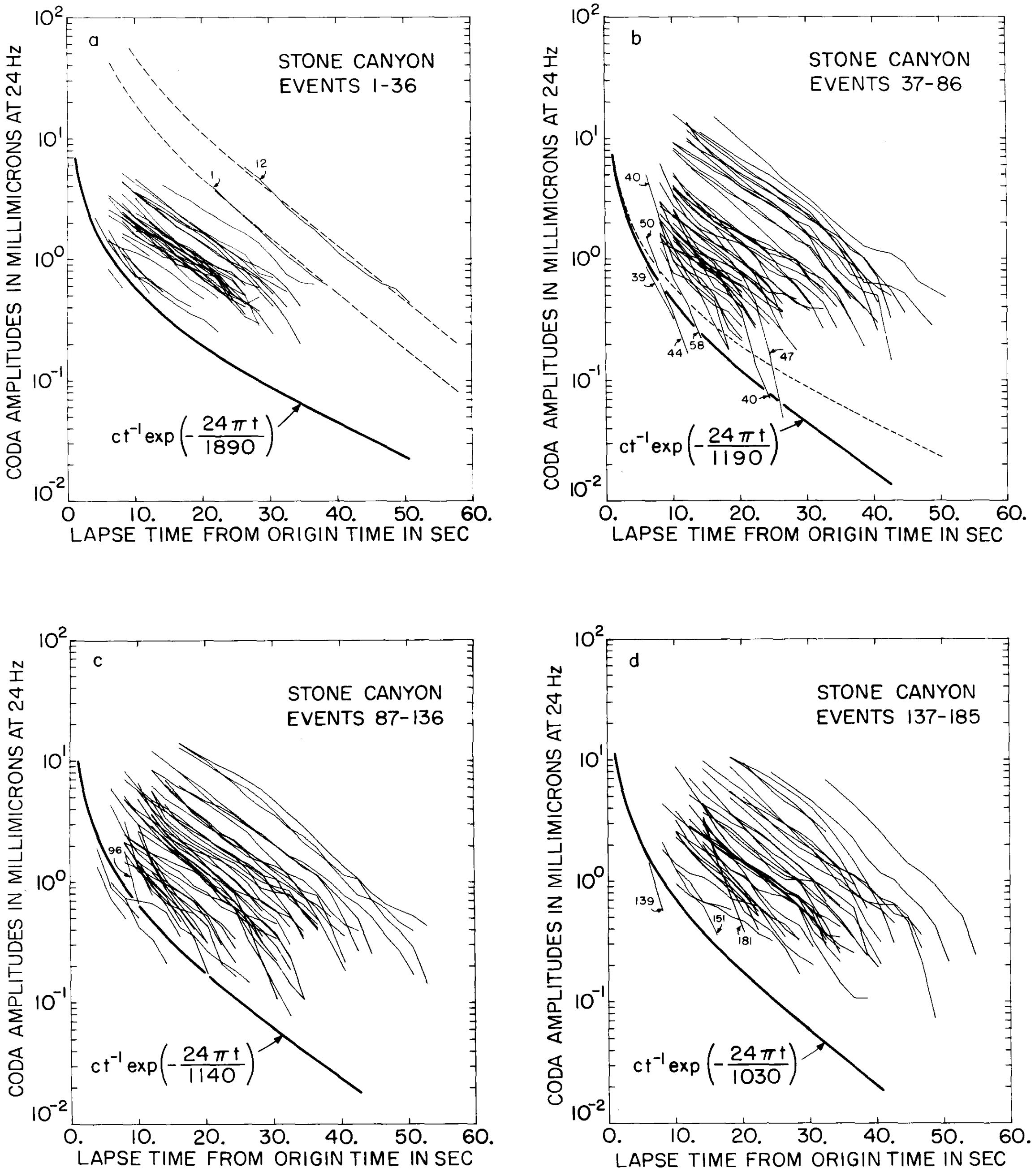

Fig. 4.26. Amplitude decay traces of the 24 Hz coda for the 185 earthquakes recorded at Stone Canyon. The calibration traces $ct^{-1}\exp(-24\pi t/Q)$ determined by the least squares method for the individual subsets of data are shown by the heavy curves in the four plots. The dashed curves in plot a indicate that the largest two events of this series of earthquakes share the same propagation path correction as the events shown in plot d. The dashed curve in plot b reproduces the calibration trace for plot a.

scaling law proposed in Fig. 4.15.

Figure 4.26a also shows a good parallelism between most events and the calibration curve $ct^{-1}\exp(-24\pi t/1890)$. The biggest two events of this group, events 1 and 12, however, do not fit the calibration curve. Rather, they are consistent with the calibration curve for later periods such as $ct^{-1}\exp(-24\pi t/1030)$, as indicated by the dashed traces in Fig. 4.26a. The effect of using the unduly higher Q value to correct for the propagation path effect for these two earthquakes is to lower the estimates of their source factors. Let us, for example, consider event 12 which, with a source factor of $4.59 \cdot 10^{-6}$ cmsec$^{3/2}$ at 24 Hz, is the largest event shown in Fig. 4.22, and also displays the largest discrepancy with the scaling law proposed in Fig. 4.23. The amplitude of the dashed calibration trace attached to this earthquake is 3.75 millimicrons at $t = 30$ sec. Thus we have $(c/30)\exp(-720\pi/1030) = 3.75 \cdot 10^{-7}$cm, from which we determine $c = 1.01 \cdot 10^{-4}$cmsec and $(S(\omega))^{1/2} = c/\sqrt{2\Delta f} = 1.79 \cdot 10^{-5}$cmsec$^{3/2}$. A similar correction made at 3 Hz gives $(S(\omega))^{1/2} = 2.13 \cdot 10^{-3}$ cmsec$^{3/2}$. Plotting these new coordinates in the 24/3 Hz scaling of Fig. 4.23 shows that indeed this earthquake is consistent with our new scaling law rather than with the original one depicted in Fig. 4.22. The same is also true of event 1 after correction.

Let us now return to Fig. 4.26. First we remove the 10 anomalous earthquakes mentionned earlier from Figs. 4.26b, c, d and relocate the two largest earthquakes shown in Fig. 4.26a with the set of events displayed in Fig. 4.26d. The coda traces of each separate data set are now all reasonably parallel to their respective calibration curve, so that a standard propagation path correction is applicable within each subset. The changing shape of the calibration curve with time, which is particularly well marked between Figs. 4.26a and 4.26b (compare the dashed calibration trace with the heavy trace in Fig. 4.26b) indicates that the propagation path correction has changed, that is the medium characteristics have changed with time. The fact that the two largest events in Fig. 4.26a fit the calibration trace for later periods furthermore suggests that this change in the medium structure affected only earthquakes of smaller magnitudes. These smaller and closer events have shorter durations and naturally sample less of the medium than the larger events with longer durations. It is probable then, that this temporal change in the medium characteristics is local to the site near Stone Canyon. In section 5.4, we shall qualitatively show that an increase in the energy content of the 24 Hz coda can be obtained without altering the signal duration by increasing the intrinsic Q associated with a low velocity layer in the crust under Stone Canyon or alternatively, but less likely, by increasing the turbidity throughout the crust.

Along with the local change in the crustal structure under Stone Canyon, it is also possible that the source characteristics of small earthquakes may have changed slightly. We have demonstrated above that events 1 and 12 actually belong to our new scaling law. This means that for magnitudes above 3 the scaling law shown in Fig. 4.15 remains unchanged. After repositioning the two largest events in the two plots of Fig. 4.22, however, we find that to fit all the source factors shown in these plots we have to curve upward the present lines drawn through the data. The first section of the new curve has the same slope and position as the original line in each of the depicted plots. The second section of this curve has a slope unity and fits the larger events that we have just corrected. The change in the slope of the curve occurs at about magnitude 2.5, that is roughly at the level of 10^{-6}cmsec$^{3/2}$ at 24 Hz for both plots. The slope less than unity for the events of magnitude smaller than 2.5 in Fig. 4.22 is suggested by the data in Fig. 4.26. Disregarding events 1 and 12 in Fig. 4.26a and comparing the traces of the remaining events with those of similar earthquakes in Fig. 4.26c for example, we notice that the vertical extent of the ensemble of traces is larger in the latter figure than in the former. Since the magnitude range of these events is roughly the same, we expect the rate of increase of the source factors derived from the small events in Fig. 4.26a to be slower at 24 Hz than that of the same events shown in Fig. 4.26c. This difference is visible in Figs. 4.22 and 4.23. Projected into the scaling law depicted in Fig. 4.15, the corrected data from Fig. 4.22 will lead to a slightly different path of the corner frequency below M3, reflecting a constant fault area from M3 down to M2.5 and a constant stress drop from M2.5 down to M1.5 where it meets the path shown in Fig. 4.15. Although the number of earthquakes in Fig. 4.22 is probably not sufficient to allow a definite conclusion on that point, this temporal change in the scaling law of the earthquake source spectra between M1.5 and M3 would increase the corner frequency of the M2.5 earthquake by a factor of 1.7 to the present position shown in Fig. 4.15. The stress drop for the same event would correspondingly increase from 10 bars to 45 bars. This change is small in view of variation in stress drop of individual earthquakes. In fact, as shown in Figs. 4.7 and 4.23, the difference observed at 24 Hz in the relative growths of the source factors with magnitude would not have been discovered if we had not constructed a scaling law from early data separately. The data from Bickmore Canyon, which was collected 7 months before the beginning of our experiment at Stone Canyon, unfortunately does not have the frequency range required for a comparison with our own data of the coda characteristics at 24 Hz where the effect of the change in crustal structure is most important.

While interesting the sensitivity of the high frequency coda to changes in the medium characteristics suggests that caution should be exercised in using coda waves to derive the scaling law of earthquake source spectrum. Plots of the coda traces for each individual data set are necessary to ascertain that a standard propagation path correction is applicable to the events under study. In some special cases as for the 10 anomalous events encountered in Fig. 4.26, the assumption of statistical homogeneity underlying our scattering models may not be adequate. No temporal change was discovered in the coda recorded at the other stations that we considered in the present study.

Let us now turn our attention to the various scaling laws derived for different regions and discuss some of their implications. Our results are summarized in Fig. 4.27, where the locus of corner frequency versus seismic moment is drawn for earthquakes in the San Andreas rift zone, near San Fernando, Kilauea, and at Oishiyama. The locus for the central U.S. earthquakes obtained by Street et al. (1975) is also included for comparison. The extrapolation of the loci obtained from large earthquakes by Aki (1967, 1972b) and Hanks (1975) are shown as references.

For most of the areas studied, the locus of corner frequency follows a zig-zag path consisting of segments of two distinct types. One is the vertical path of constant corner frequency and the other is parallel to the extrapolation from the loci for large earthquakes. The latter path, with the slope of -3 implies a constant stress drop independent of earth-

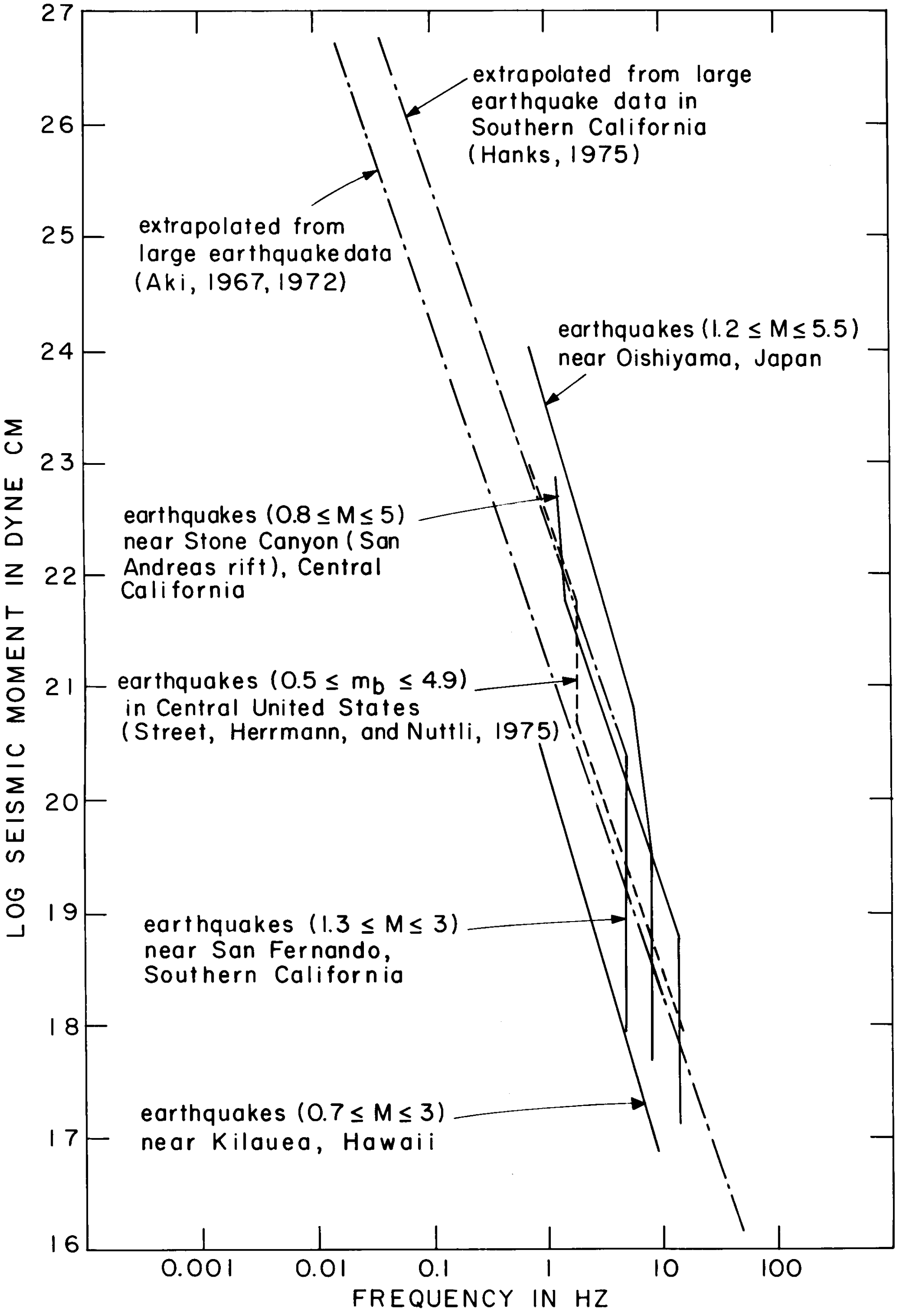

Fig. 4.27. Loci of the corner frequency as a function of seismic moment showing the characteristic paths for earthquakes of magnitude less than 5 in different regions.

quake magnitude.

The tendency to follow the constant stress drop path is understandable because the rupture strength of rocks is more or less a material constant. On the other hand, the path along the line of constant corner frequency implies a constant fault area independent of earthquake magnitude. The stress drop increases with magnitude along that path. Such a path is again understandable if there is a unique length characterizing the heterogeneity of the earth's crust in the area. A certain size of rupture area may be preferred because of the spatial distribution of stress and strength determined by the characteristic length of heterogeneity of the mechanical properties of the earth's crust. This path, however, cannot be kept indefinitely with increasing magnitude because the stress drop cannot increase indefinitely. A transition to constant stress drop earthquakes must eventually follow. In central United States or on the San Andreas fault in central California, multiple transitions between these two basic behaviors are suggested in the scaling laws which in turn suggest a multiplicity of inhomogeneity lengths affecting the earthquake fault size.

To make a more quantitative interpretation of the corner frequency loci, we shall now use the result of Madariaga (1976), who calculated the far field seismic spectrum from a circular crack which grows from a point, propagates with sub-shear velocity and stops at a radius a.

According to Madariaga, for a circular crack model the corner frequency f_o for S wave spectrum is related to the radius a by

$$a = \frac{0.21\beta}{f_o} \qquad (4.4)$$

where β is the shear velocity. For the circular crack, Eshelby (1957) and Keilis-Borok (1959) also gives a relation between the seismic moment M_o and stress drop $\Delta\sigma$ (initial stress minus final frictional stress on the fault).

$$\Delta\sigma = \frac{7}{16}\frac{M_o}{a^3} \qquad (4.5)$$

It is worth noting here that the stress drops obtained from formula (4.5) using (4.4) will be about six times larger than those found using Brune's (1970, 1971) approximation.

For earthquakes in the San Andreas rift zone, the constant corner frequency path was observed from magnitude 1 to 2, and a weak dependence of corner frequency on magnitude was again observed in the magnitude range from 4 to 5. Assuming β = 3.5 km/sec, the first corner frequency at 13 Hz corresponds to a fault radius of roughly 60 m, and the trend observed between magnitude 4 and 5 implies radii in the range of 490 to 570 m. The path joining these two segments in Fig. 4.25 is characterized by a constant stress drop around 45 bars.

On the other hand, events with magnitudes between 1 and 3 have a constant fault radius of about 150 m at San Fernando (β = 3.5 km/sec), and about 70 m at Oishiyama (β = 2.7 km/sec). The paths of the corner frequencies extrapolated from Aki (1967, 1972b) and Hanks (1975) imply constant stress drops in the range of 10 to 100 bar. The earthquakes studied by Street *et al*. (1975) in central United States show a stress drop of about 10 bar for small earthquakes and 100 bar for the larger events. Assuming β = 3.5 km/sec (Street et al., 1975), the transition between the two constant stress drop paths for these earthquakes occurs at a constant fault radius of 400 m.

Interestingly enough, the scaling law obtained in the active volcanic area of Kilauea exhibits the familiar earthquake behavior with low stress drops of the order of 0.5 bar at magnitude 1 up to 2.5 bar at magnitude 3. At the other extreme of the stress drop range, the earthquakes at Oishiyama have stress drops around 1 kbar in the magnitude range from 3 to 5.

By extending a similar study of the scaling law to many seismic areas, and correlating the stress drop and characteristic fault radius with local geology, we may eventually discover a method of predicting strong motion in a given area from the small earthquake spectra on the basis of the geologic structure.

CHAPTER 5

Quantitative Discussion on the Origin of Coda Waves

5.1 Introduction

In the previous chapter we used the source factors of coda to determine the source spectra of small earthquakes. Since the source factor of coda expresses both the effect of earthquake source and scattering sources, it can also be used to derive some information about the nature of the heterogeneous medium. In this chapter, we shall apply the two extreme models of wave medium proposed in Chapter 2 to the results of Chapter 4 to make a quantitative analysis of the scattering properties of the earth's crust in the various regions studied. This interpretation will then be further examined in the light of the attenuation characteristics of coda waves to derive a coherent picture of the origin of these waves.

5.2 Regional turbidities

As seen in Chapter 2, a quantitative description of the random medium can be made through the use of the turbidity coefficient which describes the scattering power of this medium. Let us now apply the models of coda waves discussed earlier to the source factors of coda and earthquake spectra derived in Chapter 4 and see if the resultant model parameters are reasonable.

We shall first apply the single scattering theory to the earthquakes observed at Stone Canyon. The basic equation for the theory is (2.19),

$$P(\omega|t) = \frac{v}{2} g(\pi) |\phi_o(\omega|r)|^2 \qquad (2.19)$$

where r = vt/2.

To express surface waves we shall use the simplest case of Rayleigh waves in a half space due to a point strike slip source (Ben-Menahem, 1961),

$$\phi_o(\omega|r) = 0.125\ f(h)\dot{M}(\omega)\sin 2\theta/[\mu c_R(\lambda r)^{1/2}] \qquad (5.1)$$

where $\phi_o(\omega|r)$ is the Fourier transform of vertical displacement at a distance r, μ is the rigidity of the medium, c_R is the Rayleigh wave velocity, λ is the wavelength, θ is the azimuth from the fault strike, and f(h) is the factor due to focal depth. Poisson's ratio is assumed to be 0.25.

Putting the above equation into (2.19) and using equation (2.11) in which we first eliminate the attenuation effect and replace the exponent of t by the value 1 for surface waves, we find that the backward turbidity coefficient $g(\pi)$ can be written:

$$g(\pi) = 64\lambda \left[\frac{\mu c_R}{f(h)\sin 2\theta}\right]^2 \frac{S(\omega)}{[\dot{M}(\omega)]^2} \qquad (5.2)$$

Then the source factor of coda $(S(\omega))^{1/2}$ determined previously by constraining a to the value 0.5 in equation (3.6) should give the necessary information.

For an average earthquake with magnitude 3 at Stone Canyon, $\dot{M}(\omega)$ is 6×10^{20} dyne cm at 1.5 Hz (Fig. 4.15). From the coda source factor of the same earthquake, on the other hand, we find that $S(\omega)$ is 0.45×10^{-6} cm^{2}sec^2 at 1.5 Hz. For a rough estimation of $g(\pi)$ we shall assume that $\mu = 3 \times 10^{11}$ dyne/cm^2, $c_R = 3$ km/sec, $\lambda = 2$ km, and an average azimuth depth factor $f(h).\sin 2\theta \simeq 0.1$. Then the backward turbidity $g(\pi)$ is estimated as 1.3 km^{-1}. In other words, in order to explain the observed coda as backscattering Rayleigh waves, the fractional loss of energy by scattering within the unit azimuthal angle (1 rad) in the backward direction should be $0.65/\pi$ per 1-km travel distance.

The above value of the backward turbidity coefficient does not seem to be unreasonable when we consider the strong near-surface heterogeneity commonly shown in geology maps.

On the other hand, we have an independent check on the turbitidy coefficient if we assume body wave scattering for the origin of coda waves. As discussed earlier, the model of random medium under the Montana Lasa predicts very small backward turbidity coefficients (8×10^{-5} km^{-1} for $N(r) = e^{-r/a}$ and 2.5×10^{-12} km^{-1} or less for $N(r) = e^{-r^2/a^2}$) for P waves with frequencies higher than 0.5 Hz.

For primary shear waves we shall consider the simplest case of dislocation in an unbounded homogeneous medium (e.g., Maruyama, 1963),

$$\phi_o(\omega|r) = (0.4)^{1/2}(4\pi\rho\beta^3 r)^{-1}\dot{M}(\omega) \qquad (5.3)$$

where ρ is the density, β is the shear wave velocity and the factor $(0.4)^{1/2}$ stands for the RMS average over the spherical surface of the shear displacement radiation pattern

$$[\langle R^2_{\theta\phi}\rangle]^{1/2} = [\frac{1}{4\pi} \int_o^{2\pi} d\phi \int_o^{\pi} (\cos^2\theta\cos^2\phi + \cos^2 2\theta\sin^2\phi)\sin\theta d\theta]^{1/2}$$

$$= (0.4)^{1/2} \qquad (5.4)$$

where θ and ϕ are the standard polar coordinates (Haskell, 1964; Aki, 1967).

Putting equation (5.3) into (2.19) and using equation (2.11) in which we eliminate the attenuation effect and replace the exponent of t by the value 2 for body waves, we obtain the backward turbidity coefficient $g(\pi)$ as

$$g(\pi) = 20(\rho\pi)^2\beta^7 \frac{S(\omega)}{[\dot{M}(\omega)]^2} \qquad (5.5)$$

Then the source factor of coda $(S(\omega))^{1/2}$ determined previously by constraining a to the value 1 in equation (3.6) should give the necessary information. For an average earthquake with magnitude 3 and Stone Canyon, $S(\omega)$ is 7.24 x 10^{-6} cm^{2}sec^3 at 1.5 Hz. The corresponding value of $\dot{M}(\omega)$ is

6×10^{20} dyne cm as given before. For a rough estimate of the backward turbidity coefficient, we shall use $\rho = 2.7$ gr/cm^3 and $\beta = 3.5$ km/sec. Then we find $g(\pi)$ to be about 1.8 km^{-1}. A similar computation made for compressional waves, on the other hand, gives $g(\pi)$ as high as 15 km^{-1}. These backward turbidity coefficients are many orders of magnitude larger than the values estimated earlier from the parameters of the random medium model under Lasa. In other words, the heterogeneity of the lithosphere determined from the fluctuation of amplitude and phase spectra of teleseismic P waves at Lasa is not strong enough to account for the 1.5 Hz coda of local earthquakes as backscattering body waves.

In order to substantiate the above conclusion we shall apply the three-dimensional diffusion model corresponding to body wave scattering of the same earthquake. Using the basic equation (2.15) in which we replace equation (2.11) where the exponent of t is now set to the value 3/2 for the diffusion of body waves, we find the diffusivity D as

$$D = \frac{1}{4\pi(\rho\omega^2)^{2/3}} \left[\frac{W(\omega)}{S(\omega)}\right]^{2/3} \tag{5.6}$$

where the energy density $W(\omega)$ represents the total seismic energy within a unit frequency band around ω, and $S(\omega)$ is the square of the source factor of coda obtained by constraining a to the value 3/4 in equation (3.6). The total energy radiated, E, in a given signal can be expressed in terms of its spectral amplitudes (Wu, 1966) as

$$E \propto \frac{1}{2\pi} \int_{-\infty}^{\infty} |\Omega(\omega)\omega|^2 d\omega \qquad (5.7)$$

where $\Omega(\omega)$ represents the displacement amplitude spectral density of the signal. Similarly, for the band-passed signal within the band $\omega_o < |\omega| < \omega_1$, we obtain the fractional energy ΔE

$$\Delta E \propto \frac{1}{2\pi} \int_{-\omega_1}^{-\omega_o} |\Omega(\omega)\omega|^2 d\omega + \frac{1}{2\pi} \int_{\omega_o}^{\omega_1} |\Omega(\omega)\omega|^2 d\omega \qquad (5.8)$$

which we rewrite, using (5.7),

$$\Delta E = \frac{\int_{-\omega_1}^{-\omega_o} |\Omega(\omega)\omega|^2 d\omega + \int_{\omega_o}^{\omega_1} |\Omega(\omega)\omega|^2 d\omega}{\int_{-\infty}^{\infty} |\Omega(\omega)\omega|^2 d\omega} E \qquad (5.9)$$

To compute the fractional energy, we use the source spectrum as shown in Fig. 4.15, in which we approximate the spectral modulus by the frequency response of a Butterworth low-pass filter of the form

$$\Omega(f) = \Omega_o [1 + (\frac{f}{f_o})^4]^{-1/2} \qquad (5.10)$$

where Ω_o represents the displacement amplitude spectral density at $f = 0$, f is frequency, and f_o is the corner frequency. Replacing $\omega = 2\pi f$ in (5.9) and using (5.10), we obtain an integrand which is an even function of f and thus write:

$$\Delta E = \frac{\int_{f_o}^{f_1} \frac{f^2 df}{1 + (\frac{f}{f_o})^4}}{\int_{o}^{\infty} \frac{f^2 df}{1 + (\frac{f}{f_o})^4}} E \qquad (5.11)$$

Integrating the denominator by the method of residues then yields

$$\Delta E = (\frac{\pi f_o^3}{2\sqrt{2}})^{-1} E \int_{f_o}^{f_1} \frac{f^2 df}{1 + (\frac{f}{f_o})^4} \qquad (5.12)$$

The total seismic energy E is estimated by the Gutenberg-Richter formula $\log_{10}E = 11.8 + 1.5\ M$ with the assumption that the surface wave magnitude M which enters this expression can be replaced with reasonable accuracy by the local magnitude M_L for earthquakes with magnitudes around 3 (see original data of Gutenberg and Richter (1956, Figure 3)). For M3 earthquakes at Stone Canyon, the corner frequency f_o is at 4 Hz and the total energy E is about 2×10^{16} ergs. Then the fractional energy ΔE in the 1 Hz band around 1.5 Hz is estimated as 6.4×10^{14} ergs. This gives $W = \Delta E/\Delta f = 6.4 \times 10^{14}$ erg sec. On the other hand the value of $S(\omega)$ at 1.5 Hz is 1.8×10^{-6} cm^2 sec$^{5/2}$. Putting these values into (5.6) and using $\rho = 2.7$ gr/cm^3, we obtain $D = 10^{11}$ cm^2/sec. Then, using equation (2.22) and assuming a shear velocity of 3.5 km/sec, we find that the mean free path is 9 km or the turbidity coefficient is 0.1 km^{-1}.

For the body waves around 1.5 Hz in the random medium assumed under Lasa, most of the scattered energy is directed forward because of large ka (Aki, 1973). The parts of scattered energy for which the diffusion theory may be applicable are probably only those scattered in the backward direction. Therefore the turbidity coefficient obtained from diffusivity should be considered as a rough estimate of backward turbidity. The value obtained from the coda is again several orders of magnitude larger than that estimated for the random medium under Lasa. Thus we conclude that the heterogeneity of the lithosphere is not strongenough to explain the observed coda waves at around 1.5 Hz as backscattering body waves. They must be primarily backscattering surface waves, with the backward turbidity $g(\pi)$ of the order of 1.3 km^{-1}.

The same analysis was extended to higher frequencies as well as to other stations. The results for body wave scattering are summarized in Tables 12 and 13. The turbidities at Oishiyama were calculated using Fig. 4.18 on the assumption that the seismic moment of M3 earthquakes there has the same

TABLE 12. Source Factor of Coda and Seismic Moment for Earthquakes with Magnitude 3

Station	Frequency f, Hz	Source Factor of Coda $[s(\omega)]^{1/2}$, cmsec$^{3/2}$	Moment* $\dot{M}(\omega)$, dynecm	Turbidity $g(\pi)$, km^{-1}
Stone Canyon	1.5	2.69×10^{-3}	6.03×10^{20}	1.8
	3	9.83×10^{-4}	3.63×10^{20}	0.7
	6	2.38×10^{-4}	1.62×10^{20}	0.2
	12	1.04×10^{-4}	5.75×10^{19}	0.3
	24	2.06×10^{-5}	1.82×10^{19}	0.1
San Fernando	1.5	4.35×10^{-4}	6.31×10^{20}	0.05
	3	3.53×10^{-4}	3.98×10^{20}	0.08
	6	2.74×10^{-4}	2.04×10^{20}	0.2
	12	1.31×10^{-4}	7.94×10^{19}	0.3
	24	4.53×10^{-5}	2.63×10^{19}	0.3
Kilauea	1.5	7.46×10^{-4}	1.90×10^{20}	0.1
	3	6.13×10^{-4}	7.08×10^{19}	0.5
	6	2.51×10^{-4}	1.90×10^{19}	1.1
	12	3.50×10^{-5}	4.57×10^{18}	0.4
	24	1.17×10^{-5}	1.20×10^{18}	0.6
Oishiyama	1.5	3.15×10^{-4}	7.94×10^{20}	0.003
	3	1.27×10^{-4}	5.75×10^{20}	0.001
	6	1.24×10^{-4}	3.02×10^{20}	0.004
	12	5.12×10^{-5}	1.32×10^{20}	0.003

Interpretation by the single-scattering theory for body waves.
*More precisely, this is the spectral density of the time derivative of seismic moment.

TABLE 13. Source Factor of Coda and Seismic Energy for Earthquakes with Magnitude 3

Station	Frequency f, Hz	Source Factor of Coda $[s(\omega)]^{1/2}$, $cmsec^{5/4}$	Seismic Energy within the Band, erg	Diffusivity D, cm^2sec^{-1}	Mean Free Path, km	Turbidity, km^{-1}
Stone Canyon	1.5	1.34×10^{-3}	6.39×10^{14}	1.03×10^{11}	8.9	0.11
	3	5.06×10^{-4}	3.66×10^{15}	3.04×10^{11}	26.0	0.04
	6	1.31×10^{-4}	6.73×10^{15}	6.91×10^{11}	59.2	0.02
	12	6.11×10^{-5}	4.40×10^{15}	3.60×10^{11}	30.8	0.03
	24	1.24×10^{-5}	2.25×10^{15}	4.84×10^{11}	41.5	0.02
San Fernando	1.5	2.78×10^{-4}	3.33×10^{14}	5.34×10^{11}	45.8	0.02
	3	2.31×10^{-4}	2.26×10^{15}	6.12×10^{11}	52.5	0.02
	6	1.77×10^{-4}	6.43×10^{15}	4.38×10^{11}	37.6	0.03
	12	9.06×10^{-5}	5.33×10^{15}	2.36×10^{11}	20.2	0.05
	24	3.25×10^{-5}	2.81×10^{15}	1.51×10^{11}	13.0	0.08
Kilauea	1.5	3.57×10^{-4}	6.57×10^{15}	2.86×10^{12}	357.0	0.003
	3	3.19×10^{-4}	3.99×10^{15}	5.94×10^{11}	74.3	0.01
	6	1.43×10^{-4}	2.02×10^{15}	2.76×10^{11}	34.5	0.03
	12	2.04×10^{-5}	1.01×10^{15}	5.82×10^{11}	72.8	0.01
	24	7.59×10^{-6}	5.06×10^{14}	3.43×10^{11}	42.9	0.02
Oishiyama	1.5	1.58×10^{-4}	1.94×10^{14}	7.54×10^{11}	82.3	0.01
	3	6.88×10^{-5}	1.42×10^{15}	2.15×10^{12}	234.6	0.004
	6	6.89×10^{-5}	5.58×10^{15}	1.34×10^{12}	146.0	0.007
	12	2.96×10^{-5}	6.05×10^{15}	1.09×10^{12}	118.8	0.008

Interpretation by the diffusion theory.

value of 10^{21} dyne cm as for the other regions studied. For all the areas considered, the backward turbidity obtained from the coda at 1.5 Hz is at least 1 or 2 orders of magnitude larger than the value calculated for the body waves under Lasa. This is consistent with the above suggestion that the low-frequency coda waves are backscattering surface waves.

The medium under Stone Canyon becomes markedly more transparent with increasing frequency. On the other hand, the opposite tendency is found at San Fernando, where the medium is slightly more opaque to 24 Hz waves than to 1.5 Hz waves. While the backward turbidities at 24 Hz are roughly similar in these two regions, implying common medium characteristics at this frequency, the region of Stone Canyon is about one order of magnitude more turbid at low frequency than the region of San Fernando. In other words, shallow large-scale heterogeneities are comparatively stronger at Stone Canyon than at San Fernando. This high turbidity at shallow depth in the Bear Valley area appears to be compatible with strong lateral velocity fluctuations found in that region by Aki and Lee (1975). In Hawaii, the backward turbidity shows a tenfold increase in the range of 1.5 to 6 Hz, beyond which the medium becomes suddenly more transparent. The turbidity at Oishiyama is roughly constant throughout the observed frequency range with values lower than in the other regions considered.

5.3 Regional seismic attenuation properties of the earth's crust

We shall now turn to the factor b derived in Chapter 3 from equation (3.8). The least square estimates of this factor are given in Tables 8a, b, c for different regions and various choices of the parameter a. From these results, and using formula (3.9), we can calculate a value of the quality factor for each channel filter frequency. These estimates of Q thus represent an average value of the attenuation properties over the region encompassed by the coda waves from many different local earthquakes. In Figure 5.1 the values of Q^{-1} determined at Tsukuba, Japan, and San Fernando, California, are shown plotted against frequency for three choices of the spreading factor a. As we pointed out in Chapter 3, because of the particular form of (3.8), the uncertainty associated with the parameter a has very little effect on the result derived for Q. In both regions, Q increases with frequency independent of the choice of a. At Tsukuba, Q varies from 200-250 at 1 Hz to about 1800 at 24 Hz. On the other hand, the Q derived at San Fernando shows lower values increasing from 60-80 to roughly 600 within the same frequency range.

The quality factors obtained for the regions of Oishiyama, Tsukuba, San Fernando, Kilauea, and the Bear Valley area are summarized in Figures 5.2 and 5.3. In this analysis the factor a was fixed to 1. The Q of coda waves again shows consistently low values at 1.5 Hz and high values at 24 Hz. That Q is high at high frequency can be seen

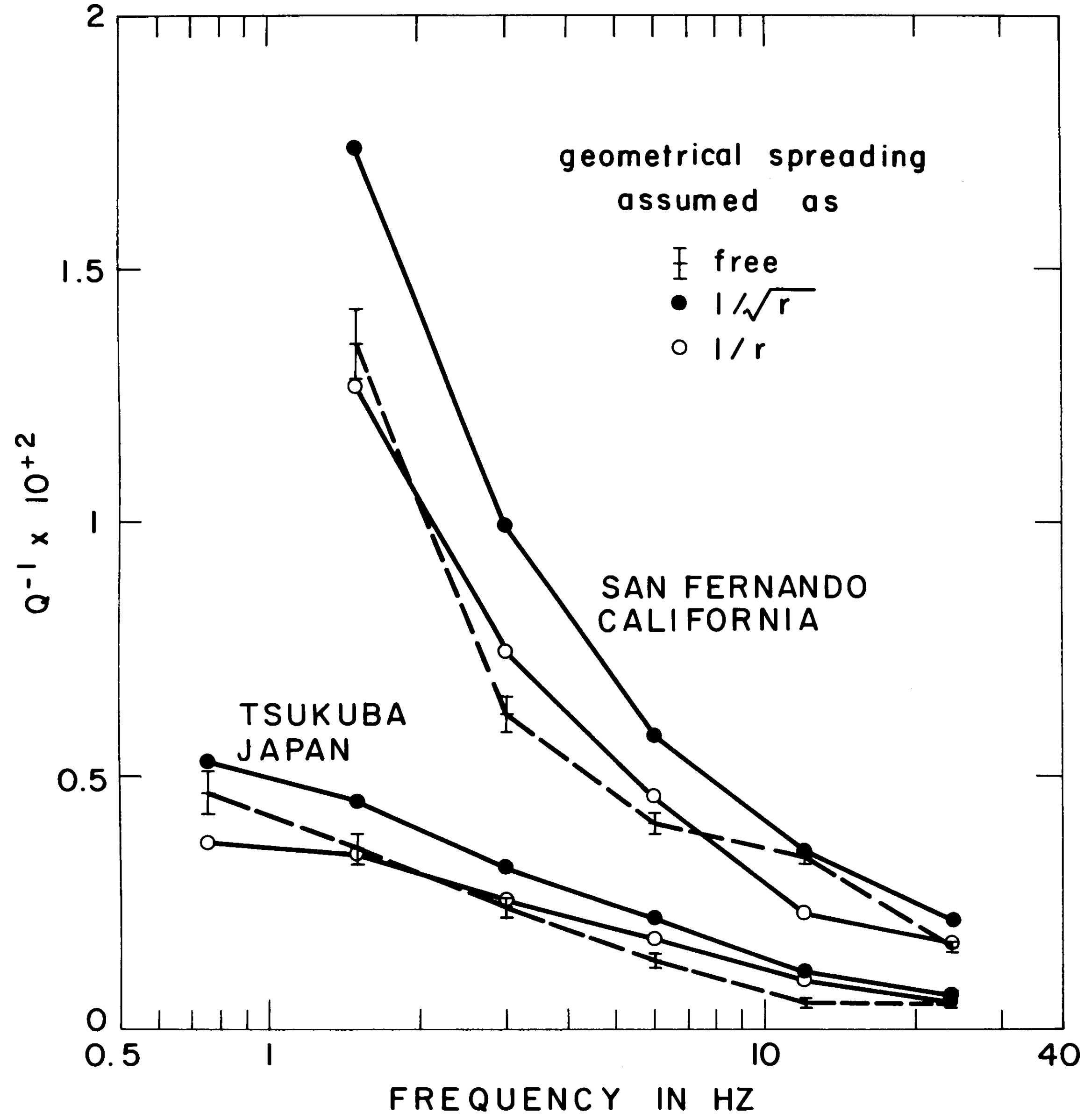

Fig. 5.1. Regional variations of Q^{-1} in the range 1-24 Hz derived from the analysis of earthquake coda at Tsukuba (bottom) and San Fernando (top), with different assumptions on the spreading mode of waves in the single-scatterer model. Open circles refer to the assumption of body wave scattering, and closed circles refer to the assumption of surface wave scattering. Crosses with error bars refer to no constraint on the mode. The values of Q^{-1} derived from the diffusion model would fall in between the values shown for surface wave and body wave assumptions.

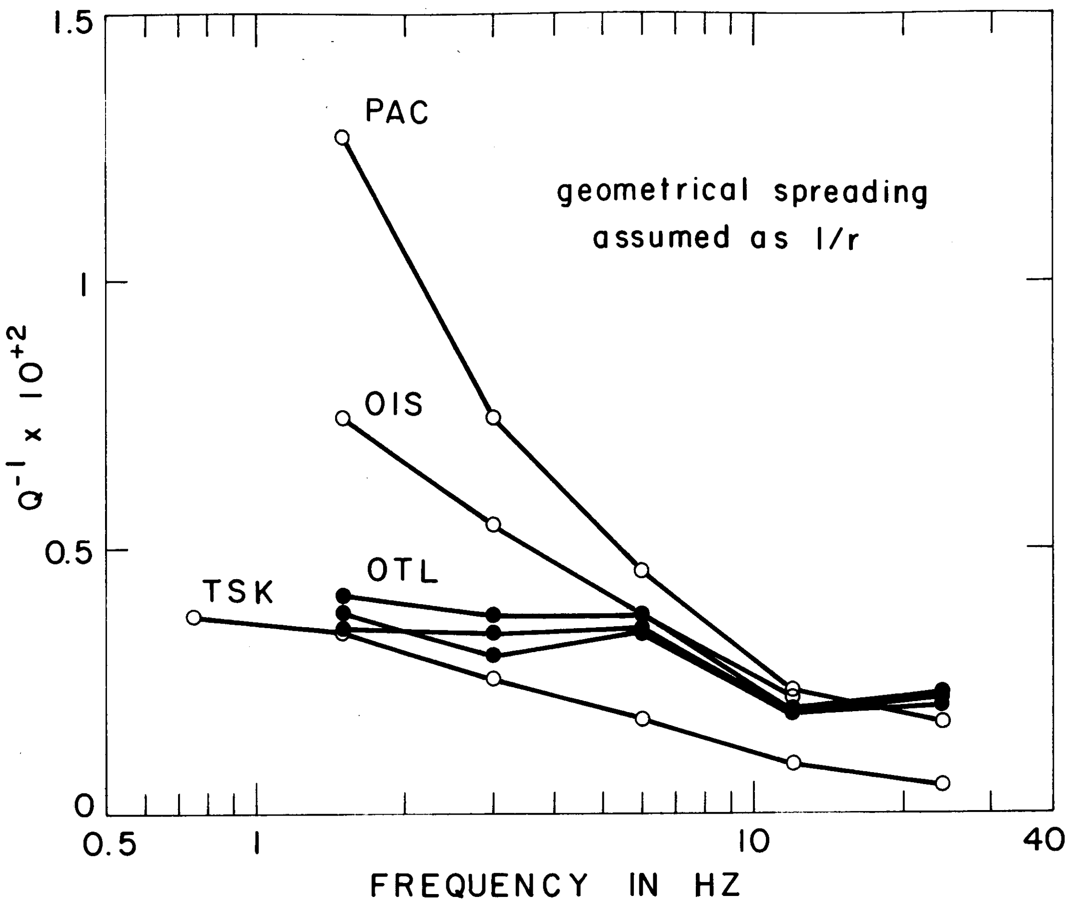

Fig. 5.2. Regional variations of Q^{-1} in the range 1-24 Hz derived from the analysis of earthquake coda at Tsukuba (TSK), Kilauea (OTL), Oishiyama (OIS) and San Fernando (PAC). The values shown were derived from the single-scatterer model assuming body wave scattering. The 3 curves shown for Kilauea result from the processing of 3 different data sets, each consisting of 37 earthquakes (see Table 8b).

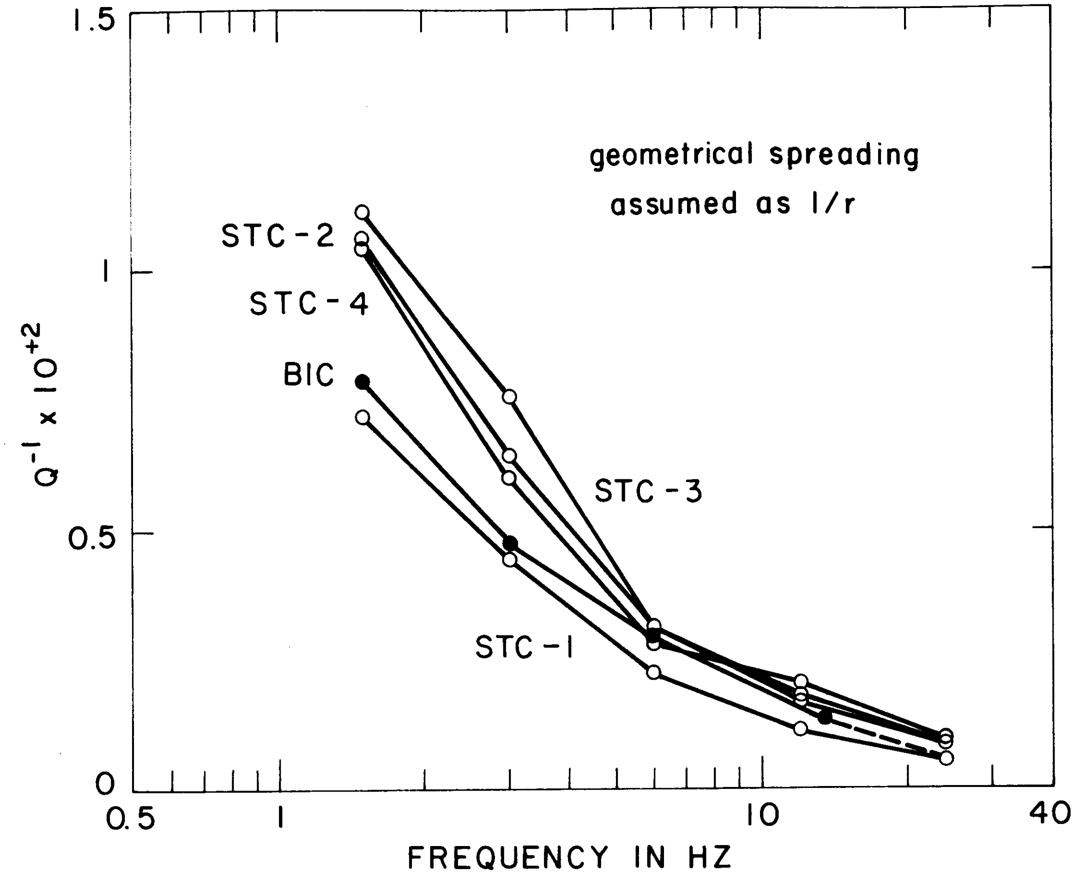

Fig. 5.3. Variations of Q^{-1} in the range 1-24 Hz derived from the analysis of earthquake coda at Stone Canyon (STC) and Bickmore Canyon (BIC). The values shown were derived from the single-scatterer model assuming body wave scattering. The 4 curves shown for Stone Canyon result from the processing of 4 different data sets consisting of 36, 50, 50, and 49 events, respectively. There is a marked difference between the values of Q^{-1} derived from the first data set at Stone Canyon compared to the values of Q^{-1} obtained from the last three data sets at the same station.

directly from the records. For example at Tsukuba, if the Q obtained at 1 Hz were to be applicable at 24 Hz also, one would expect the signal within the corresponding frequency band to die off in a matter of a few seconds. The fact that it can last for 100 sec or more at this frequency (Fig. 3.12) clearly indicates that the Q of coda waves must increase with frequency. This, however, does not necessarily mean that the Q of crustal material is frequency dependent, but rather that we may be observing the dependence of Q on depth for waves scattered from different parts of the earth's crust. In other words, this apparent frequency dependence can be explained if the coda waves at 1.5 Hz are primarily composed of surface waves scattered from shallow heterogeneities and those at 24 Hz are essentially backscattering body waves from the deeper, high-Q lithosphere. The turbidities found in the previous section support the above suggestion, because we showed that the low-frequency coda waves cannot be backscattering body waves. The observed high Q for high-frequency coda, on the other hand, eliminates the possibility that they are backscattering surface waves confined in the low-Q shallow depth. Thus they must be backscattering body waves from heterogeneities in the deep lithosphere.

The low values of Q obtained near 1 Hz are consistent with the Q determined by other workers using direct waves from explosions or shallow earthquakes (Clowes and Kanasewich, 1970; O'Neill and Healy, 1973; Kurita, 1975; Bakun and Bufe, 1975). For example, at Bickmore Canyon, the Q of coda waves from 18 local earthquakes is 130 at 1.5 Hz (Fig. 5.3), which agrees well with the Q_β of 100-150 found by Bakun et al. (1976) for S waves from the same shallow events. On the other hand, the high Q of 600-2000 derived at 24 Hz for most areas are consistent with the results reported by Clowes and Kanasewich (1970) for the lower crust and with the Q value of the lithosphere obtained from surface wave attenuation (Tsai and Aki, 1969).

The results obtained in California indicate a gradual change in the opacity and attenuation characteristics of the medium with increasing frequency. The change in the Q of coda observed in Japan also appears quite smooth. By comparison, the medium under Kilauea presents some interesting properties. At frequencies below 6 Hz, our results indicate that the waves are probably surface waves in a rather opaque medium with a constant Q of about 250 consistent with the Q_β required to correct the absolute spectra for the smallest and closest events. Above 6 Hz, however, the medium suddenly becomes more transparent and Q increases to a roughly constant level of 400-500. Thus, in Hawaii, Q is high in the shallow crust and low in the lower crust compared to California or Japan. This low Q in the deeper crust is not a local station effect because the direct P and S arrivals show a sharp impulsive character. Rather it may reflect porous lava sheets or the presence of magma under Kilauea.

Another interesting observation is made at Stone Canyon (Fig. 5.3) where a significant variation exists between the apparent Q obtained from the first 36 earthquakes recorded at STC (STC-1) and the apparent Q derived from subsequent data sets (STC-2, -3, and -4). As shown in Figures 4.25 and 5.4, this temporal variation is particularly well marked at high frequency during the first 100 days of recording at this station. Fits made with two different size distributions of the data space available indicate that the strongest variation occurs roughly 70 days after the beginning of the operation at STC. Let us now see how this variation is related to a change in the medium properties under the Stone Canyon area.

5.4 Temporal variation in the crustal structure near Stone Canyon

We have seen in section 4.4 that the temporal change observed in the high frequency coda recorded at Stone Canyon is primarily related to a path effect. The records of the two earthquakes shown in Fig. 4.25 indicate that for events of the same duration, the change in coda character at 24 Hz affects mostly the intermediate portion of the seismograms while the beginning as well as the end of the traces seem to share common amplitudes. The variation appears as an increase in the energy content of the coda as seen for example in event

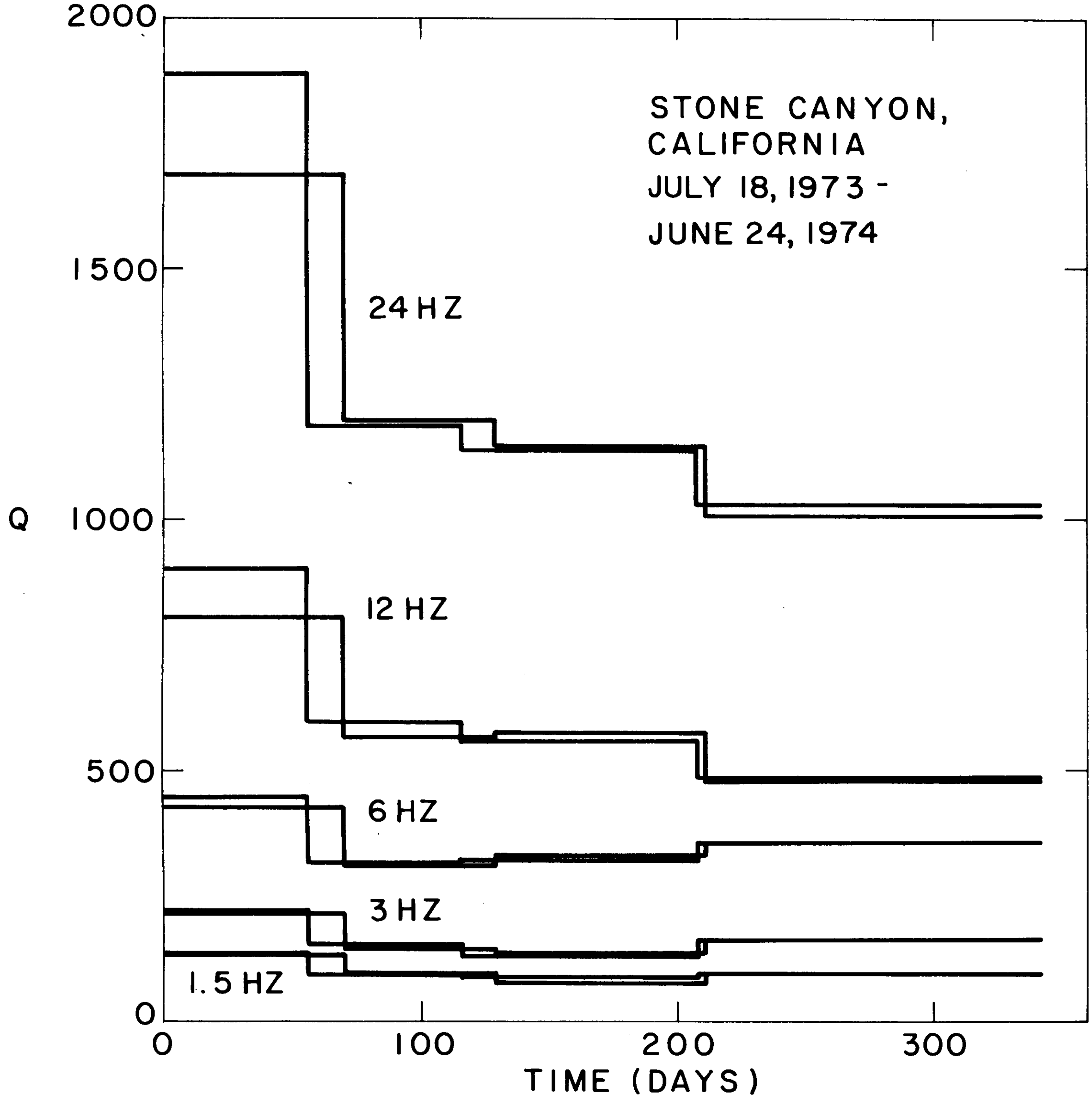

Fig. 5.4. Temporal variation of the apparent Q of coda waves observed at Stone Canyon during a period of 342 days. The two curves shown for each channel filter frequency represent the results of fitting data sets consisting of 36, 50, 50 and 49 events, and 47, 46, 46, and 46 events, respectively (see Table 8b). The strongest variation is observed roughly 70 days after the beginning of the operation at STC.

67 compared to event 14 (Fig. 4.25) which suggests that the intrinsic Q or possibly the turbidity may have increased in the crust under Stone Canyon. In an attempt to explain this observation we shall use a three-dimensional block-model of the wave medium with homogeneous velocity and statistical properties. Our model has Q and turbidity structures which vary as functions of depth only, and contains an isotropic distribution of scatterers of constant size a, each of which occupies the center of a cube of fixed dimensions larger than the scattering scale a. The earthquake source is set at the center of an individual block from which, for our purpose, we have removed the scatterer. The station occupies the center of a half-block at the free surface of the medium. The model is outlined in Fig. 5.5. We shall use the Born approximation and consider only singly scattered wavelets propagating along straight ray paths from the source to individual scatterers and from these scatterers to the station. Each layer in our model has a thickness equal to the size of one block and is characterized by a fixed value of the intrinsic Q and of the mean square velocity fluctuation $<\mu^2>$. The power spectral density $P(\omega|t)$ of an individual wavelet scattered from the ith scatterer and arriving at the station at time t_i is expressed as

$$P_i(\omega|t_i) \propto \frac{1}{(\ell_{1i}\ell_{2i})^2}\, g_i(\theta_i)\, e^{-\frac{\omega}{v}\sum_j \frac{\Delta\ell_j}{Q_j}} \qquad (5.13)$$

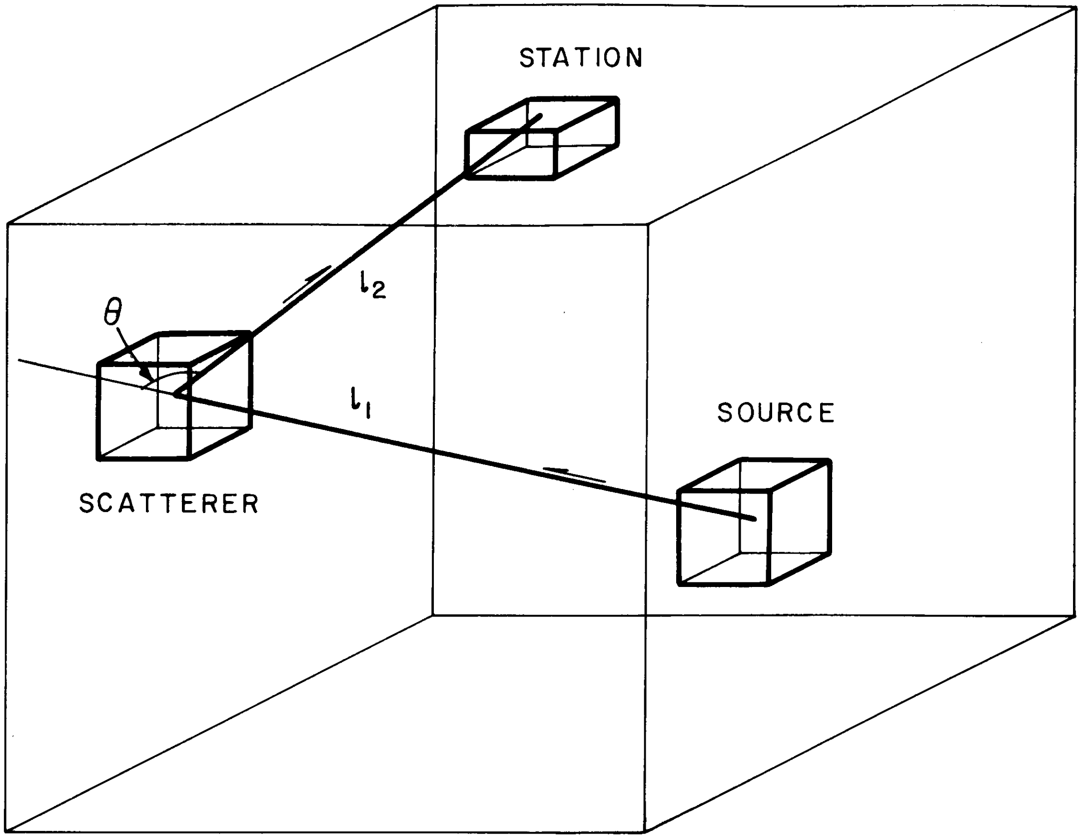

Fig. 5.5. Three-dimensional single scattering block-model used for the study of the temporal variation observed in the 24 Hz coda at Stone Canyon.

where ω is the angular frequency, v is the propagation velocity of the waves, and ℓ_{1i} and ℓ_{2i} are the distances from the source to the scatterer and from the scatterer to the station, respectively. $g_i(\theta_i)$ is the turbidity coefficient associated with the scatterer and θ_i is the angle between the direction from the center of the scattering block to the station and the direction of propagation of the incident wavelet (Fig. 5.5). The term $\sum_j \frac{\Delta\ell_j}{Q_j}$ represents the attenuation due to each layer crossed by the wave along its path. For a source in the mth layer and ith scatterer in the nth layer we have

$$\sum_j \frac{\Delta\ell_j}{Q_j} = \frac{\ell_{1i}}{2(m-n)}\left(\frac{1}{Q_m}+\frac{1}{Q_n}\right) + \frac{\ell_{1i}}{m-n}\sum_{j=n+1}^{m-1}\frac{1}{Q_j} + \frac{\ell_{2i}}{2(n-1)}\left(\frac{1}{Q_n}+\frac{1}{Q_1}\right) + \frac{\ell_{2i}}{n-1}\sum_{j=2}^{n-1}\frac{1}{Q_j} \tag{5.14}$$

where Q_j is the quality factor for the jth layer. We shall describe the turbidity $g(\theta)$ according to Chernov (1960). For an acoustic random medium with a spatial auto-correlation function $N(r) = e^{-r/a}$, $g(\theta)$ is given by equation (2.20)

$$g(\theta) = \frac{8k^4a^3\langle\mu^2\rangle}{(1+4k^2a^2\sin^2\frac{\theta}{2})^2} \tag{2.20}$$

where k is the wave number $2\pi/\lambda$. On the other hand, for $N(r) = e^{-r^2/a^2}$ we have the alternate equation (2.21)

$$g(\theta) = (\pi)^{1/2}k^4a^3\langle\mu^2\rangle\exp(-k^2a^2\sin^2\tfrac{\theta}{2}) \tag{2.21}$$

Because of our earlier assumption that the coda waves under consideration are probably composed mostly of shear waves, we shall use the θ-dependences given in the above two formulas only to gain a rough idea about the sensitivity of the coda to different functions N(r) and to various values of the factor ka.

For a block size sufficiently larger than the scattering scale length a, we can consider the scattering process as a superposition of statistically independent events and add the contributions received from different scatterers during the time interval $(k-1)\Delta t$ and $k\Delta t$ to obtain the power spectral density $P_k(\omega|t_k)$ at time t_k

$$P_k(\omega|t_k) = \sum_{(k-1)\Delta t < t_i \leq k\Delta t} P_i(\omega|t_i) \tag{5.15}$$

from which we derive the RMS coda amplitude $A_k(\omega|t_k)$ as

$$A_k(\omega|t_k) \propto [P_k(\omega|t_k)]^{1/2} \tag{5.16}$$

For simplicity we shall investigate the effects of a variation in the Q structure or turbidity structure separately and limit our models only to the 24 Hz coda, which, we believe is due to back-scattered body waves. Since the temporal change appears as an increase in the energy content of the coda, we shall concentrate on the effects of increasing Q or $<\mu^2>$ in layers of different thicknesses at various depths. Let us consider a medium with velocity of 3.5 km/sec. The backward turbidity found at 24 Hz at Stone Canyon is roughly 0.02 - 0.1 km^{-1} (Tables 12 and 13). According to equation (2.20) these values of $g(\pi)$ are compatible with a root mean square velocity fluctuation $<\mu^2>^{1/2}$ of 5-10% and a scattering scale length of 10-250 m. This allows us to choose the unit block size of our model as 3 km. Taking the two events displayed in Fig. 4.25 as examples we place the earthquake source at a depth of 6 km and epicentral distance of 12 km. The position of this source is not critical, however, as long as it stays within the limits given in Table 1. We also limit the dimensions of the model to 156 x 156 x 81 km and set the station at the center of the 156 x 156 km free surface. These dimensions fix the maximum coda duration, measured from origin time, at 44 sec which is quite adequate because the 24 Hz coda observed at STC does not last beyond 50 sec (Fig. 4.26).

Preliminary models indicate that in order to reproduce observed coda with an apparent Q of the order of 1000-2000 such as shown in Fig. 5.4 an average intrinsic Q of 40 over the first 13.5 km of the crust together with an average value of 2000 between 58.5 and 81 km are reasonable lower and upper bounds. In addition we have a limitation on the size of the scattering scale length set by the amplitude of the coda observed in the records. For example at 24 Hz and with $v = 3.5$ km/sec we have $k = 43.085$. Then if we choose $a = 250$ m we obtain $k^2a^2 = 116$ which, because of the particular form of equation (2.21) does not produce a coda of significant amplitude. In view of this constraint let us fix the scattering scale length at 100 m and compare the synthetic coda obtained with ka = 4.3 using the two spatial auto-correlation functions $N(r) = e^{-r/a}$ and $N(r) = e^{-r^2/a^2}$ with the results derived in the case of isotropic scattering ($ka << 1$). Three models are shown in Fig. 5.6. The initial Q structures depicted share in common a low intrinsic Q of 100 in the shallow crust, an intermediate Q of 500 in the deep crust and a high Q of 1500-1800 extending below the crust down to 81 km, the maximum depth extent for our block-model in the present configuration. In model 1 (Fig. 5.6a) the intrinsic Q is increased from 500 to 1800 in the depth range of 22.5 to 37.5 km and in model 2 (Fig. 5.6b) Q is increased from 100 to 500 between 4.5 and 10.5 km. The mean square velocity fluctuation $<\mu^2>$ is maintained constant in both models. Finally, in model 3 (Fig. 5.6c), the Q structure remains unchanged but $<\mu^2>$ is increased with depth z according to the function $1 + 3.5 \exp -(\frac{z-6}{35})^2$ from an initial constant value of 1. The normalized synthetic coda amplitudes computed before and after the change in the Q or $<\mu^2>$ structures are shown for the individual models in Figures 5.7 through 5.9. Figures 5.7a, 5.8a and 5.9a were obtained with a spatial auto-correlation function $N(r) = e^{-r/a}$ and Figures 5.7b, 5.8b and 5.9b correspond to the case of $N(r) = e^{-r^2/a^2}$. Figures 5.7c through 5.9c represent the case of isotropic scattering. To compare the apparent Q of coda for

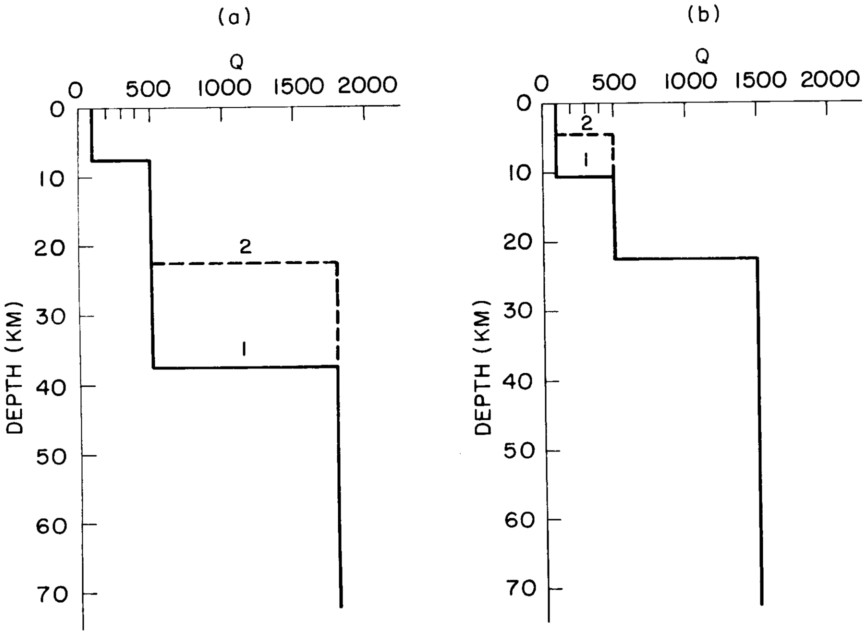

MODEL 1

MODEL 2

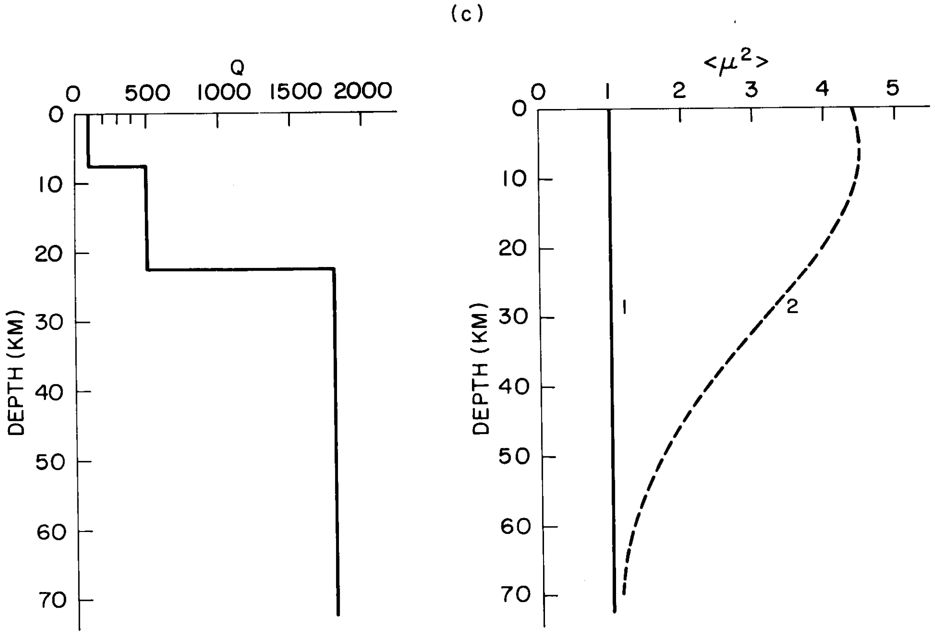

MODEL3

Fig. 5.6. Structures used to model the temporal variation observed in the 24 Hz coda at Stone Canyon. In models 1 and 2 the intrinsic Q is increased in a layer while $<\mu^2>$ remains fixed. In model 3, the Q structure is fixed while $<\mu^2>$ is increased. The dashed lines depict the new structures after the change in Q or normalized $<\mu^2>$.

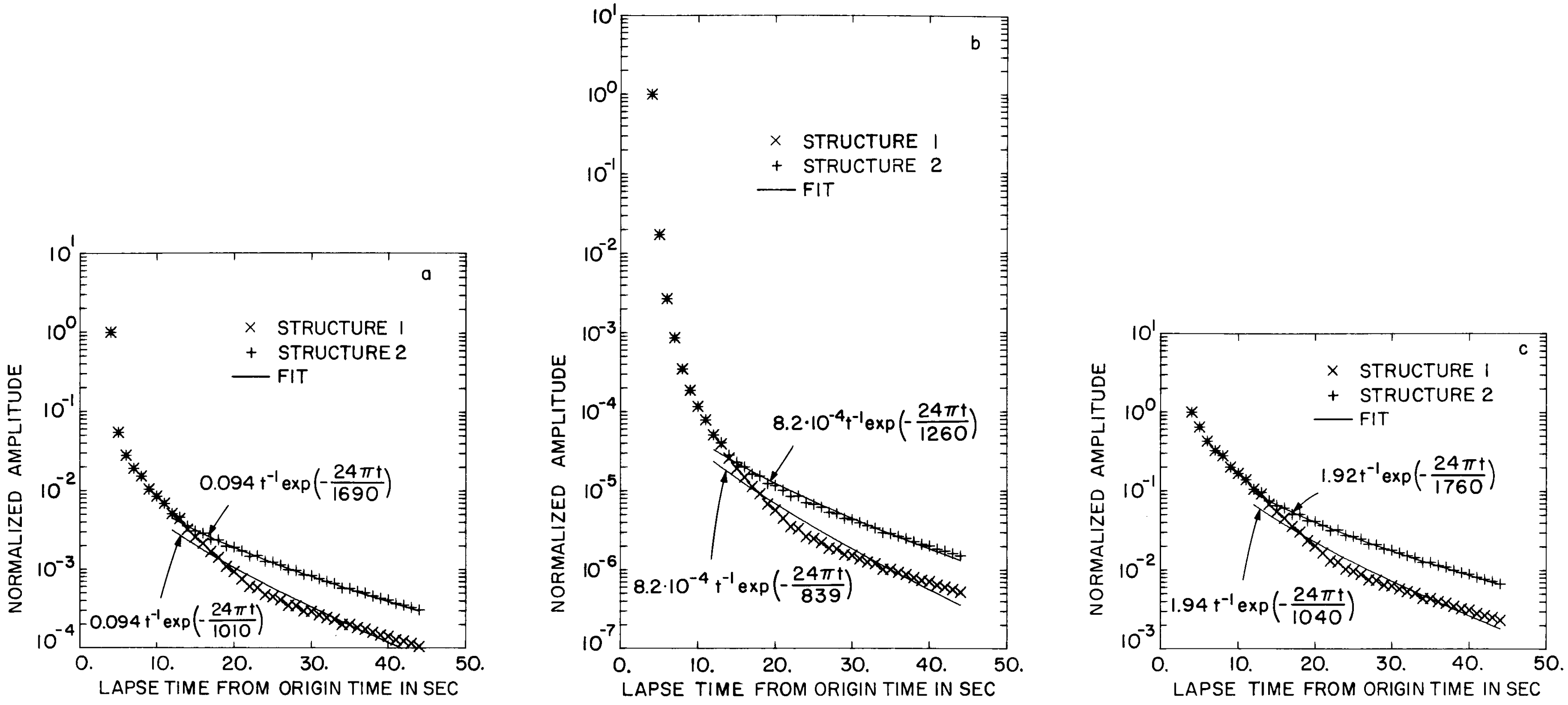

Fig. 5.7. Normalized synthetic coda amplitudes computed for an earthquake at an epicentral distance of 12 km and depth of 6 km using model 1 (Fig. 5.6a). Plots a and b were obtained with ka = 4.3 and using $N(r) = e^{-r/a}$ and $N(r) = e^{-r^2/a^2}$, respectively. Plot c depicts the results for isotropic scattering (ka<<1). Structure 1 refers to the original Q structure and structure 2 to the new structure after the increase in the intrinsic Q. The plain curves are fits obtained with the function $ct^{-1}\exp(-24\pi t/Q)$.

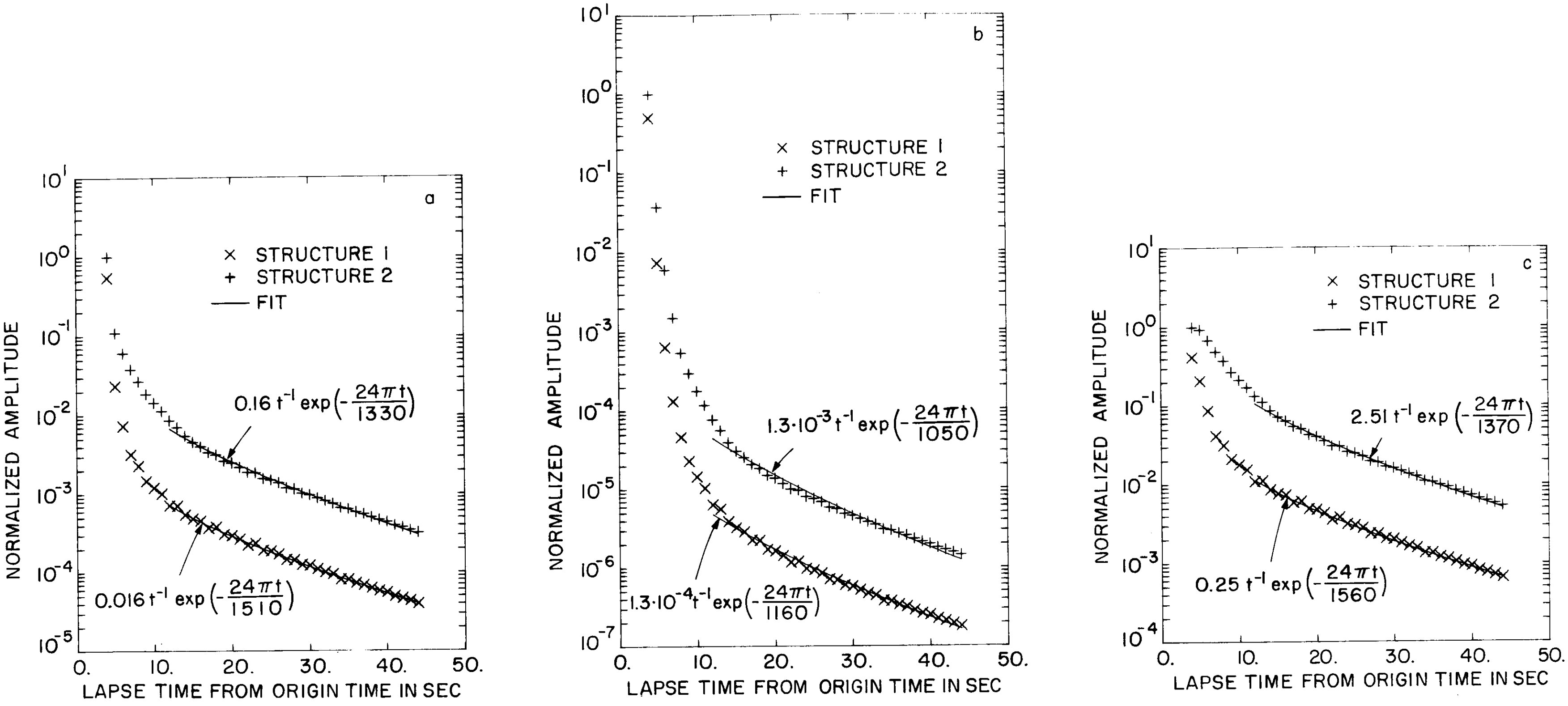

Fig. 5.8. Normalized synthetic coda amplitudes computed for an earthquake at an epicentral distance of 12 km and depth of 6 km using model 2 (Fig. 5.6b). Plots a and b were obtained with ka = 4.3 and using $N(r) = e^{-r/a}$ and $N(r) = e^{-r^2/a^2}$, respectively. Plot c depicts the results for isotropic scattering (ka<<1). Structure 1 refers to the original Q structure and structure 2 to the new structure after the increase in the intrinsic Q. The plain curves are fits obtained with the function $ct^{-1}\exp(-24\pi t/Q)$.

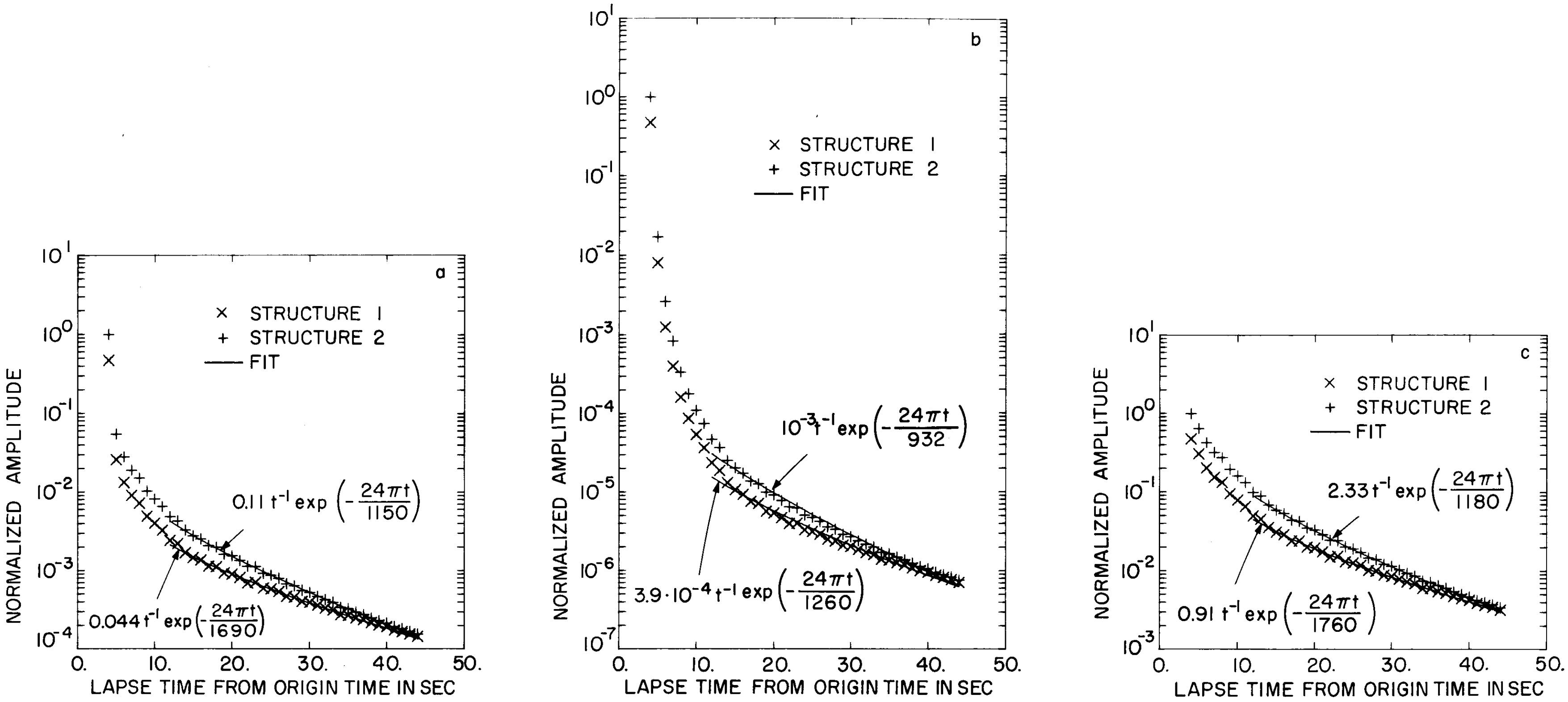

Fig. 5.9. Normalized synthetic coda amplitudes computed for an earthquake at an epicentral distance of 12 km and depth of 6 km using model 3 (Fig. 5.6c). Plots a and b were obtained with ka = 4.3 and using $N(r) = e^{-r/a}$ and $N(r) = e^{-r^2/a^2}$, respectively. Plot c depicts the results for isotropic scattering (ka<<1). Structure 1 refers to the original $<\mu^2>$ structure and structure 2 to the new structure after the increase in $<\mu^2>$. The plain curves are fits obtained with the function $ct^{-1}\exp(-24\pi t/Q)$.

these models with those obtained at Stone Canyon, the synthetic amplitudes were fitted over the time range of 12 to 44 sec with the function $ct^{-1}\exp(-24\pi t/Q)$ describing the single scattering model for body waves. The fitted functions are shown as plain curves in the figures.

The results obtained with $N(r) = e^{-r/a}$ and ka = 4.3 are very similar to those derived in the case of isotropic scattering. A spatial auto-correlation function of the type $N(r) = e^{-r^2/a^2}$, however, seems less appropriate because it leads to an amplitude decay that is generally too strong to fit with the observation. Of the three models proposed here only the last two show the trend observed in the apparent Q of coda (Fig. 5.4), that is a decrease in the value of this factor following the change in the crustal structure. Model 1 (Fig. 5.7) shows just the reverse result. In Fig. 5.7c for example the apparent Q increases from 1040 to 1760. This trend is related to the depth at which the Q structure has changed. As indicated in Fig. 5.7 the computed coda amplitudes remain unaffected up to t = 13 sec, the arrival time of the waves backscattering from the top of the 15 km thick layer in which the intrinsic Q has increased. The effect of this increase, which starts to be felt beyond 13 sec, is to amplify the later arrivals, resulting in a longer signal duration and, consequently, a larger value of the apparent Q. It appears unlikely then that a change in the intrinsic Q at the bottom of the crust can affect the intermediate coda without altering the duration of seismogram. Model 2 (Fig. 5.8), on the other hand, presents interesting features. The five-fold increase of the intrinsic Q at shallow depth amplifies the coda amplitudes by a maximum factor of 13 at t = 9 sec. The amplitudes of the first arrivals at t = 4 sec are larger by a factor of 2 and the amplitudes at t = 44 sec are multiplied by 8. While about four times too large this amplification of the coda is in general agreement with the observation. The large residual amplification at 44 sec is due to the fact that the Q increase occurs in a layer that contains the earthquake focus and affects indiscriminately all the wave paths originating from the source. This accounts for the rather weak decrease of 100-200 in the apparent Q of the synthetic coda resulting from the structural change. The amplification of the coda amplitudes depicted in Fig. 5.8 can be reduced by choosing a smaller increase in the intrinsic Q shown in Fig. 5.6b and the discrepancy in the signal duration before and after the change in the structure may possibly be reduced by associating this increase with a low velocity layer. Shallow nearly horizontal ray paths emanating from the earthquake source would sample more of this layer and thus be comparatively more affected than nearly vertical rays backscattering from deep heterogeneities with short paths through the layer. A multiple scattering process in which waves remain trapped in this layer may also produce the desired effect. Such elaborate models, however, are beyond the scope of the present study. The presence of a low velocity zone in the upper crust, having a lower boundary at depths between approximately 8 and 15 km, has been suggested by several seismologists and has been associated in various tectonic areas with intrusive bodies having lower velocities and densities than the surrounding country rocks (e.g. Landisman et al., 1971). Model 2 suggests that the structural change responsible for the change in behavior of the high frequency coda does not exceed a depth of about 10 km. At shallow depths, down to a few kilometers, an increase of the intrinsic Q may be related to the closure of microcracks due to an increase of stress in the area. This stress accumulation appears consistent with the increase in stress drop suggested in Chapter 4 for local earthquakes in the magnitude range from 1.5 to 3. More extended discussions on this problem seem premature at this point.

An alternate model that can match the observation made at Stone Canyon is model 3. As indicated in Figs. 5.9a and 5.9c the values of the apparent Q of the synthetic coda computed before and after the change in the $<\mu^2>$ structure (Fig. 5.6c) have the correct magnitudes, decreasing from 1700-1800 down to 1100-1200. The physical process underlying the large increase of $<\mu^2>$ required for this result is more difficult to visualize, however. The mean square velocity fluctuation may become significantly larger when cracks open up, but such a process, if it exists, is more likely to occur at shallow depth than at the confining pressures of several kbars existing at the depths suggested by model 3. Thus a change in the intrinsic Q associated with a low velocity layer at a depth roughly coinciding with the depth of earthquake activity on the San Andreas seems more appropriate to explain the change observed in the 24 Hz coda at Stone Canyon.

5.5 Concluding remarks

We suggested earlier that the high frequency coda waves above 10 Hz are made of backscattering body waves. The value of backward turbidity required to explain them as backscattering body waves is about 10^{-1}-10^{-2} km^{-1} for all the stations. If we use equation (2.20) as an approximate description of the turbidity for coda waves, one can get a rough estimate of the ratio $\langle\mu^2\rangle/a$. The required backward turbidity may then be explained by assuming the correlation distance a = 10-500 m and $\langle\mu^2\rangle^{1/2}$ = 5-10%. Although this result is not uniquely determined, such a small scale inhomogeneity, if it exists under Lasa, may give negligible effects on teleseismic body waves with frequency around 1 Hz or be masked by the effects of larger-scale inhomogeneity. Thus there is no observation against the idea that the high frequency coda waves are backscattering body waves from heterogeneities in the deep lithosphere.

The frequency dependence observed in the apparent Q of coda waves is useful for the study of the medium structure in various areas. In Hawaii, for example, the apparent Q is high at low frequency and low at high frequency compared to other regions in California or Japan. The roughly constant apparent Q of 250 below 6 Hz and short duration of the coda at 24 Hz observed near Kilauea, as well as the value of the intrinsic Q required to correct the seismograms of small earthquakes in the area suggest the existence of a thick layer with an intrinsic Q of about 250 extending over most of the crust under this volcanic region. By contrast the increase of Q with depth is more pronounced near Stone Canyon as suggested by the models shown in Fig. 5.6.

The sensitivity of the high frequency coda to details of the crustal structure also appears to be promising for the study of temporal changes in the medium properties. By extending our single scattering model to include the vertical heterogeneity in Q we found that the peculiar behavior of the 24 Hz coda at Stone Canyon may be related to an increase of tectonic stress in the area.

CHAPTER 6

Conclusions

A method has been proposed to determine the source spectra of small earthquakes from their coda waves. The basic assumption underlying our technique is that the coda spectra are independent of epicentral distance and details of the direct wave path from source to station. The existence of a common shape of coda amplitude decay curve (Figures 3.10, 3.11 and 3.12) supports that assumption.

Two extreme models of the wave medium were proposed to account for the observation made on the coda waves. Both models are based on the idea that the coda waves are backscattering waves from numerous heterogeneities distributed uniformly in the earth's crust. In the first model, the scattering was assumed to be a weak process, and use was made of the Born approximation. Because of this approximation the law of conservation of energy was violated. To alleviate this problem, a second model was considered in which the seismic energy transfer was considered as a diffusion process. In this strong scattering model, the energy was of course conserved, but the exact partitioning of seismic energy between the forward and backward scattering modes remained undefined. The inadequacy of these two models in dealing with the energy balance is a reflection of their extreme simplicity. Despite these difficulties, however, we feel they offer a basis from which a quantitative description of the origin of coda waves can be made. If the value of turbidity previously derived by Aki (1973) for the lithosphere under the Montana Lasa also applies to the lithosphere under California, Hawaii, and Japan, the coda waves at around 1.5 Hz cannot be explained as backscattering body waves from heterogeneities in the lithosphere. We concluded that the coda waves at this frequency are primarily backscattering surface waves. The low Q found for these waves supports this assumption. On the other hand the high Q found for waves at frequencies higher than 10 Hz strongly suggests that at these frequencies the coda is made of backscattering body waves from the deep high-Q lithosphere.

The turbidities required to explain the coda waves at frequencies higher than 10 Hz as backscattering body waves are of the order of 10^{-1}-10^{-2} km^{-1}, which may correspond to scatterer sizes in the range 10-500 m for a fractional RMS velocity fluctuation of a few percent.

APPENDIX

The matrix formulation of the least square problem described in Chapter 3 is given by equation (A.3) when the parameter a in (3.8) is set free, or by equation (A.4) if this parameter is fixed. In these two equations, the weighting factor w_{ij} has the value 1 when the corresponding amplitude A_{ij} exists, otherwise w_{ij} has the value 0. Note also that the signs of the parameters a and b have been changed in both equations for convenience.

Close scrutiny of (A.3) and (A.4) suggests that the matrices of the normal equations are not well balanced. The presence of the term $\sum_i t_i$ and $\sum_i t_i^2$ in row and column 2 of the matrix in (A.3) and in row and column 1 of the matrix in (A.4) will lead to very large values that might affect the precision of the computed inverses. This in turn will affect the resolution of the vector of parameters p. To prevent these computational artifacts a scaling factor α has been applied to the biased rows and columns in equations (A.3) and (A.4). Following computation of the vector p, the factor b (equation 3.8) is obtained by remultiplying by α the corresponding parameter in p. To compute the least square error estimate for b from equation (3.15) we then write

$$(\delta p_2)^2_{RMS} \simeq \alpha^2 (\tilde{U}U)^{-1}_{22} \frac{\sum_i [\bar{R}(t_i)]^2}{\ell - (m+2)} \qquad (A.1)$$

And similarly computing the least square error estimate for b using equation (3.16):

$$(\delta p_1)^2_{RMS} \simeq \alpha^2 (\tilde{UU})^{-1}_{11} \frac{\sum_i [\bar{R}(t_i)]^2}{\ell - (m+1)} \qquad (A.2)$$

The value of the scaling factor α was obtained by minimizing the deviations of the matrix product $(\tilde{UU})^{-1}(\tilde{UU})$ from the identity matrix. In most of the least square fits that we processed this value was set to 0.005.

$$p = \begin{bmatrix} n_a \\ n_b \\ n_{C_1} \\ n_{C_2} \\ \vdots \\ n_{C_m} \end{bmatrix} = \begin{bmatrix} \sum_j\sum_i (w_{ij})^2(\log_{10}t_i)^2 & \alpha\sum_j\sum_i (w_{ij})^2 t_i\log_{10}t_i & \sum_i (w_{i1})^2\log_{10}t_i & \sum_i (w_{i2})^2\log_{10}t_i & \cdots\cdots & \sum_i (w_{im})^2\log_{10}t_i \\ \alpha\sum_j\sum_i (w_{ij})^2 t_i\log_{10}t_i & \alpha^2\sum_j\sum_i (w_{ij})^2 t_i{}^2 & \alpha\sum_i (w_{i1})^2 t_i & \alpha\sum_i (w_{i2})^2 t_i & \cdots\cdots & \alpha\sum_i (w_{im})^2 t_i \\ \sum_i (w_{i1})^2\log_{10}t_i & \alpha\sum_i (w_{i1})^2 t_i & \sum_i (w_{i1})^2 & 0 & \cdots\cdots & 0 \\ \sum_i (w_{i2})^2\log_{10}t_i & \alpha\sum_i (w_{i2})^2 t_i & 0 & \sum_i (w_{i2})^2 & \cdots\cdots & 0 \\ \vdots & \vdots & \vdots & \vdots & & \vdots \\ \sum_i (w_{im})^2\log_{10}t_i & \alpha\sum_i (w_{im})^2 t_i & 0 & 0 & \cdots\cdots & \sum_i (w_{im})^2 \end{bmatrix}^{-1} \times \begin{bmatrix} \sum_j\sum_i (w_{ij})^2\log_{10}t_i\log_{10}A_{ij} \\ \alpha\sum_j\sum_i (w_{ij})^2 t_i\log_{10}A_{ij} \\ \sum_i (w_{i1})^2\log_{10}A_{i1} \\ \sum_i (w_{i2})^2\log_{10}A_{i2} \\ \vdots \\ \sum_i (w_{im})^2\log_{10}A_{im} \end{bmatrix} \qquad \text{(A.3)}$$

$$p = \begin{bmatrix} n_b \\ n_{C_1} \\ n_{C_2} \\ \vdots \\ n_{C_m} \end{bmatrix} = \begin{bmatrix} \alpha^2\sum_j\sum_i (w_{ij})^2 t_i^2 & \alpha\sum_i (w_{i1})^2 t_i & \alpha\sum_i (w_{i2})^2 t_i & \cdots\cdots & \alpha\sum_i (w_{im})^2 t_i \\ \alpha\sum_i (w_{i1})^2 t_i & \sum_i (w_{i1})^2 & 0 & \cdots\cdots & 0 \\ \alpha\sum_i (w_{i2})^2 t_i & 0 & \sum_i (w_{i2})^2 & \cdots\cdots & 0 \\ \vdots & \vdots & \vdots & & \vdots \\ \alpha\sum_i (w_{im})^2 t_i & 0 & 0 & \cdots\cdots & \sum_i (w_{im})^2 \end{bmatrix}^{-1} \times \begin{bmatrix} \alpha\sum_j\sum_i (w_{ij})^2(\log_{10}A_{ij} - a\log_{10}t_i)t_i \\ \sum_i (w_{i1})^2(\log_{10}A_{i1} - a\log_{10}t_i) \\ \sum_i (w_{i2})^2(\log_{10}A_{i2} - a\log_{10}t_i) \\ \vdots \\ \sum_i (w_{im})^2(\log_{10}A_{im} - a\log_{10}t_i) \end{bmatrix} \qquad \text{(A.4)}$$

REFERENCES

Aki, K., Correlogram analyses of seismograms by means of a simple automatic computer, J. Phys. Earth, 4, 71-79, 1956.

Aki, K., Generation and propagation of G waves from the Niigata earthquake of June 16, 1964, Bull. Earthquake Res. Inst. Tokyo Univ., 44, 23-88, 1966.

Aki, K., Scaling law of seismic spectrum, J. Geophys. Res., 72, 1217-1231, 1967.

Aki, K., Seismic displacement near a fault, J. Geophys. Res., 73, 5359-5376, 1968.

Aki, K., Analysis of the seismic coda of local earthquakes as scattered waves, J. Geophys. Res., 74, 615-631, 1969.

Aki, K., Earthquake mechanism, Tectonophysics, 13, 423-446, 1972a.

Aki, K., Scaling law of earthquake source time-function, Geophys. J.R. astr. Soc., 31, 3-25, 1972b.

Aki, K., Scattering of P waves under the Montana Lasa, J. Geophys. Res., 78, 1334-1346, 1973.

Aki, K., and B. Chouet, Origin of coda waves: source, attenuation, and scattering effects, J. Geophys. Res., 80, 3322-3342, 1975.

Aki, K., and W.H. Lee, Determination of three-dimensional velocity anomalies under a seismic array using first P arrival times from local earthquakes, 1. A homogeneous initial model, preprint, 1975.

Aki, K., and M. Tsujiura, Correlation study of near earthquake waves, Bull. Earthquake Res. Inst. Tokyo Univ., 37, 207-232, 1959.

Aki, K., M. Tsujiura, M. Hori, and K. Goto, Spectral study of near earthquake waves, Bull. Earthquake Res. Inst. Tokyo Univ., 36, 71-98, 1958.

Bakun, W.H., and C.G. Bufe, Shear-wave attenuation along the San Andreas fault zone in central California, Bull. Seismol. Soc. Amer., 65, 439-459, 1975.

Bakun, W.H., C.G. Bufe, and R.M. Stewart, Body-wave spectra of central California earthquakes, Bull. Seismol. Soc. Am., 66, 363-384, 1976.

Ben-Menahem, A., Radiation of seismic surface-waves from finite moving sources, Bull. Seismol. Soc. Amer., 51, 401-435, 1961.

Berkhemer, H., Die Ausdehnung der Bruchfläche im Erdbebenherd und ihr Einfluss auf das seismische Wellenspektrum, Gerland's Beitr. Geophys., 71, 5-26, 1962.

Bisztricsany, E.A., A new method for the determination of the magnitude of earthquakes, Geofiz. Kozlem., 7, 2, 1958.

Boore, D.M., and D.P. Hill, Wave propagation characteristics in the vicinity of the San Andreas fault, in Proceedings of the Conference on Tectonic Problems of the San Andreas Fault System, edited by R.L. Kovach and A. Nur, Geological Sciences, Vol. XIII, School of Earth Sciences, Stanford University, 1973.

Brune, J.N., Tectonic stress and the spectra of seismic shear waves from earthquakes, J. Geophys. Res., 75, 4997-5009, 1970.

Brune, J.N., Correction, J. Geophys. Res., 76, 5002, 1971.

Capon, J., High-resolution frequency-wave number spectrum analysis, Proc. IEEE, 57, 1408-1418, 1969.

Capon, J., Characterization of crust and upper mantle structure under Lasa as a random medium, Bull. Seismol. Soc. Amer., 64, 235-266, 1974.

Chernov, L.A., Wave Propagation in a Random Medium, pp. 35-57, McGraw-Hill, New York, 1960.

Cleary, J.R. and R.A.W. Haddon, Seismic wave scattering near the core-mantle boundary: A new interpretation of precursors to PKIKP, Nature, 240, 549-550, 1972.

Clowes, R.M., and E.R. Kanasewich, Seismic attenuation and the nature of reflecting horizons within the crust, J. Geophys. Res., 75, 6693-6705, 1970.

Dainty, A., M.N. Toksöz, K.R. Anderson, P.J. Pines, Y.Y. Nakamura, and G. Latham, Seismic scattering and shallow structure of the moon in Oceanus Procellarum, Moon, 9, 11-29, 1974a.

Dainty, A.M., P.J. Pines, and M.N. Toksöz, Strong scattering of seismic waves: Examples from model experiments and the moon (abstract), EOS Trans. AGU, 55, 362, 1974b.

Douglas, B.M., and A. Ryall, Spectral characteristics and stress drop for microearthquakes near Fairview Peak, Nevada, J. Geophys. Res., 77, 351-359, 1972.

Dunkin, J.W., Scattering of transient, spherical P waves by a randomly inhomogeneous elastic half-space, Geophysics, 34, 357-382, 1969.

Eaton, J.P., Crustal structure and volcanism in Hawaii, in MacDonald, G.A., and Kuno, Hisachi, eds., Crust of the Pacific basin: Am. Geophys. Union, Geophys. Mon., 6, 13-29, 1962.

Eshelby, J.D., The determination of the elastic field of an ellipsoidal inclusion and related problems, Proc. R. Soc. Lond., Ser. A, 241, 376-396, 1957.

Greenfield, R.J., Short-period P wave generation by Rayleigh wave scattering at Novaya Zemlya, J. Geophys. Res., 76, 7988-8002, 1971.

Gutenberg, B., and C.F. Richter, Earthquake magnitude, intensity, energy and acceleration, Bull. Seismol. Soc. Am., 46, 105-145, 1956.

Haddon, R.A.W., Corrugations on the mantle-core boundary or transition layers between inner and outer cores? (abstract), EOS Trans. AGU, 53, 600, 1972.

Haddon, R.A.W., Scattering of seismic body waves by small random inhomogeneities in the earth, preprint, 1975.

Hanks, T.C., The faulting mechanism of the San Fernando earthquake, J. Geophys. Res., 79, 1215-1229, 1974.

Hanks, T.C., Observations and estimation of long-period strong ground motion in the Los Angeles basin, preprint, 1975.

Hanks, T.C. and M. Wyss, The use of body-wave spectra in the determination of seismic source parameters, Bull. Seismol. Soc. Am., 62, 561-589, 1972.

Haskell, N., Total energy and energy spectral density of elastic wave radiation from propagating faults, Bull. Seismol. Soc. Am., 54, 1811-1842, 1964.

Hill, D.P., Crustal structure of the island of Hawaii from seismic-refraction measurements, Bull. Seismol. Soc. Am., 59, 101-130, 1969.

Howe, M.S., Wave propagation in random media, J. Fluid Mech. 45 (4), 769-783, 1971.

Howe, M.S., Conservation of energy in random media, with application to the theory of sound absorption by an inhomogeneous flexible plate, Proc. Roy. Soc., Ser. A 331, 479-496, 1973a.

Howe, M.S., On the kinetic theory of wave propagation in random media, Phil. Trans. Roy. Soc. London, Ser. A., 274, 523-549, 1973b.

Husebye, E.S., D.W. King, and R.A.W. Haddon, Precursors to PKIKP and seismic wave scattering near the core-mantle boundary, J. Geophys. Res., 81, 1870-1882, 1976.

Ishida, M., Determination of fault parameters of small earthquakes in the Kii peninsula, preprint, 1974.

Johnson, L.R., and T.V. McEvilly, Near-field observations and source parameters of central California earthquakes, Bull. Seismol. Soc. Am., 64, 1855-1886, 1974.

Keilis-Borok, V.I., On estimation of the displacement in an earthquake source and of source dimensions, Ann. Geofis., 12, 205-214, 1959.

King, D.W., R.A.W. Haddon, and J.R. Cleary, Evidence for seismic wave scattering in the D"layer, Earth Planet. Sci. Lett., 20, 353-356, 1973.

Kopnichev, Y.F., Models for the formation of the coda part of seismograms, Acad. Nauk USSR, 222, 333-335, 1975 (in Russian).

Kurita, T., Attenuation of shear waves along the San Andreas fault zone in central California, Bull. Seismol. Soc. Am., 65, 277-292, 1975.

Landisman, M., S. Mueller, and B.J. Mitchell, Review of evidence for velocity inversions in the continental crust, in Heacock, J.G., ed., The Structure and Physical Properties of the Earth's Crust, Am. Geophys. Union, Geophys. Mon., 14, 11-34, 1971.

Lee, W.H.K., R.E. Bennett, and K.L. Meagher, A method of estimating magnitude of local earthquakes from signal duration, open file report, 28 pp., Nat. Center for Earthquake Res., U.S. Geol. Surv., Menlo Park, Calif., 1972.

Levin, F.K., and D.J. Robinson, Scattering by a random field of surface scatterers, Geophysics, 34, 170-179, 1969.

Madariaga, R., The dynamics of an expanding circular fault, Bull. Seismol. Soc. Am., 66, 639-666, 1976.

Maruyama, T., On the force equivalents of dynamic elastic dislocations with reference to the earthquake mechanism, Bull. Earthquake Res. Inst. Tokyo Univ., 41, 467-486, 1963.

Molnar, P., K.H. Jacob, and K. McCamy, Implications of Archambeau's earthquake source theory for slip on faults, Bull. Seismol. Soc. Am., 63, 101-104, 1973.

Nakamura, Y., Seismic energy transmission in the lunar surface zone determined from signals generated by movements of lunar rovers, Bull. Seismol. Soc. Am., 593-606, 1976.

Nakamura, Y., G.V. Latham, M. Ewing, and J. Dorman, Lunar seismic energy transmissions (abstract), EOS Trans. AGU, 51, 776, 1970.

Nikolayev, A.V., Seismic properties of weakly heterogeneous media, Izv. Acad. Sci. USSR Phys. Solid Earth, 2, 83-87, 1968.

Nikolayev, A.V., The seismics of heterogeneous and turbid media, 140 p., translated from Russian, Keterpress enterprises, Jerusalem, 1975.

Nikolayev, A.V. and F.S. Tregub, A statistical model of the earth's crust: Method and results, Tectonophysics, 10, 573-578, 1970.

O'Neill, M.E., and J.H. Healy, Determination of source parameters of small earthquakes from P-wave rise time, Bull. Seismol. Soc. Amer., 63, 599-614, 1973.

Randall, M.J., Spectral peaks and earthquake source dimension, J. Geophys. Res., 78, 2609-2611, 1973.

Rautian, T.G., and V.I. Khalturin, The frequency-temporal properties of coda waves for local earthquakes of Garm region, USSR, preprint, 1976.

Ryall, A., and D.L. Bennett, Crustal structure of southern Hawaii related to volcanic processes in the upper mantle, J. Geophys. Res., 73, 4561-4582, 1968.

Scheimer, J., and T.E. Landers, Short-period coda of a local event at Lasa, Seismic Discrimination, Semiannu. Tech. Sum. 42, Lincoln Lab., Mass Inst. of Technol., Cambridge, 1974.

Soloviev, S.L., Seismicity of Sakhalin, Bull. Earthquake Res. Inst. Tokyo Univ., 43, 95-102, 1965.

Street, R.L., R.B. Herrmann, and O.W. Nuttli, Spectral characteristics of the Lg wave generated by central United States earthquakes, Geophys. J. R. Astr. Soc., 41, 51-63, 1975.

Stump, B.E., P and S wave corner frequencies observed in the near field and the effect of attenuation, EOS Trans. AGU, 56, 1148, 1974.

Takano, K., Analysis of seismic coda waves of ultramicro-earthquakes in the Matsushiro area - a comparison with Parkfield, California, J. Phys. Earth, 19, 209-216, 1971.

Thatcher, W., Regional variations of seismic source parameters in the northern Baja California area, J. Geophys. Res., 77, 1549-1565, 1972.

Thatcher, W., and T.C. Hanks, Source parameter of southern California earthquakes, J. Geophys. Res., 78, 8547-8576, 1973.

Tocher, D., Earthquake energy and ground breakage, Bull. Seismol. Soc. Am., 48, 147-152, 1958.

Tocher, D., Movements on faults, Proc. 2nd World Conf. Earthquake Engineering, 1, 551-564, 1960.

Tsai, Y.B., and K. Aki, Simultaneous determination of the seismic moment and attenuation of seismic surface waves, Bull. Seismol. Soc. Amer., 59, 275-287, 1969.

Tsujiura, M., Frequency analysis of seismic waves, 1, Bull. Earthquake Res. Inst. Tokyo Univ., 44, 873-891, 1966.

Tsujiura, M., Frequency analysis of seismic waves, 2, Bull. Earthquake Res. Inst. Tokyo Univ., 45, 973-995, 1967.

Tsujiura, M., Regional variation of P wave spectra, 1, Bull. Earthquake Res. Inst. Tokyo Univ., 47, 613-633, 1969.

Tsumura, K., Determination of earthquake magnitude from total duration of oscillation, Bull. Earthquake Res. Inst. Tokyo Univ., 45, 7-18, 1967.

Tucker, B.E., and J.N. Brune, S-wave spectra and source parameters for aftershocks of the San Fernando earthquake of February 9, 1971, in Geological and Geophysical Studies, vol. 3, San Fernando Earthquake of February 9, 1971, National Oceanic and Atmospheric Administration, Washington, D.C., 1973.

Wesley, J.P., Diffusion of seismic energy in the near range, J. Geophys. Res., 70, 5099-5106, 1965.

Wu, F.T., Lower limit of the total energy of earthquakes and partitioning of energy among seismic waves, Ph.D. Thesis, California Institute of Technology, 1966.

Wyss, M., and J.N. Brune, Seismic moment, stress and source dimensions for earthquakes in the California-Nevada region, J. Geophys. Res., 73, 4681-4694, 1968.